ACCELERATOR AND INSTRUMENTATION RESEARCH AND DEVELOPMENT AND CONSTRUCTION

Status of the MSU 4π Array

G. Westfall, C. Ogilvie, D. Cebra, K. Wilson, A. Vander Molen, J. Kam, S. Howden, J. Winfield, J. Yurkon, M. Maier, S. Bricker, and L. Morris

The MSU 4π array is designed to detect all charged particles emitted from intermediate-energy nucleus-nucleus collisions. Using low-pressure multiwire counters (MWPC's), Bragg curve counters (BCC's) and fast/slow plastic scintillator telescopes (FS's), particles ranging from protons to fission fragments can be detected with nearly 4π solid angle.[1]

FIG. 1: Photograph of the MSU 4π array being placed in the interim 4π vault.

The geometry of the device is a truncated icosahedron consisting of 12 pentagonal faces and 20 hexagonal faces. One of the pentagonal faces is used for exit of the beam and another is instrumented with a forward array. Each remaining face will be instrumented with one subarray, consisting of five or six FS's, one BCC, and one MWPC for each pentagonal or hexagonal face. This geometry provides at total of 170 light-particle detectors, 30 target-like-fragment detectors, and 30 fission-fragment detectors. In addition, a 45-element forward array has been installed in the forward pentagonal region. This array consists of FS's, with 1.6-mm ΔE and 18-cm E counters. This array brings the total number of counters to 215. Figure 1 shows a photograph of the MSU 4π Array as it was being installed in the interim vault.

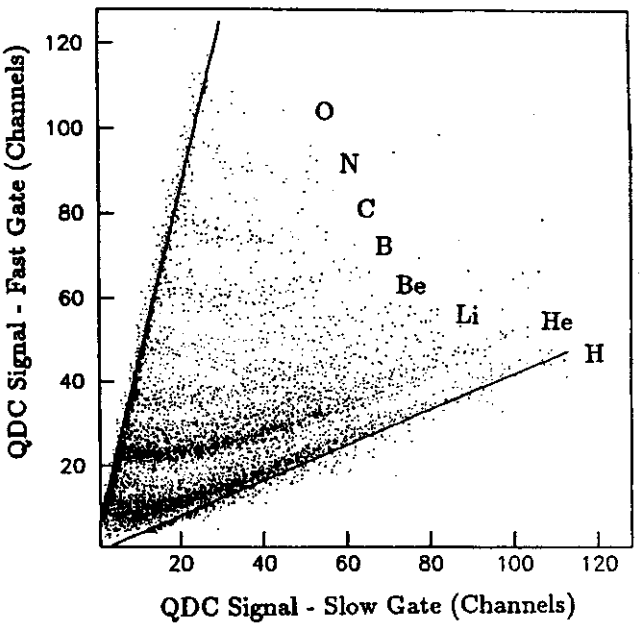

FIG. 2: Typical ΔE-E spectrum for a phoswich from the main ball of the MSU 4π array.

All of the scintillator modules of the array are complete and operational and have been used in a number of experiments on the K500 and the K1200 cyclotrons. A typical ΔE-E spectrum for one of the forward array scintillators is shown in Fig. 2. Two of the 30 BCC's planned have been completed and installed in the array. One of these production BCC's was tested and calibrated using the K500 Cyclotron and the S320 spectrometer. In that test, clear separation between neighboring Z's was demonstrated up to $Z=14$. Most of the parts for the construction of the BCC's are in-house and construction of these counters should be complete by fall of 1989. Completion of the BCC's will be followed by the assembly and installation of the MWPC's, which must be mounted to the front window support of the BCC's.

The scintillator modules are read out using Fast Encoding and Read-out ADC's (FERA's). The ΔE, E, and time signals are obtained using a specially designed splitter system that allows the signal to be carried on the same cable

as the high voltage. The splitter system also matches the impedances of the various input devices and adjusts the gain properly between the three signals. Several new electronic modules have been designed, constructed and installed. These modules include the Fast Decision Module (FDM) and the FERA Faucet Maier (FFM). The FDM is a very fast 16x16-bit programmable memory that allows 65536 different trigger configurations. This device is programmed to respond to 16 different digital inputs and provide 16 digital outputs and a trigger signal with a programmable gate and delay. The FFM is a device to enhance use of the ECLine front panel readout of the FERA modules on the 4π acquisition system. This readout system now can accept up to 25,000 events per second.

Currently, the array resides in the 4π Interim Vault, just downstream of the 92" scattering chamber. Four experiments were carried out with the K500 Cyclotron. One experiment has been completed using the array with the K1200 and one is underway. One more experiment is planned before the entire system is moved to the N2 vault, which will be its permanent location in Phase II of NSCL.

References

1. G.D. Westfall *et al.*, Nucl. Instrum. Methods, A238, 347 (1985).

Bragg-Curve Spectroscopy in a 4π Geometry

D.A. Cebra, S. Howden, J. Karn, D. Kataria, M. Maier, A. Nadasen, E. Norbeck,[a] C.A. Ogilvie, D. Swan, A. Vander Molen, G.D. Westfall, W.K. Wilson, J. Winfield, and J. Yurkon

Bragg-curve spectroscopy (BCS) is a technique that allows one to identify the charge (Z) of highly ionizing fragments without sacrificing the lowest energy data, as is necessary if one uses a ΔE detector.[1] One constructs a gas-ionization chamber such that the drift field is parallel to the trajectories of the incident fragments. The charge collected at the anode generates a signal whose height as a function of time represents the ionization density as a function of position. The signal thus is a representation of the Bragg-curve ionization pattern created as the particle is stopped within the chamber. The peak at the end of the ionization pattern is proportional to the Z of the particle.

Previously, most detectors of this sort have covered small solid angles[2,3,4]; thus, the detected particles were all incident normal to the entrance windows of the device. The technique has been extended to large solid-angle Bragg-curve counters (BCC's) which are suitable for use with a 4π array designed to detect highly ionizing fragments.[5,6]

We have constructed and tested BCC's designed to be operated in the MSU 4π array. These detectors cover a large solid angle (400 msr) and handle satisfactorily particles that are not normal to the entrance window. A field-shaping grid was installed on the inner walls of our BCCs to approximate a radial field. The entrance window is 900 μg/cm^2 Kapton, which allows heavy ions with as little as 100 keV/n to enter the detector. The peak of a particle's Bragg curve must occur within the detector for the particle to be identified, thus the identification threshold is 1 MeV/n for heavy ions. The chamber is designed to run at 500 Torr of P5 (95% Argon, 5% methane) with -1000 V on the cathode and +120 V on the anode. The anode of the exit window is a 2.5μm aluminum layer, which has been evaporated directly onto the surface of the fast plastic scintillation element of the phoswichs, which makes up the final stage of the 4π detection system. Thus, particles which exit the BCC's are still identifiable.

We have tested the first production model BCC/phoswich module for the MSU 4π array in an experiment using the K500 cyclotron. A test box which contained the module and a target ladder was positioned behind the 10° exit port on the S320 spectrometer.

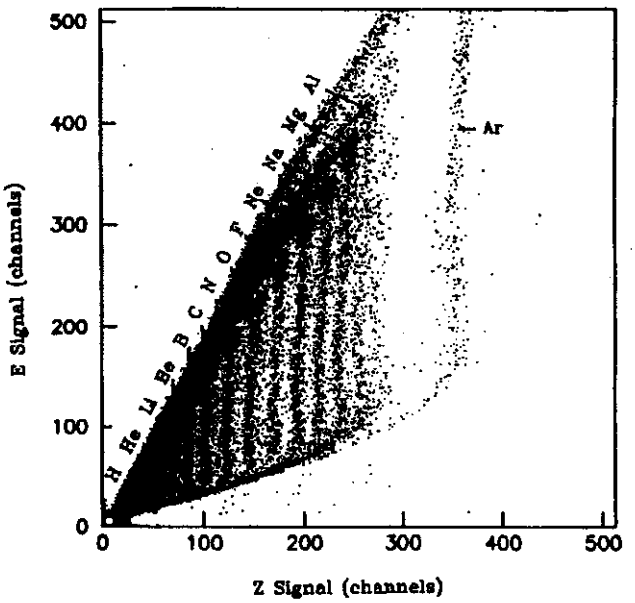

FIG. 1: Plot of Z signal against E signal for the first production Bragg curve detector.

In order to measure the energy resolution of the BCC, a beam of 4 MeV/n ^{40}Ar was stopped in the gas detector. The energy resolution is the ratio of the peak width at half maximum to peak position. We measured the resolution at 2%. In order to study the Z resolution, a beam of 35 MeV/n ^{36}Ar was stopped in a target 15 cm upstream of the detector, causing the exiting fragments to illuminate the entire face of the detector. In Fig. 1 a plot of the fragment charge versus the energy is displayed. The width of the Z lines remains constant as Z increases; for Z=14, one measures a 4% resolution (FWHM/position). These resolutions compare favorably with the best resolution attained for small solid-angle BCC's.[7]

Figure 2 displays a plot of light produced in the fast plastic scintillator against the energy signal from the BCC. This is a standard ΔE-E plot, with the gas detector acting as the ΔE detector and the first scintillation element of the phoswichs acting as a stopping scintillator.

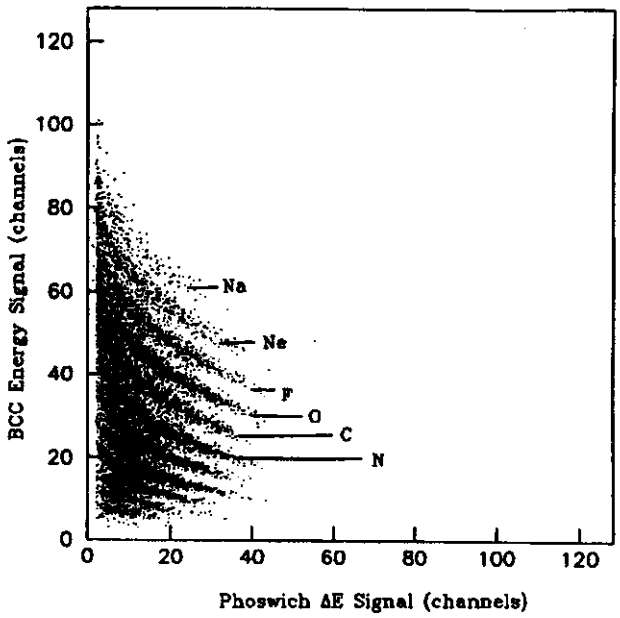

FIG. 2: Plot of the fast phoswich signal against the Bragg curve E signal for particles stopping in the scintillators.

Clearly, charge identification is maintained up to sodium, where the data end. For this plot, the 35 MeV/n ^{36}Ar was stopped in a target on the S320 target ladder, and the spectrometer was tuned to accept outgoing fragments with about 35% of the original beam rigidity. This range corresponded to particles penetrating into the BCC's but not the fast plastic scintillators.

We have constructed Bragg-curve detectors in a novel and demanding geometry. These detectors compare very favorably in terms of both energy and charge resolution to others built with fewer constraints. In addition, these detectors have a much greater dynamic range because they are backed by scintillation detectors. The 4π modules are thus capable of detecting and identifying particles with energies from 1 MeV/n up to 200 MeV/n.

References

a. University of Iowa.

1. C. Gruhn *et al.*, Nucl. Instrum. Methods 196, 33 (1982).

2. R. Kotte *et al., ibid.*, 257, 244 (1987).

3. A. Moroni *et al., ibid.*, 225, 57 (1984).

4. K. Kimura and H. Tomura, *ibid.*, 254, 583 (1987).

5. R. MacDonald *et al., ibid.*, 219, 508 (1984).

6. G.D Westfall *et al., ibid.*, 238, 347 (1985).

7. M. Vineyard *et al., ibid.*, 255, 507 (1987).

4π-Miniball Detector

R.T. de Souza, N. Carlin, Y.D. Kim, C.K. Gelbke, W.G. Lynch, R. Pelak, L. Phair, and M.B. Tsang

Phase II experiments at the NSCL will increasingly require instrumentation capable of large-phase-space coverage. In order to perform studies of intermediate-mass fragment emission and search for the onset of multifragmentation reactions at Phase II energies, with event-by-event information about charged particle emission patterns, we are designing and constructing a compact, transportable 4π-detector, consisting of 188 phoswich detectors which are capable of identifying fragments up to $Z \approx 15$.

The detector utilizes basic concepts developed by the Washington University group for the Dwarf-Ball.[1] The individual detector elements will consist of 20-mm-thick CsI(Tl) crystals covered by thin (40-100μm) plastic scintillator foils. The scintillation light will be detected by photomultipliers and encoded by FERA ADC's for three different time gates:

i. a fast (≈50 ns) time gate placed on the signal of the fast plastic scintillator,

ii. an intermediate time gate (≈60-400 ns) placed on the fast CsI decay component, and

iii. a long time gate (≈1-2 μs) placed on the long decay component of the CsI signal for pulse shape discrimination of light particles.

Compared to the existing 4π array, the instrument has the following characteristics:

1. The detector is small. This has the advantage that it allows one to surround the array with a 4π-neutron multiplicity detector, which will permit full multiplicity coverage for both charged and neutral particles on an event-by-event basis. The small size, however, carries an associated disadvantage because the dynamic range for energy measurements of light particles in this device is reduced.

2. The array has a large number of detector elements capable of identifying intermediate mass fragments. This high granularity reduces multiple hits which cause pile-up and misidentification of fragments.

3. The geometry is simple; individual detectors will be arranged in rings corresponding to Θ= const. Solid angles increase from forward to backward angles. This design allows for the fact that particle multiplicities and energies increase at forward angles.

4. The detector is mechanically robust since it does not involve thin gas detector windows. It is therefore easy to reconfigure or transport.

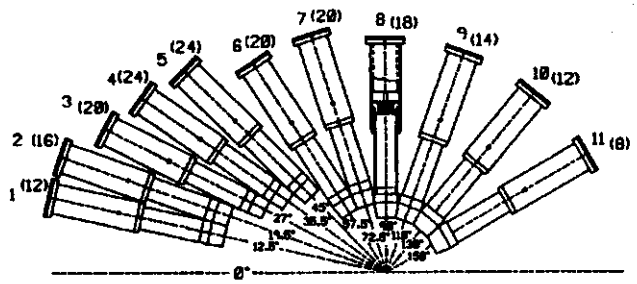

FIG. 1: Half-plane section of the Miniball array. Individual detector rings are labeled 1 through 11; numbers of detectors per ring are given in parentheses.

The conceptual design of the detector array has been finalized, and Monte Carlo simulations for cross talk and misidentifications due to coincidence summing have been performed. Figure 1 shows a half-plane section of the array. The array consists of 11 rings of detectors located at the polar angles indicated in the figure. The numbers in parentheses indicate the number of elements per ring. Figure 2 shows a schematic of the three dimensional detector geometry; each ring of detectors corresponds to an independent assembly which will be mounted on rails for ease of service. Figure 3 shows front views of the different detector shapes. The individual detectors are identified by the ring numbers defined in Fig. 1; the numbers in parentheses indicate the number of detectors for a given ring.

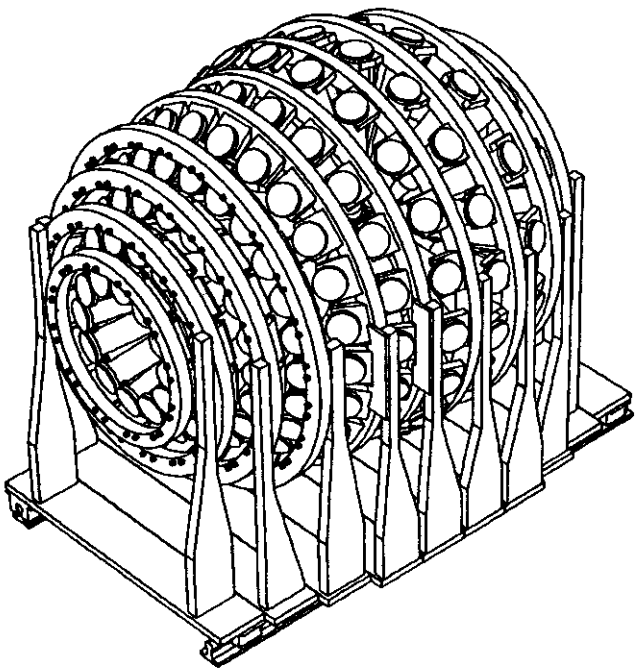

FIG. 2: Schematic of three-dimensional detector geometry.

Prototype detectors have been tested with promising results; particle identification up $Z = 18$ has been obtained.

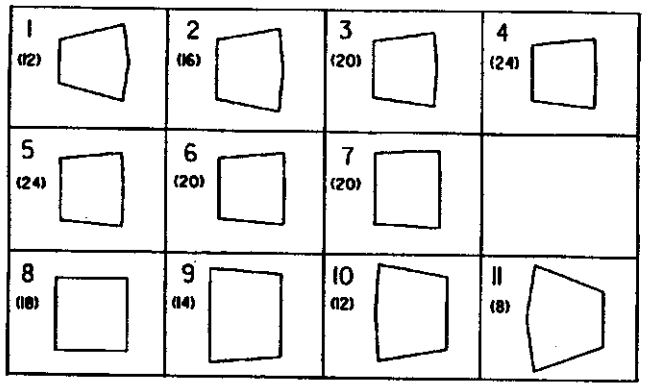

FIG. 3: Front views of different detector shapes. The detectors are labeled by their ring number; numbers of detectors per ring are given in parentheses.

At this time we are working on details of the mechanical design and fabrication. No major technical difficulties have surfaced up to now, and we have started the acquisition of hardware components.

References

1. D.G. Sarantites *et al.*, Nucl. Instrum. Methods A264, 319 (1988). The fast-slow plastic phoswich elements of the original device were replaced by plastic-CsI(Tl) phoswich elements.

Quality Tests of CsI(Tl) Scintillators

R.T. de Souza, W.G. Gong, N. Carlin, C.K. Gelbke, Y.D. Kim, and W.G. Lynch

The use of Cs(Tl) detectors has attracted attention in the recent past, both for its excellent pulse shape discrimination characteristics useful for particle identification, and for its capabilities as a total energy detector for the detection of energetic light charged particles.[1-7] Two detector systems at NSCL currently utilize CsI(Tl) crystals. Development of bench tests to determine crystal quality has been essential to the development of these devices.

One of these two systems is a 56-element hodoscope for detection of energetic light ions from intermediate-energy heavy-ion collisions. In each element of the hodoscope, there is a totally planar silicon-surface barrier detector, backed by a cylindrical crystal of CsI(Tl), which is 38 mm in diameter and 102 mm long. Since the spectral response of CsI(Tl) scintillators is well matched to that of silicon photodiodes, which exhibit excellent long-term stability, the CsI(Tl) scintillators for this device have been coupled to Hamamatsu silicon photodiodes.

Initially, good energy resolution was obtained only for selected detectors.[7] The resolution of other detectors was found to be limited by local crystal non-uniformities, which caused local variations of the light output efficiency.[7] The magnitude of these variations of light output efficiency can vary significantly between individual crystals. These variations were assessed by a bench test in which the position-dependent response to collimated γ-rays was measured.[7] In this note we report test results for two large sets of CsI(Tl) crystals manufactured by BICRON Corporation.

All crystals tested were cylinders, 38 mm in diameter and 102 mm long. A clear lucite light guide, 12 mm long, connected the rear flat surface of each CsI(Tl) crystal to a square-shaped PIN diode of 400 mm^2 active area, manufactured by Hamamatsu corporation. The outer surfaces of the crystal and light guide were sanded with fine (#320-#400) paper. White teflon tape was wrapped around the sides of the detector assembly and the front face of the crystal was covered by aluminum foil, 17μm thick. An opaque aluminum foil was wrapped around the layers of teflon tape. The detector was then inserted into an aluminum can, which provides mechanical protection, and the housing of the preamplifier.[7]

The response of all detectors was tested with 662-keV γ-rays from a ^{137}Cs source collimated by a 3-mm-diameter lead collimator, about 6 cm thick. The collimated γ-rays entered through the flat front face of the CsI(Tl) crystals in a direction parallel to the cylinder's axis. As a quantitative measure for the non-uniformities of scintillation response, we evaluated the maximum shift of the centroid of the photopeak as the collimator circled around the cylindrical CsI(Tl) crystals at a radius of 1 cm. The measured shifts of the photopeak were normalized to the response for irradiation at the center of the circular entrance window. More details of this test are given in Ref. 7.

Two different sets of crystals were tested. The first set of crystals was grown in a large production furnace. The second set of crystals was grown in a smaller, better-controlled research furnace, and a more careful material purification technique was employed.

Figure 1 shows the results obtained for the two sets of crystals. The test results for crystals grown in the large production furnace are shown by the unshaded histogram. These scintillators exhibit a broad distribution in scintillation uniformity corresponding to a broad spread in scintillator quality. There is a close relation between scintillation uniformity and energy resolution when photon statistics or electronic noise cease to be limiting factors. When used for the detection of energetic light charged particles, most of these crystals will yield detectors with only modest energy resolution.

The test results for crystals grown in the small research furnace are shown by the shaded histogram. These scintillators exhibit much better scintillation uniformity, sug-

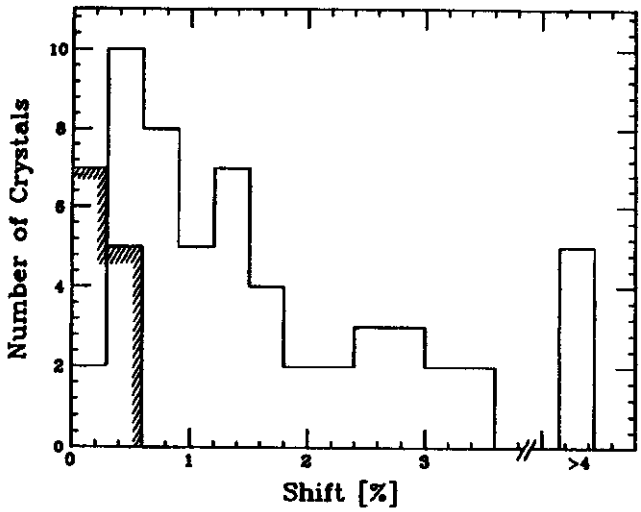

FIG. 1: Maximum variations of scintillation response observed for collimated γ-rays entering the detector front face as it circled around the detector axis, at radius 1 cm. The shaded histogram shows the measurements for detectors produced with the new purification technique; the unshaded histogram shows measurements for detectors fabricated with standard techniques.

gesting that controlled growth conditions and careful material purification may be important factors for the production of high quality CsI(Tl) scintillators.

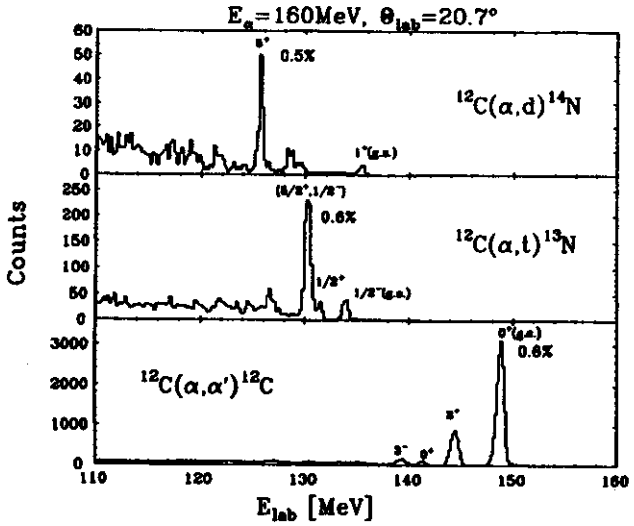

FIG. 2: Energy spectra measured with CsI(Tl) detectors produced in the research furnace.

Figure 2 illustrates the energy resolution which can be obtained with good-quality CsI(Tl) scintillators. The energy spectra were obtained by irradiating a polycarbonate foil with α-particles of 160 MeV incident energy. For these measurements, a ΔE-E detector telescope was used, which consisted of a 300-μm-thick planar silicon ΔE-detector and a CsI(Tl) E-detector from the set of crystals manufactured with the small research furnace. The sharp peaks resulting from the $^{12}C(\alpha,d)$, $^{12}C(\alpha,t)$ and $^{12}C(\alpha,\alpha)$ reactions indicate excellent detector resolutions of 0.5-0.6% fwhm. For this particular CsI(Tl) crystal, a maximum peak shift of 0.6% was measured with our bench test. The measured electronic noise was 300 keV. The gain stability of these detectors was found to be better than 0.5% over a period of three weeks.

The second detector system under construction at the NSCL is a 4π phoswich array referred to as the Miniball. The Miniball is a 188-element phoswich array. Each phoswich consists of a 40- to 100-μm-thick fast-plastic element optically coupled to a 20-mm-thick CsI(Tl) crystal. The geometric shapes of the crystal are approximately trapezoids with front faces which could be approximated as 2 cm×2 cm squares. The light generated by the passage of the heavy ion through the fast plastic and into the CsI(Tl) is detected by a 1-inch-diameter photomultiplier tube (Burle Industries C38062E). Unfortunately, photodiode readout would not permit a separation of the signals from the plastic and CsI(Tl) scintillators, and therefore photodiodes cannot be employed.

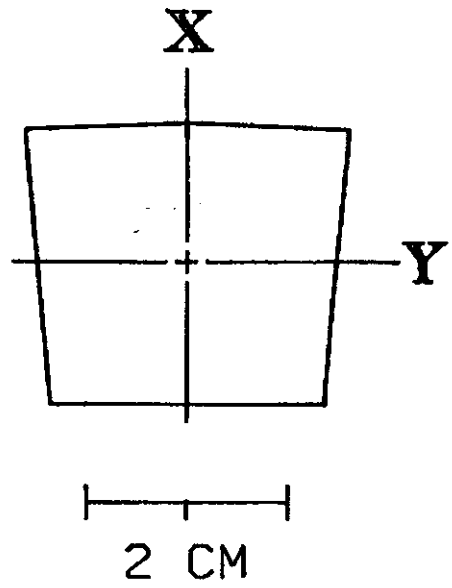

FIG. 3: Designation of the coordinate system used in the scanning with alpha particles and gamma rays.

To measure the uniformity of the response of the CsI(Tl) crystal, the collimated ^{137}Cs gamma scanning technique described above was performed. The crystal was scanned starting from the center moving orthogonally in x and y directions, as shown in Fig. 3. The asymmetries observed are reported in Fig. 4. In addition, the crystal was scanned with 8.785-MeV alpha particles from a ^{228}Th source, retaining the same absolute orientation as in the gamma scan. In the alpha scanning test, the sensitivity of the measured asymmetry to various crystal front coverings (aluminized mylar, double aluminized mylar, and intransparent aluminum) was investigated.

As long as even a very thin specular reflector was used for the front face of the crystal, the measured asymmetry was unchanged. The reproducibility of the alpha scanning was 0.3%. The fact that the measured asymmetry qualitatively tracked with the asymmetry measured with gamma rays, which average over a larger crystal volume, clearly demonstrates that the non-uniform response was not simply a surface treatment effect. Indeed, the asymmetry was also reproduced by impinging the alpha particles from the back of the crystal and collecting the scintillation light from the front.

By this test procedure, crystals could be selected which had a non-uniformity of response of less than 2% (maximum deviation). Four such crystals were assembled into elements of the Miniball by optically coupling them to 40(±2%)-μm fast-plastic foils spun from BICRON Beta paint. A front

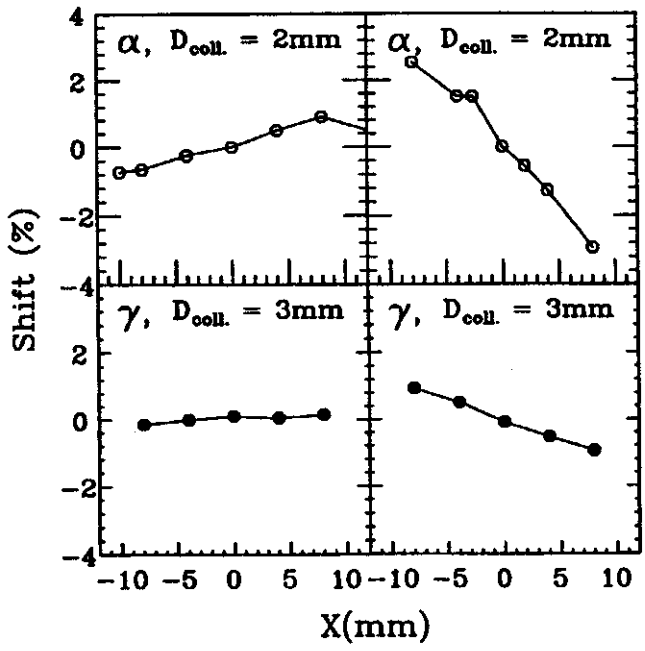

FIG. 4: Typical asymmetries observed in the testing of CsI(Tl) crystals. Examples of crystals with varying degrees of asymmetry are shown.

cover of 0.38 Al was used. In a beam test of 8.5-MeV/u-^{40}Ar projectiles on a ^{27}Al target, fragments from $Z=1$ to $Z=18$ were clearly resolved in all four detectors.

In summary, bench tests have been developed which allow determination of the performance of the CsI(Tl) crystals. This tests a preselection of CsI(Tl) crystals without resorting to extensive beam tests. Our tests indicate that detectors constructed from large CsI(Tl) crystals can exhibit excellent energy resolution and even stability when a photodiode readout is utilized.

This work was supported by the National Science Foundation under Grant No. PHY-86-11210.

References

1. E. Blucher *et al.*, Nucl. Instr. and Meth. A249, 201 (1986).
2. G. Viesti *et al.*, Nucl. Instr. and Meth. A252, 75 (1986).
3. R.J. Meijer *et al.*, Nucl. Instr. and Meth. A256, 521 (1987).
4. P. Kreutz *et al.*, Nucl. Instr. and Meth. A260, 120 (1987).
5. H. Grassmann, E. Lorenz, and H.G. Moser, Nucl. Instr. and Meth. 228, 323 (1985).
6. H. Grassmann *et al.*, Nucl. Instr. and Meth. 234, 122 (1985).
7. W.G. Gong *et al.*, Nucl. Instr. and Meth. A268, 190 (1988).

Automated Analysis of CCD-Recorded Nuclear Collisions in a Streamer Chamber

D. Krofcheck, G.M. Crawley, C. Djalali[a], S. Howden, C.A. Ogilvie, A. Vander Molen, G.D. Westfall, W.K. Wilson, and R.S. Tickle[b]

The study of high-energy nucleus-nucleus collisions has benefitted greatly from the use of 4π detector systems, such as the Lawrence Berkeley Laboratory Streamer Chamber.[1] Recent work performed with this device includes measurements of transverse momentum[2] and negative pion multiplicities[3]. However, major operational drawbacks with the streamer chamber still exist, such as the low rate at which pictures of nuclear collisions are acquired and the long time needed to analyze the pictures. The MSU streamer chamber group has attempted to solve the latter problem through the use of a charge-coupled device (CCD) camera system.[4] These cameras make digital recordings of the collisions, which are subsequently image-enhanced and analyzed. Here, we report on the progress in the development of operator-independent CCD picture analysis software.[5]

The automated analysis software is divided into three main steps encompassing nuclear fragment track recognition, pre-matching/reconstruction, and mass identification.

In the first step, the CCD picture is enhanced by performing a double differential with respect to the beam axis using the collision vertex as the origin. This eliminates most of the background light due to flares or reflections. The processed image is then scanned to search for sections of a track. Any candidate track sections are checked for the following properties: divergence from the track vertex, an approximately circular arc shape due to the presence of the chamber's magnetic field, a narrow track width, and a nearly Gaussian intensity distribution across the track width. If the candidate track sections meet these criteria, the sections are used as a template for a third-order polynomial fit to determine the full nuclear fragment trajectory.

After the three camera views have been scanned for tracks, the pre-matching/reconstruction step begins. Pre-matching of a given track in each of the three camera views is accomplished by comparing deduced properties of the found tracks. Primary pre-matching criteria include: the slope in each view of the fitted track at the collision vertex with respect to the beam direction, the arc length of the track, and the slope of each track at its endpoint.

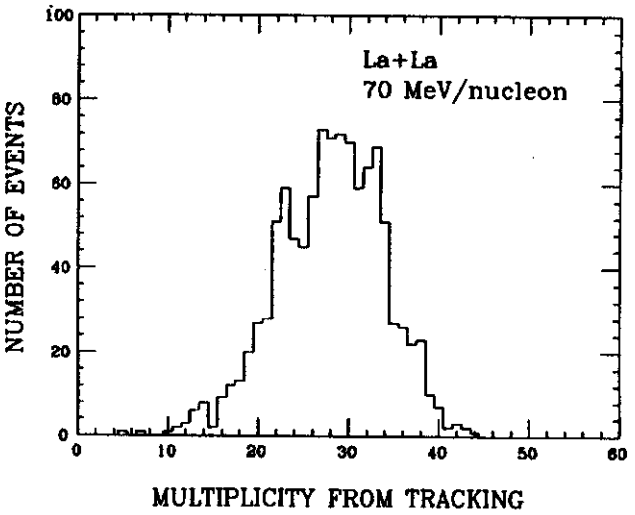

FIG. 1: The distribution of the number of fragment tracks found using the tracking step in the automated analysis.

If no pre-matches are found for a given track, then secondary and tertiary criteria are applied. Respectively, these criteria are the slopes and track curvatures at the collision vertex, and track slopes and intersections at imaginary planes perpendicular to the beam direction.

If a given track appears in several of the three-view matches, the Three View Geometry Program[6] is used to select the actual match. This is done by placing restrictions on the reconstructed track momentum and the extrapolated origin of the track, as well as comparing the track to an idealized 3D curve.

The performance of the tracking and pre-matching/reconstruction steps is illustrated in Figs. 1 and 2. The tracking step typically finds at least 90% of the

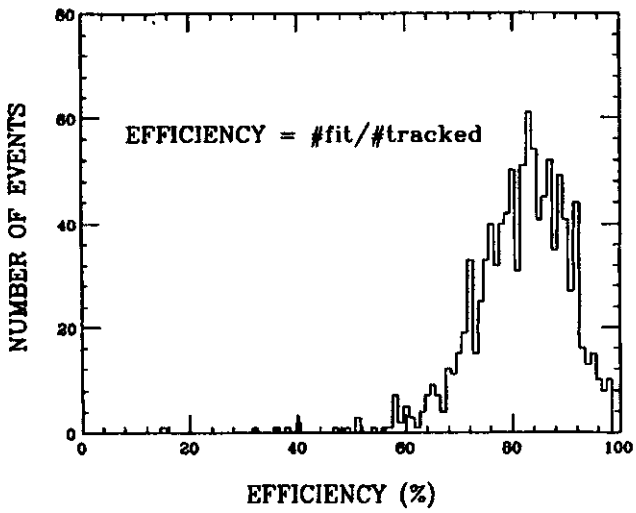

FIG. 2: The fraction of the found tracks in the best camera view which are used in the 3D reconstruction. This number is never greater than 100% because the pre-matching reconstruction step can only work with the tracks found in the previous step.

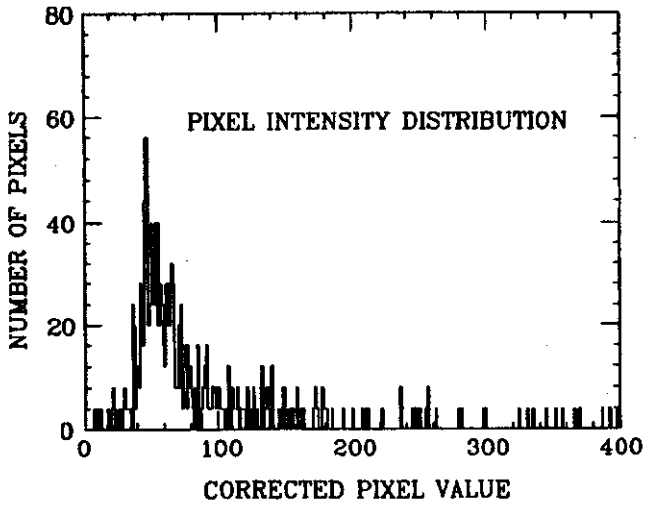

FIG. 3: A distribution of spatially-corrected pixel intensity values for a reconstructed track. This distribution is fit with a Landau distribution line shape which yields a peak position that represents the average pixel-light intensity of the track.

visually-confirmed tracks, while the pre-matching/reconstruction step can reconstruct 85% of the found tracks.

The mass identification step in the automated analysis software relies upon the analysis of pixel-light intensity values recorded along the nuclear fragment's track. Corrections are made to these values to account for spatial effects due to the changing distance and orientation of the tracks with respect to the cameras. Figure 3 shows how an average pixel-light intensity value is then assigned to each reconstructed track. Final corrections are applied to the track average values to compensate for central electrode-grid screening and Marx-generator voltage fluctuations. The corrected pixel-light values are related to the nuclear fragmentation masses:

$$I \sim (m/R)^n \qquad (1)$$

where I is the corrected pixel-light value measured for the reconstructed track, m is the fragment mass, R is the fragment rigidity, and n is an exponent which is chosen to fit the data.

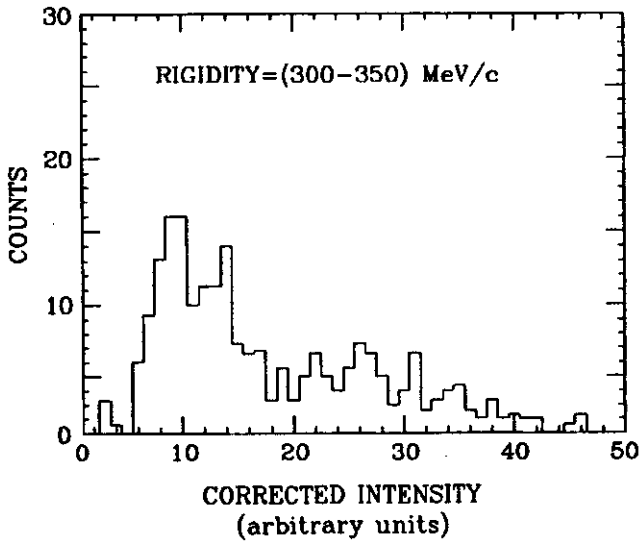

FIG. 4: A rigidity cut is placed on the particle identification spectrum. This plot shows indications of the presence of beam velocity protons.

Figure 4 shows the result of the mass-identification step for the reaction La+La at 70 MeV/nucleon. The rigidity cut for this figure contains a strong contribution from beam velocity protons. Definitive statements about the exact mass locations in Fig. 4 must await the use of an energy-calibrated, low-mass beam to generate better statistics.

References

a. University of South Carolina
b. University of Michigan

1. K. Van Bibber and A. Sandoval, *Heavy Ion Science,* ed. D.A. Bromley (Plenum, New York, 1982), IV.

2. P. Danielewicz *et al.,* Phys. Rev. C38, 120 (1988).

3. J.W. Harris *et al.,* Phys. Rev. Lett. 153B, 377 (1985).

4. S.P. Angius *et al.,* Nucl. Instrum. Methods A273, 283 (1987).

5. D. Krofcheck *et al.,* submitted to Nucl. Instrum. Methods.

6. F.J. Somitz, A.D. Johnson and T.B. Day, *LBL Alvarez Group Programming Note P-117,* 2nd ed. (1966).

Recent Developments with the Reaction Products Mass Separator (RPMS)

R. Harkewicz, D. Mikolas, D.J. Morrissey, J. A. Nolen, B. Sherrill, and D. Swan

The Reaction Products Mass Separator (RPMS) at NSCL is a device which physically separates heavy-ion reaction products according to their mass-to-charge ratio, and focuses them to a small spot in the focal plane where detectors can be located. The RPMS has been used in a number of decay studies involving nuclei far from stability.[1-3] A detailed description of the device can be found in Ref. 1.

In this report we discuss developments that have taken place during the past year in the areas of RPMS beam diagnostics, detector hardware development, and lastly, upgrade of the RPMS during the present reassembly.

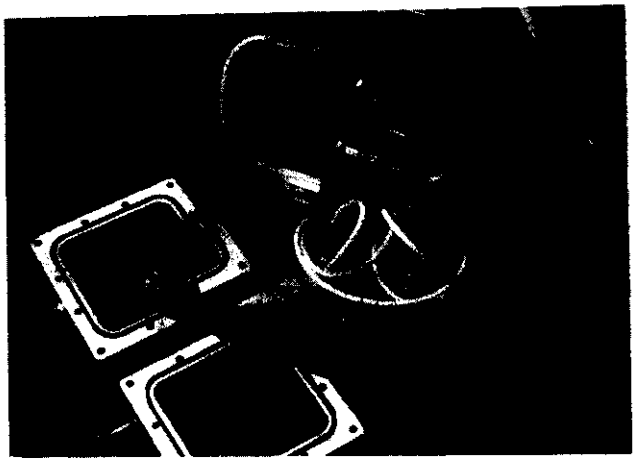

FIG. 1: Position-sensitive gas counter detector used at the focal plane of the RPMS to determine the position of ions transported through the device. Two chambers of resistive-division single-wire counters can determine the position of ions to accuracy of 1 mm.

To better understand the transport of ions through the RPMS, a two-dimensional position-sensitive detector has been designed and constructed. A photograph of this detector is shown in Fig. 1. The detector is usually placed in the vacuum chamber at the focal plane, has a square active area (2" × 2"), and is electrically isolated from beamline ground. The detector has all-aluminum body components which are assembled together using O-rings and Reynolds high-voltage electrical feedthroughs; this provides glue-free assembly and relatively quick repairs when necessary. The detector is divided into two chambers, with one resistive 0.3-mil-diameter Nicrome wire crossing the center of each chamber, horizontally and vertically. The detector typically operates with isobutane at a pressure of 35 Torr. The three windows of 1.5-micron-thick aluminized mylar (the center window is aluminized on both sides) make the detector nearly transparent to high-velocity, light reaction products.

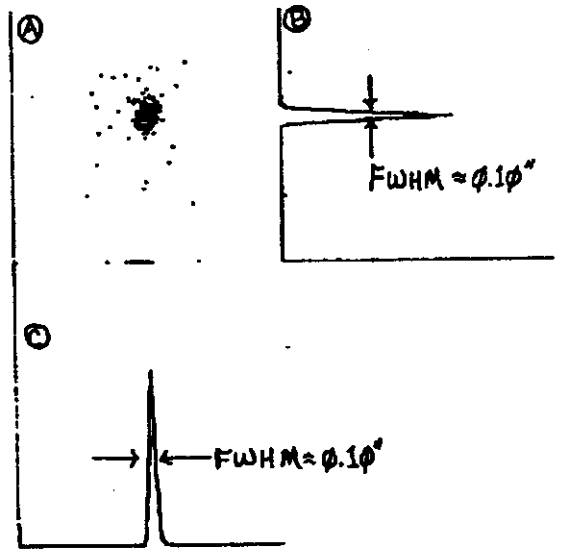

FIG. 2: (A): Two-dimensional image obtained on position-sensitive gas counter-detector placed at the RPMS focal plane with ^{241}Am source placed in RPMS target chamber (see text). (B) and (C): One-dimensional projections of the data in (A).

Off-line diagnostic measurements have been performed by placing an ^{241}Am source (approximately 0.10" diameter) in the target chamber of the RPMS and focusing the 5.5 MeV alpha particles from the source on the gas detector. Figure 2 shows the alpha particle pattern obtained using the position-sensitive gas counter-detector. Note that the image size obtained has a FWHM of 0.10" in both the x and y dimensions; this is approximately the source size.

From these tests we have found that there is a horizontal optical misalignment of approximately 0.6 cm in the target position. During reconstruction of the RPMS (discussed in more detail below) this problem will be corrected.

The results of actual ion transport through the RPMS can be compared to computer predictions. The new beam optics program, GIOS, for General Ion Optical Systems, which can handle Wien filters, is now being used.[4] It allows optimization of the Wien filter parameters, and has graphical output of the results. In the future, we plan to use on-line low-intensity calibrated beams to increase our knowledge of ion transport through the spectrometer. We will develop a kinematics program for RPMS operations, including scaling predictions for all the settings of the device.

During the past year, the focal plane region has been modified to allow a multi-element silicon detector telescope (with up to 10 detectors) to be operated in vacuum, cooled to -20°C. Figure 3 is a photograph of this detector holder, with some silicon detectors. Prior to this modification, the separated products from RPMS experiments had to pass through a thin kapton window which separated the focal-plane detectors (operated in air) from the rest of the RPMS.

Recent vault reconstruction at the NSCL, necessary for the implementation of the experimental areas for the new K1200 cyclotron, required that the RPMS be disassembled and moved. At present (June, 1989) a new experimental vault for the RPMS is nearly complete and reassembly of the spectrometer will commence shortly. While the RPMS is still in its disassembled state, its voltage holding capability is being tested to determine why the device has experienced problems with voltage discharge from the electrical plates of its Wien filter. The most recent experiments were run with plate biases of ±75 kV; the original design of the device should be able to sustain three to four times this voltage. We expect that the cleaned and revamped RPMS will be ready for experiments in the fall of 1989.

FIG. 3: Multi-element silicon detector-telescope-holder which allows for detectors to be operated in vacuum and cooled to -20°C. The detectors are cooled by refrigerated alcohol, which circulates through the tube at left.

References

1. M.S. Curtin *et al.*, Phys. Rev. Lett. 56, 34 (1986).
2. D. Mikolas *et al.*, Phys. Rev. C37, 766 (1988).
3. M. Samuel *et al.*, *ibid.*, 1314 (1988).
4. H. Wollnik, *Manual for GIOS* (1988).

S320 Spectrograph Improvements

M.F. Mohar, S. Bricker, M. Maier, D.J. Morrissey, B.M. Sherrill, D. Swan, J.S. Winfield, and J. Yurkon

Introduction

In the past year the S320 spectrograph has been modified and upgraded to expand its capabilities and enhance its operation. While some of the improvements were made with specific experiments in mind, many of the modifications were made to improve the overall operation of the device and to allow for prototyping of the S800 spectrograph detector design and control system.

Alignment and Optics

A test run showed some alignment problems in the spectrograph, and after sighting with a transit back to the Hunter's Point magnet, it was found that the target ladder was out of alignment 2 mm to the right of center (facing towards the focal plane). Therefore, a new scintillator was made with the true alignment for a focus at the target position.

Because of the alignment compensation and the installation of new magnet power supplies, a short test run was performed prior to the next experiment to determine the optimal settings of the quadrupole doublet, dipole, sextupole, and octupole magnet supplies. The tests were carried out using E/A=8 MeV ^{36}Ar elastic scattering, and the results were incorporated into the spectrograph settings code S320.[1]

Control System

Most of the controls for the S320 spectrograph originally were switches and dials on the old K500 beamline console. When the console was removed in 1988, all of the 110V on/off outlet controls were incorporated into the Modicon system. The potentiometer control of the magnet power supplies was taken over by the Fermi station system.* The target ladder height and rotation and the aperture ladder controls remained in the stand-alone Data-U2 controller box. However, to unify the control system throughout the lab, the old system is being replaced with bang-bang servo motors to be interfaced with the Fermi system. By interfacing these spectrograph parameters to the Fermi control system, more flexible remote control is now possible. More important for a spectrograph experiment, this interfacing enables the recording of the spectrograph parameters automatically onto the magnetic tape with the event-by-event data.

This system was tested during a March 1989 experiment. At that time, only the S320 dipole power supply and the quadrupole doublet power supplies were controlled by the Fermi system. The experimenters were able to set and monitor these power supplies not only at the new control-console Fermi station, but in Data-U2 as well. This was facilitated by a program running on the CYCLO μVAX that reads the Fermi parameters over the ARCNET interface. The experimenters were able to monitor, set, and print out the S320 magnet values at a terminal in the Data-U. They were also able to monitor and record the beamline parameters. Once the Data-U2 front-end computer is upgraded to the level of the Distant Data-U front-end, all of the Fermi parameters will be able to be periodically recorded on tape. This will eliminate human errors and will give a log of beamline and spectrograph settings for future experiments.

Focal Plane and Start Detectors

A new focal plane detection system was designed and implemented for the detection of slow heavy-ions in the spectrograph. This was part of an experiment to study the use of fusion/evaporation reactions to produce proton-rich nuclei far from stability. The requirements were to provide unit Z resolution in the range $20<Z<40$, to obtain time resolution of at most 800 picoseconds FWHM, and to provide position resolution of at most 1 mm FWHM.

*Fermi stations are also known as "VME stations" -- see *Phase II Control System, Foth.*

Initial tests were done using the existing focal plane system consisting of two position wires, two ion chambers with wire anodes, and a final scintillator. The gas detectors were in a common volume of isobutane gas. E/A = 10 MeV ^{40}Ar was elastically scattered from a gold target to check the position resolution, and also interacted with a titanium target to produce fusion/evaporation products.

There was a strong position dependence in the ion chamber signals that prevented resolution of the higher Z's. The position dependence of the proportional counter signal seemed to result from some interaction of the ion-induced electron avalanche with the anode wires, since there was an enhancement of the ion chamber signal pulse height at those positions where intense concentrations of elastic scattering had previously passed through the chamber. Since the wires were operated with voltages slightly into the proportional region, it is possible that the locations on the wires of the elastic scattering peaks may have been polished by the electron avalanche or the avalanche removed a deposit on the wires that may have been laid by gas polymerization. Examination of the wire chambers after the test run showed no clear evidence of wear, but the position dependence was experimentally reproducible. If the focal plane was evenly illuminated with a high intensity of particles, the gain level would come to a constant value without any positional dependence. But after a few minutes of normal operation, the response would slowly return to show an enhancement in the regions where the elastic scattering peaks had been.

After the initial test run, a new detection system for the evaporation products was designed, based on the idea that better Z resolution would be possible if the ions were ranged out in a highly segmented ion chamber. This necessitated a timing detector in front of the ion chamber, and at least two position signals so that corrections can be made for an ion's incident angle in the detector. The detector window thicknesses needed to be minimized due to the low energy of the reaction products. Also a start detector was required since the cyclotron RF timing signal gave a resolution of only about 1.2 ns FWHM.

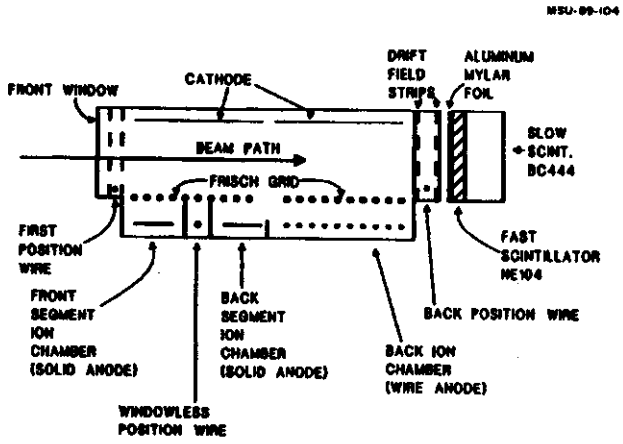

FIG. 1: Prototype S320 focal plane detector. Windows and field shaping strips are indicated.

A prototype ion chamber (Fig. 1) was built and tested using an E/A = 10 MeV ^{86}Kr beam, with the spectrograph set for elastic scattering and single nucleon transfers. The front ion chamber of the detector used in the previous test run had been divided into two sections, with anode plates instead of wires to collect the charge. The back ion chamber had the usual wire anode. Between the first and second anode plates, a new "windowless wire" resistive wire proportional counter was tested. The wire was placed in a grounded box to shield the neighboring anode plates from its higher electric field. This maintained uniform charge collection throughout the ion chamber.

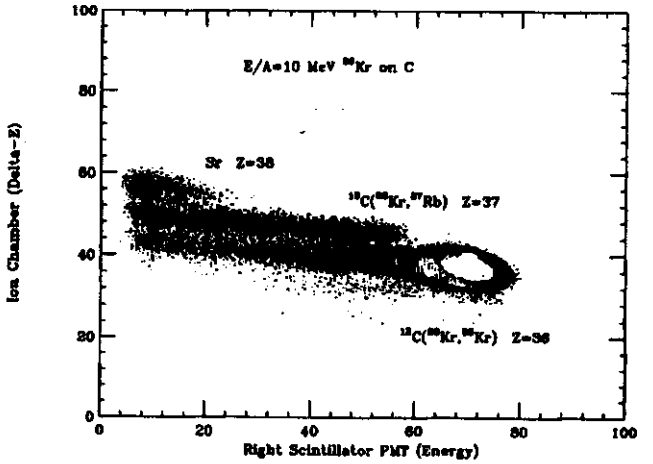

FIG. 2: Z resolution from summed ion chamber energy loss vs. scintillator energy signal using the prototype detector.

The prototype detector was ideal for testing the different ion chamber anodes and field shaping properties using various gasses and voltage settings. Two gasses were tested: pure isobutane and a mixture of 20% isobutane and 80% freon. The freon/isobutane mixture worked well and showed no sign of causing position dependences in the detector. Although the mixture does not have the gas gain of pure isobutane, it still gives an adequate signal (for slow heavy-ions). The detector, when run at classical ion chamber voltages, was able to resolve Z = 36, 37, and 38 from nucleon transfer reactions of krypton on carbon (Fig. 2).

With the encouraging results from the anode plates and the windowless position wires, the final design for the slow heavy-ion detection system was developed. The choice of the freon/isobutane gas mixture required further noise reduction in the anode signals. A separated FET preamp (Fig. 3) was developed in which the first stage amplification is mounted directly onto the anode board. This minimizes the effect of the pickup noise on the cable between the anode and the preamp, thus improving the signal-to-noise ratio.

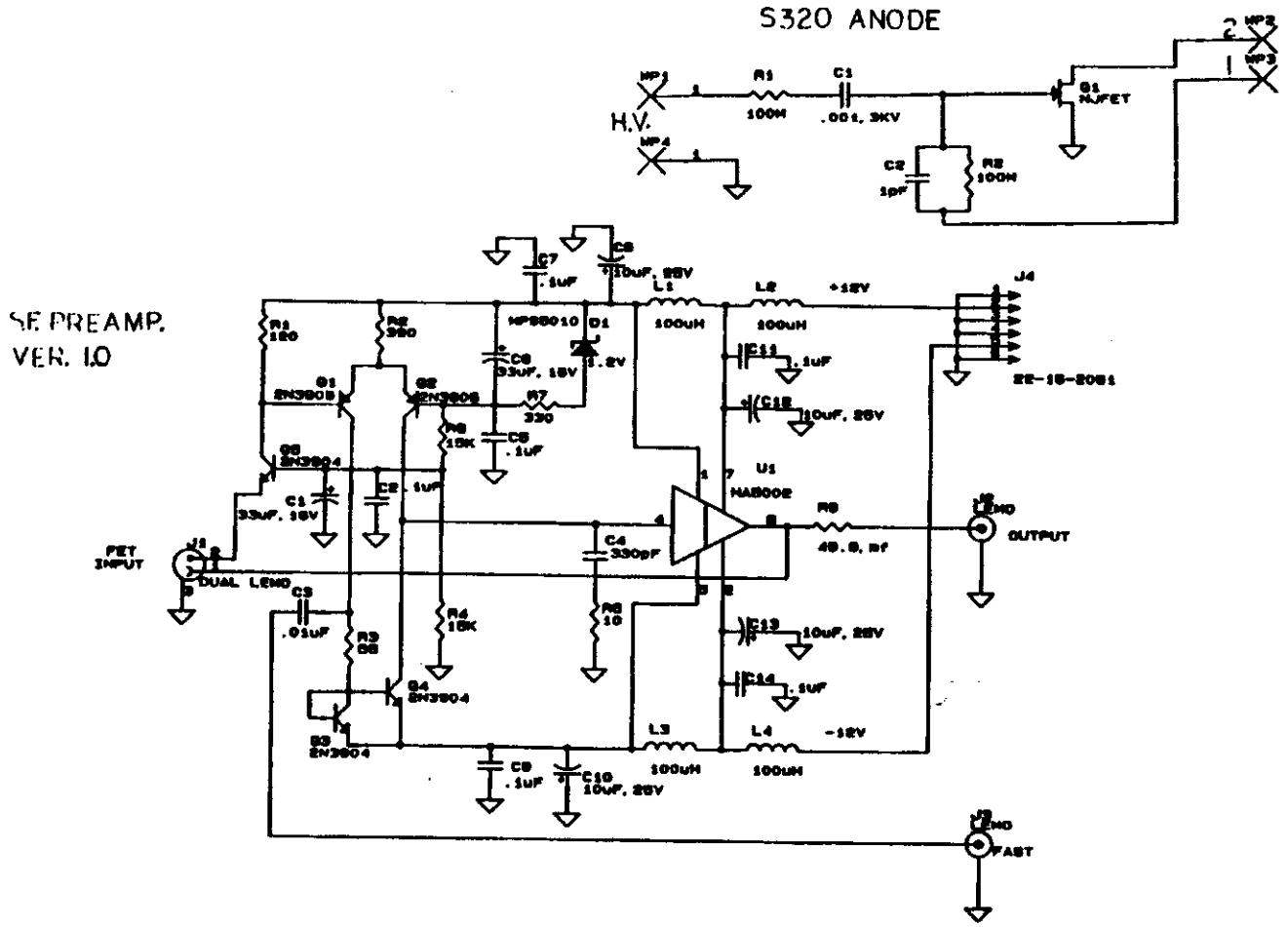

FIG. 3: Separated FET preamp schematic.

The new ion chamber incorporated 12 one-inch segments: 10 for anode strips, and two for windowless position wires. The 12 components are modular and could be replaced or reconfigured as necessary. The position wires not only give ion angle information, but also may be used to eliminate any ions that scatter out of the detector volume.

Since the ions are to be ranged out in the ion chamber volume, the first part of the detection system has to give both time of flight and position information. A low-pressure multiwire proportional counter (LP-MWPC) was designed and built, based on the design of Breskin *et al.*[2] Such a detector gives excellent time resolution, and gives position information well within the limits required for the experiment. The timing signal comes from the anode, and the position signal comes from a delay line readout of the induced charge on two layers of cathode strips that are interleaved to improve the position resolution. The time-delayed signal taken from either side of the detector (timed against the prompt anode signal) directly corresponds to the position of the ion in the detector.

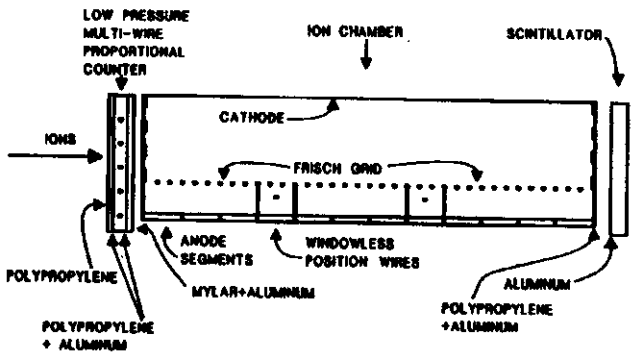

FIG. 4: Focal plane detector configuration for slow heavy ions. Window and field shaping strips are indicated. The scintillator material used was NE104.

A final diagram of the focal plane detection system is shown in Fig. 4. The back scintillator was kept to allow a broader dynamic range of Z identification.

As noted earlier, a start detector is necessary in order to obtain a time resolution of less than 800 ps. A thin scintillator foil design, based loosely on that of the wedge mounted start detector[1], was built and mounted just before the spectrograph aperture. The $< \frac{100\mu g}{cm^2}$ scintillator foil was supported by a light guide glued to the face of a photomultiplier tube (Fig. 5).

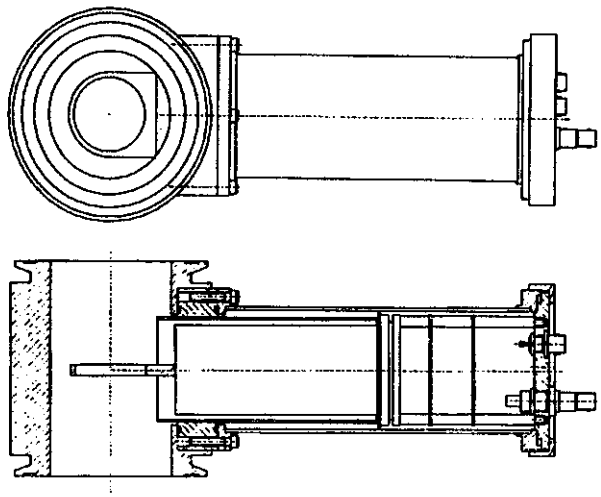

FIG. 5: Start detector. The scintillator used was BICRON BC498X.

An experiment was run in March 1989 using the slow heavy-ion detection system described in this text, and complete analysis is presently being done. However, based on early analysis and on-line results, the ion chamber gave unit Z resolution through Z=33 and the windowless wires provided position resolution of around 0.8 mm FWHM. Some aspects of the LP-MWPC are not yet fully understood; however, the timing characteristics were good (2 ns rise time) and the position resolution was adequate (about 0.72 mm FWHM). There is evidence for scattering from the LP-MWPC front window support wires and the anode wires; this is still being investigated. There was a problem with the collection efficiency of light from the start detector scintillator. Initially, it was thought that there would be enough internal reflection in the start scintillator for the edge collection of the scintillation light to give an adequate timing signal. However, on-line results during the experiment showed that this was not the case; only about 55% of the particles (averaged over all Z's) gave start detector signals above threshold. Either a more efficient means of scintillator light collection or an entirely different start detector seems necessary.

Future Work

The new N1 vault and beamline construction is being completed. The S320 spectrograph will be re-aligned with the Hunter's Point Magnet, and the target and aperture positions will be rechecked at this time as well.

The new control system for the target ladder and the aperture will also be installed. The front-end upgrade necessary to read these values to tape will soon be in place; however, a fair amount of programming must be done before the Fermi system parameters can be written to tape.

A new computerized gas handling system very similar to the 4π gas handling system is being planned for the S320 focal plane detectors. Ultimately, the gas pressures in the spectrograph detectors will be monitored and changed in the Data-U, and their values will be written to tape.

Several improvements are planned for the S320 target chamber. A stable support for the monitor detectors was designed and is under construction. This support is braced to the wall near the target chamber and enters the vacuum chamber through a bellows arrangement. At the same time, the target TV camera was changed to a small CCD type that views the target through a periscope.

Some prototyping of the S800 spectrograph detection and control systems is being done using the S320 spectrograph. The control system and gas handling system that are being designed and tested for the S320 are also a model for the S800, since the control requirements of these systems are similar for both spectrographs. Also, the Breskin-type LP-MWPC has been tested in the S320 as a prospective position and timing detector for the S800 using E/A = 40 MeV ^{12}C elastically scattered from a gold target. The data from this test are still being analyzed, but the preliminary results look unsatisfactory for S800 use.

References

1. H. van der Plicht and J.S. Winfield, *S320 Manual,* revised 1988.

2. A. Breskin, Nucl. Instrum. Methods 196, 11 (1982).

Simulations of a Low-Energy Stopped Charged Pion Detector

R.J. Radtke

One method of observing charged pions produced from nuclear reactions is to stop them in an absorber surrounding the target and then to detect the electrons produced in the subsequent muon decay by a Cherenkov detector enclosing the absorber. The effectiveness of this scheme has been studied with a simulation by the Monte Carlo code EGS (electron-gamma shower) Version 4[1], and a preliminary design for such a detector has been formulated.

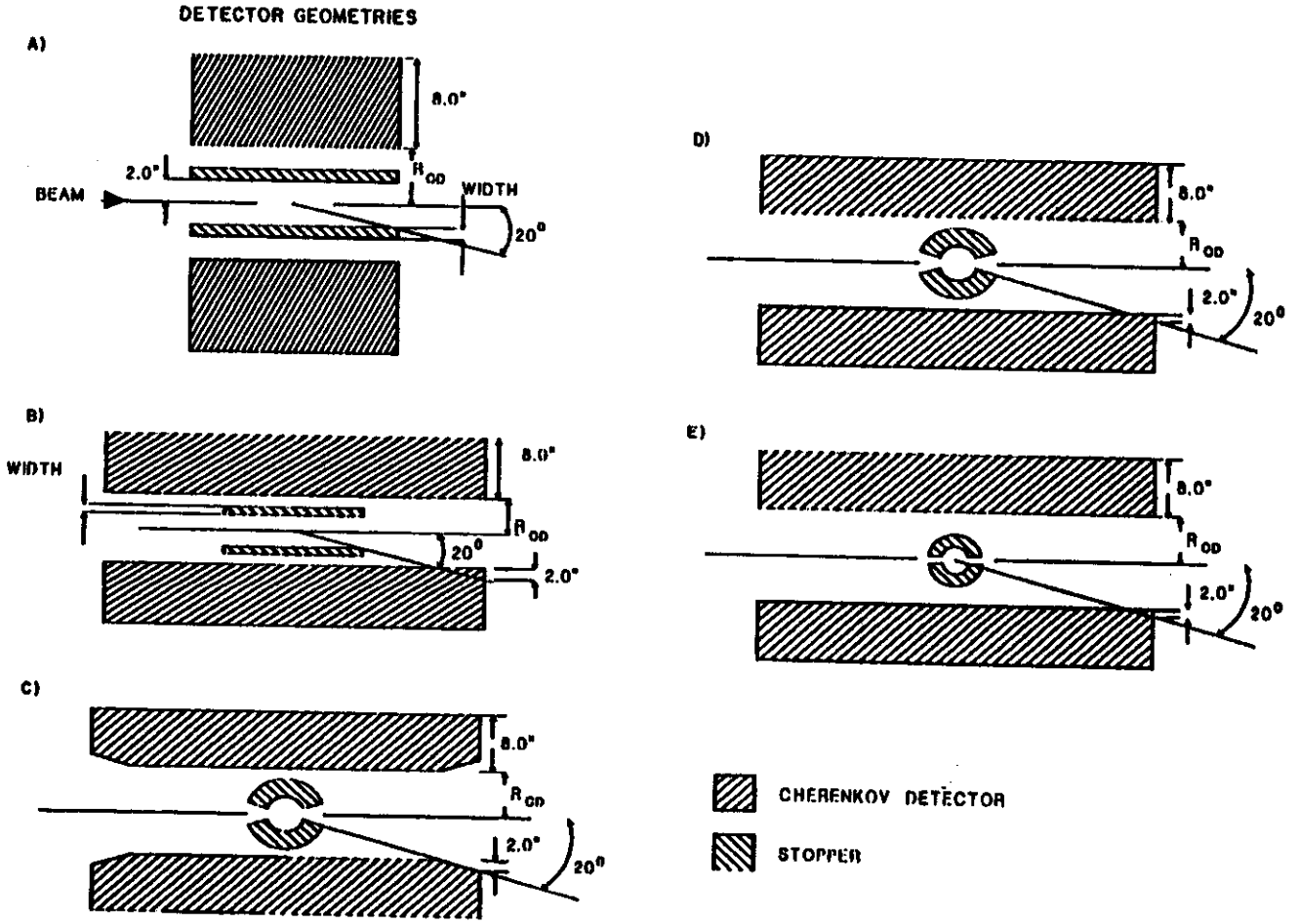

FIG. 1: Detector design geometries.

The first sequence of EGS simulations evaluated various stopping materials by calculating detector efficiency and light output for 5 MeV pions. The detector was modeled by two coaxial cylinders of infinite length, the inner representing the stopper and the outer a lucite Cherenkov detector. Pions travel radially outward from the cylinder axis to embed themselves in the stopper at a depth determined by program RANGE[2]. For the final geometry (see below), the fraction of pions that decay in-flight can be calculated and is greater than 2.5% only for low-energy (< 5 MeV) pions.

Hence, for most purposes, in-flight decay is negligible. Beryllium, lucite, mylar, boron, and carbon were evaluated, and lucite provided the highest primary efficiency and brightest light output (primary efficiency is defined as the percentage of pion decays in which the primary electron from the subsequent muon decay enters the Cherenkov stack).

The second series of calculations evaluated various detector geometries. All designs studied were constructed to detect pions between 20 and 160 degrees relative to the beam direction and use lucite as the stopping material. Cylindrical stoppers are a logical extension of the previous detector model and leave two options for the Cherenkov detector construction: either flush with the stopper [Fig. 1(a)] or extended to intercept the 20-degree exit cones [Fig. 1(b)]. Alternatively, a spherical stopper would insure even penetration of pions with similar energies, leaving detection efficiency a function of pion energy only, rather than energy and emission angle. Detectors following this design can have an unobstructed exit cone [Fig. 1(c)], and extended Cherenkov detector [Fig. 1(d)], or an extended Cherenkov detector and a stopper wrapped completely around the beam pipe [Fig. 1(e)]. Note that these designs include an allowance for low-angle electron emissions to penetrate at least 2.0 inches into the Cherenkov stack.

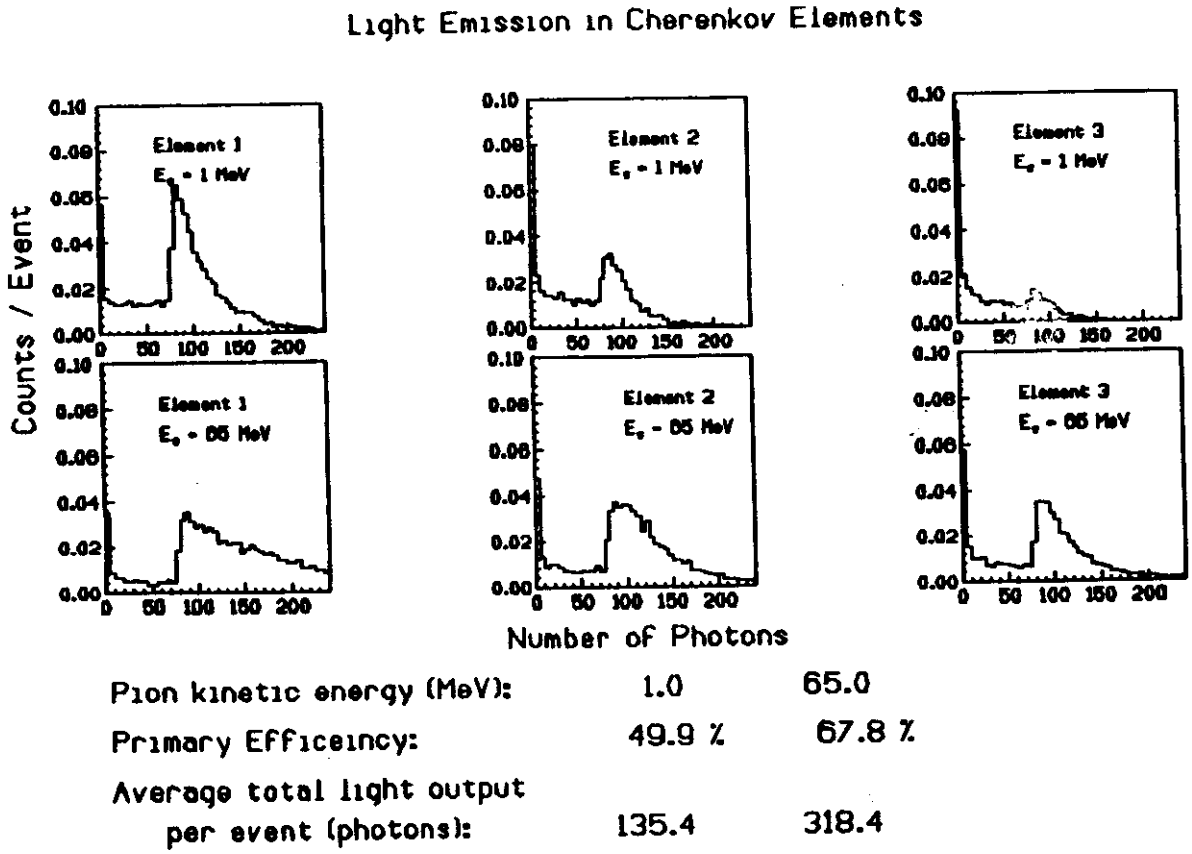

FIG. 2: Light output from Cherenkov elements from 1 and 65 MeV pions.

EGS4 calculations reveal that spherical stoppers are more efficient and produce more light than their cylindrical counterparts, and within the spherical stoppers, the addition of extra material in the Cherenkov stack yields a small improvement in efficiency, whereas additional stopper material has no effect. As might be expected, the spherical stopper behaves better at both low and high emission angles than cylindrical stoppers, although neither detector type has a strong angular dependence in its response.

The detector's sensitivity to pion energy depends critically on the stopper width. Simulations approximating the detector by coaxial infinite cylinders show clearly that a deeper stopper will stop a greater energy range of pions but strongly decreases both primary efficiency and light output. As a compromise, a stopper thickness chosen so that the primary efficiency is 50% for 1 MeV pions will contain pions up to 65 MeV with a 3.9-inch-deep stopper and operate with marginal efficiency (67.8% for 65 MeV pions) and fair light output.

Dividing the Cherenkov stack into 1.0-inch elements, the specific light output between 350 and 600 nm can be calculated.[3] Assuming a 10% photon collection efficiency in each element, Fig. 2 depicts the response of the preceding design to 1 and 65 MeV pions. At both energies, there is a low-energy photon background over which peaks are visible out to element 3 for 1 MeV pions and element 6 (not shown) for 65 MeV pions.

In addition, light output drops to half of the initial value by the second element and declines more slowly thereafter for both pion energies. Thus, using only three or four Cherenkov stack elements would decrease detector size without drastically reducing response. Moreover, further calculation indicates that reducing the inner diameter of the Cherenkov stack has no appreciable effect on efficiency and light output, so placing the Cherenkov stack close to the stopper will also reduce detector size.

Finally, since any detector must operate in a laboratory environment, kinematic effects must eventually be considered. Although sub-threshold pions are generally emitted isotropically in the nucleon-nucleon center-of-mass frame, the laboratory distribution is only approximately isotropic. To accommodate this effect, a teardrop-shaped stopper would provide optimal pion collection, but this optimum shape would change with beam energy.

In summary, a spherical lucite stopper design with an extended Cherenkov detector is the most effective in terms of primary efficiency and light output. For a 50% primary efficiency at 1 MeV, a 3.9-inch-deep stopper will contain pions up to 65 MeV relatively independent of emission angle. With an inner stopper radius of 2.0 inches, the detector has an axial length of 43.5 inches, a diameter of 20.8 inches assuming only four Cherenkov stack elements are used, and requires a beam pipe of not more than 1.37 inches diameter.

References

1. W.R. Nelson, H. Hirayama and D.W.O. Rogers, "The EGS4 Code System", *Stanford Linear Accelerator Report No. 265* (1985).

2. Program results have been confirmed for protons, deuterons, tritons, and alphas and are assumed to hold for pions as well.

3. P. Marmier and E. Sheldon, *Physics of Nuclei and Particles* (Academic Press, New York, 1969).

A Toroidal Lens for Study of Sharp Positron Lines in Heavy-Ion Collisions

J.S. Winfield, S.M. Austin, J. Bailey, E. Kashy, D. Kataria, M. Maier, and D. Mikolas

There is considerable interest in the origin of the sharp positron lines, or peaks, observed[1-3] in high-Z heavy-ion reactions near the Coulomb barrier. In spite of several years of investigation, significant experimental uncertainties remain, and there is no theoretical explanation for the peaks. Major experimental problems include background caused by the extremely large flux of electrons and photons from the target, target deterioration, the low duty cycle and intensity of the beam at GSI, and the need for high-resolution electron and positron detectors. Some of these issues are addressed by APEX, a proposed experiment with a new solenoid detector at the ATLAS facility of Argonne National Laboratory.[4] While the NSCL is an active member of this collaboration, we also intend to investigate the background problem with our own detector and with heavy-ion beams from the K500 or K1200 cyclotrons.

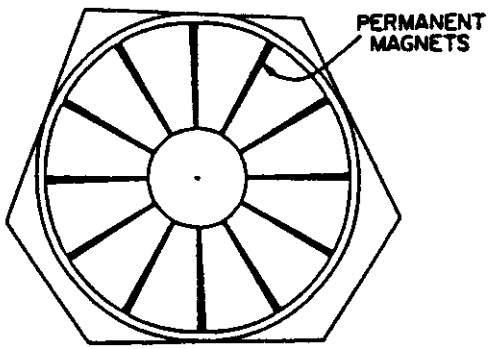

FIG. 1: Profile of a single lens as viewed from the target. The complete array would consist of 60 hexangonal modules of this shape and 12 regular pentagonals modules (not shown).

One of the designs considered for the APEX proposal[4] was a set of magnetic toroidal lenses located on a sphere around the target. Depending on the orientation of the field, each lens would selectivity transmit either positrons or electrons. The transmitted particles would be collected by a silicon detector on the axis of the lens. The direct path from target to detector is blocked by a plug of "Heavymet" (90% W, 10% Ni/Fe/Cu). Because the rate of low-energy electrons is very high, the number of scattered electrons reaching the Si detector is significant. Thus, additional identification of positrons is essential. This is achieved through the detection of their annihilation radiation in gamma detectors which surround the Si counter. This "positron lens" design offers the unique advantage of decoupling time-of-flight and angle of emission, compared to existing detectors at GSI and the proposed APEX design. Tests on an early prototype lens showed that when the lens was orientated to focus positrons, rejection of electrons was very effective.

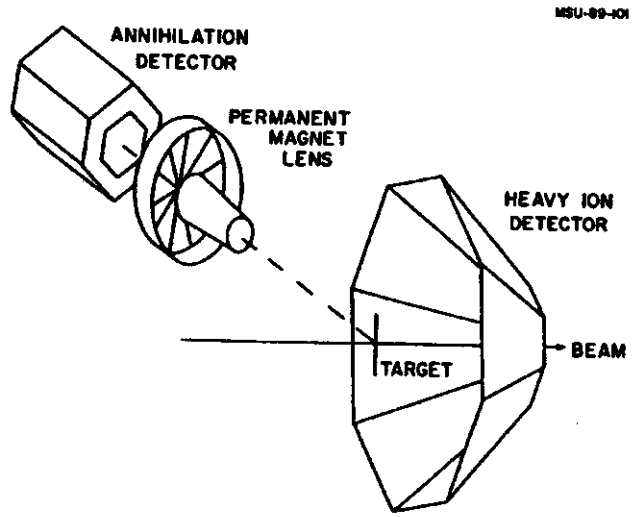

FIG. 2: Sketch of the arrangement of the lens and heavy-ion counters around the target.

We have built and are preparing to test a single toroidal lens which will be used to study backgrounds present in heavy-ion collisions (using beams from the K500 cyclotron) and positron-scattering from bound electrons. The magnetic field is provided by 12 thin, permanent magnets arranged like spokes in a wheel (see Fig. 1). The electron detector will be a 1700 mm^2 Si(Li) detector, cooled to give an expected energy resolution of about 20 keV. The annihilation detector will probably consist of an array of CsI or NaI bars in a barrel arrangment around the Si(Li) detector.

We also are designing a heavy-ion detector so the lens can be used to study positrons emitted in coincidence with heavy-ion scattering. The proposed detector is an umbrella arrangement of position-sensitive PPAC detectors (see sketch in Fig. 2). A meander-type delay line would be used to measure the scattering angle with respect to the beam axis.

References

1. T.E. Cowan, Ph.D. thesis, Yale University, 1988.

2. P. Kienle, Annu. Rev. Nucl. Part. Sci., 36, 605 (1986).

3. A. Schaefer, J. Phys. G 15, 373 (1989).

4. Proposal for an ATLAS Positron Experiment, submitted to the US DOE February 1989, APEX Collaboration (Argonne National Laboratory, Florida State, Michigan State, Princeton, and Yale Universities).

^{7}Be Production for Wear Research

M.L. Mallory, R.M. Ronningen, Wm.C. McHarris, B. Sherrill, Y.X. Dardenne, and H. Schock[a]

Introduction

In last year's Annual Report the initial experiments at making ^{7}Be radioactivity isotopes by particle fragmentation and implanting this isotope into wear test samples were described. During the current research period we extended our measurements and summarize them here. Also, a funding proposal for the establishment of an engineering wear research center with the Mechanical Engineering Department was completed.

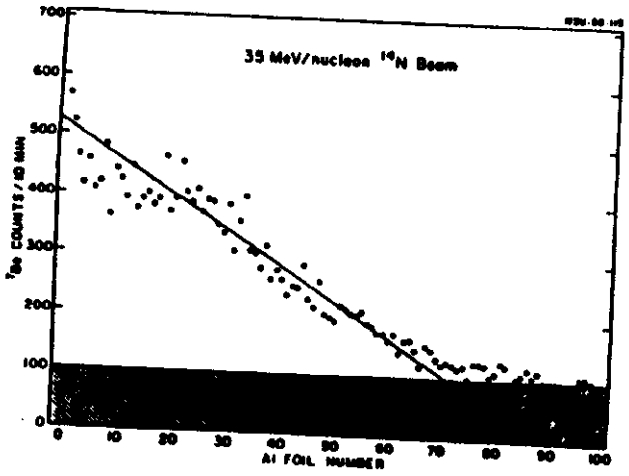

FIG. 1: The dose-depth relationship is shown for ^{7}Be ions implanted in stacked 0.0025-cm-thick Al foils for a primary ^{14}N beam energy of 35 MeV/A.

^{7}Be Dose-Depth Measurements

In order to quantitatively measure the wear rate of a test sample, the ^{7}Be dose-depth must be known. Figures 1, 2 and 3 show experimental data obtained for ^{7}Be distributions in Al-foil stacks for three nitrogen bombardment energies, 35, 22, and 17 MeV/A. Each Al foil is .001" thick. The nitrogen beam energies were reduced to 23, 14, and 11 MeV/A, respectively, by the carbon target before entering the Al-foil stack. The distributions can be analytically derived from fragment spectra results obtained from nitrogen beam studies on thin carbon targets.[1] An analytical spectrum shape that has a Gaussian distribution for the high-momentum fragments (and an exponential

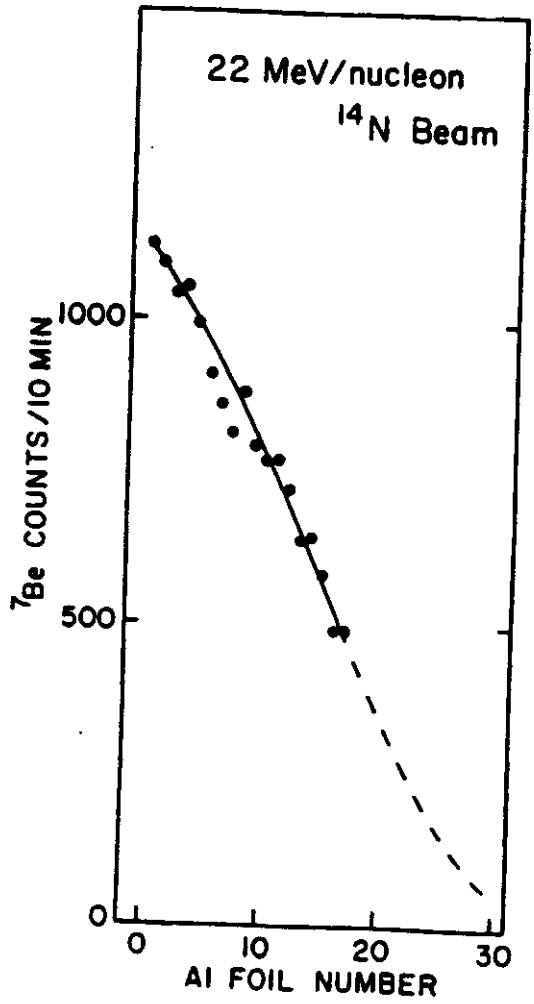

FIG. 2: The same as Fig. 1 except here the beam energy is 22 MeV/A.

shape for the lower energy fragments) fits those data.[1] Using only the Gaussian distribution, appropriate range curves, and an assumption on the energy variation of fragment cross section, Fig. 4 was calculated. This result can be compared with the Al-foil stack data and is promising. Thus, we are beginning to develop an analytical method for predicting the ^{7}Be dose-depth distribution into any test material.

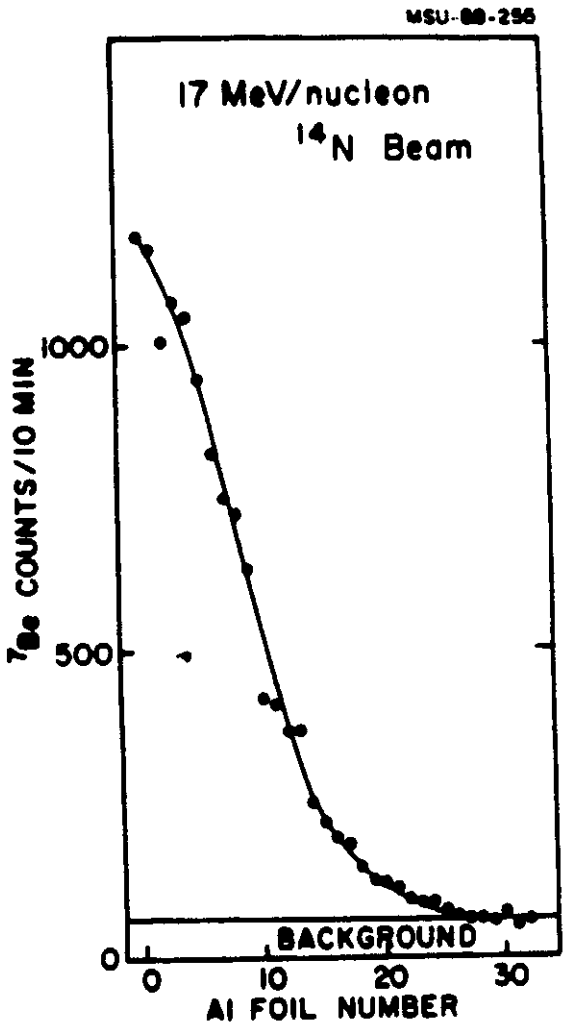

FIG. 3: The same as Fig. 1 except here the beam energy is 17 MeV/A.

^{7}Be Sample Implantation

A Si_3N_4 ceramic disk was substituted for the Al-foil stack and implanted with ^{7}Be. A carbon target in front of the disk was bombarded for 24 hours with a 17 MeV/A nitrogen beam, yielding an implanted dose of 3.7×10^{11} ^{7}Be ions. This disk is now being used in a wear study program, the first step of which is to determine the dose-depth relationship directly by controlled wear rates.

In our experiments the beam current from the K500 cyclotron was limited by the power dissipated in the electrostatic deflectors by internal beam losses. The deflectors are not cooled, and it is expected that cooling would allow beam intensities greater than 1×10^{13} pps.

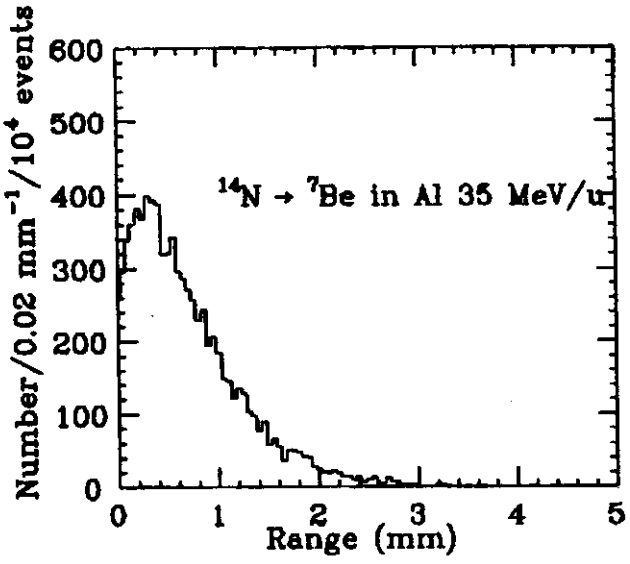

FIG. 4: A theoretical simulation of the dose-depth distribution of ^{7}Be in Al at 35 MeV/A is shown. Additional nuclear research data will make it possible to compute the dose-depth of ^{7}Be in any material.

The cyclotron beam current upper limit is unknown, but beam power limits, ion source output and space charge limitations are all starting to be areas of concern, are of interest to accelerator design, and will be addressed in future experiments. Experiments at increasing the nitrogen beam limits from 10^{11} pps to 10^{13} pps are underway on the K500 cyclotron.

Conclusion

In summary, ^{7}Be implantation into light materials has been demonstrated using the K500 cyclotron, and experimental and model studies of the dose-depth relationships are in progress. Further pilot studies with the present K500 beam intensity are planned. Additional cyclotron development and material property studies are needed before this technique will be easily and economically available. These will aid in the design studies of a dedicated ^{7}Be cyclotron. Such a dedicated machine appears to be able to make economical ^{7}Be implanted wear samples.

References

a. MSU Mechanical Engineering Department

1. Z. Seres *et al., NSCL Annual Report* (1987), p. 15.

Beam Diagnostic Developments at NSCL

F. Marti, R.A. Blue, J. Johnson, J. Kuchar, J.A. Nolen, P. Rutt, B. Sherrill, and J. Yurkon

Introduction

The National Superconducting Cyclotron Laboratory (NSCL) facility will consist of two superconducting cyclotrons, K500 and K1200, delivering beam to several experimental rooms. Since we are just beginning operation of the facility, cost and flexibility were considered in the design of the diagnostics systems at this stage. Space in the beamline is very limited and quickly interchangeable devices are needed, since we plan to try different devices and do not want to change the diagnostic boxes where these devices mount. This requirement guided us to develop a multipurpose beam diagnostic chamber that would easily accept a variety of diagnostic equipment.

Another requirement is to minimize the radiation produced during beam tuning. We would like to tune with total beam currents of 1 electrical nA or less. This goal is made possible by very sensitive phosphors, which are applied to scintillator plates to brighten the intensity of the beam image. We plan to tune the beamline with low intensities obtained by inserting attenuators[1] in the low-energy injection line, then remove the attenuators and send the more intense beam to the experiment. Our laboratory has been using scintillators for many years, viewing them with TV cameras for qualitative information. Low-cost framegrabbers that digitize TV signals allow accurate quantitative measurements with the scintillators. Several other laboratories are undertaking similar efforts with different beams and goals.[2-4]

Beam Diagnostics Chamber

The basic beam diagnostic chamber that we have adopted is shown in Fig. 1. It consists of a 25-cm-diameter stainless tube with two large Conflat flanges closing the top and bottom openings. The beam enters and leaves the chamber through two 10-cm pipes on each side of the chamber. (See Fig. 2.) A 15-cm viewing port is provided and is perpendicular to the beam trajectory. The top flange is used in some cases to mount a turbo molecular pump. Six half-nipples with standard 2.75 inches Conflat flanges are welded on the bottom flange. Four of these flanges are used to mount the actuators that move devices into the beam path, and the other two provide for either extra electrical feedthroughs, or vacuum gauges.

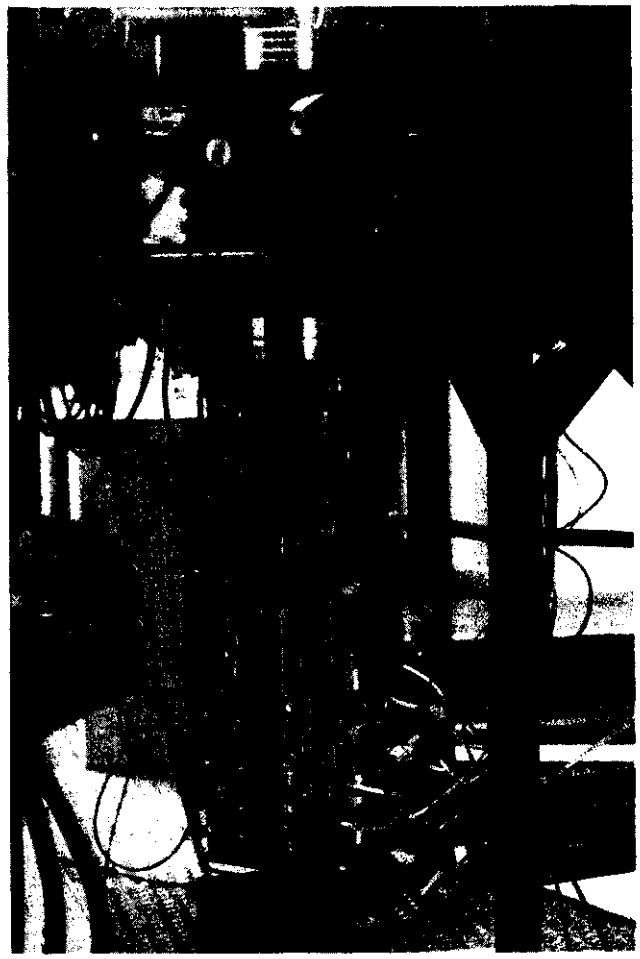

FIG. 1: Photograph of the standard beam diagnostic chamber, equipped with four actuators. Each actuator has three air cylinders that move the shaft to six different positions. A side port with a large window allows the TV cameras to look at the scintillators.

The basic actuator design consists of three air cylinders, with lengths 1, 2 and 3 (or 4) inches. By expanding and contracting, the appropriate cylinders the actuator can change its position by 1-inch increments, allowing up to six

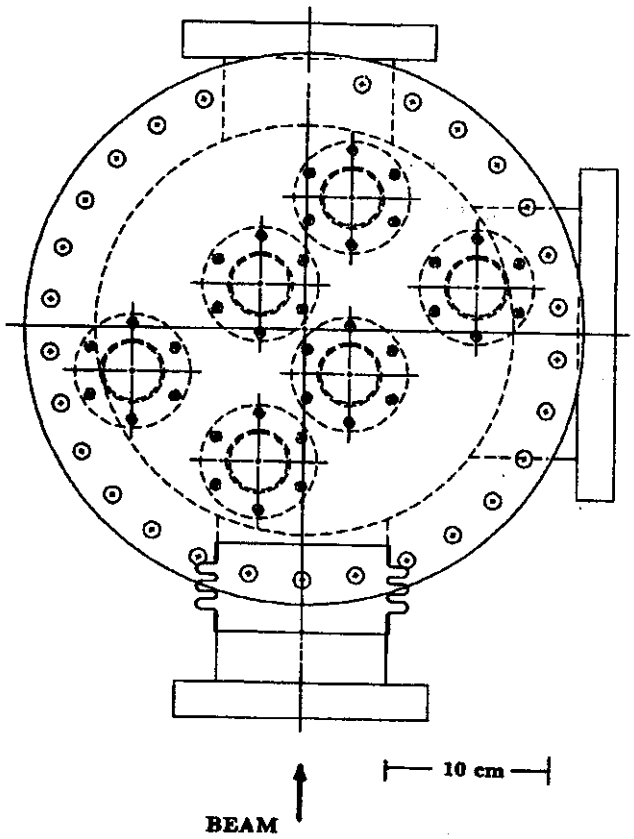

FIG. 2: Top view of the standard diagnostics chamber showing the four flanges for the actuators (on the beam path) and two for the feedthroughs or vacuum connections.

devices (different scintillators, for example) mounted on a single shaft. The hollow shaft allows water cooling and electrical connections that move with the actuator. In the case of a wire scanner for example, only one cylinder (the 4-inch) needs to be moved to scan the whole beam cross section. All actuators are bellows-sealed. A smaller version of this standard chamber is used in places where only one actuator is required.

Beamline Viewers

Phosphors

One aspect still under investigation is the suitable scintillation material and the method for depositing it on a metal plate which can be inserted in the beam. For K500 cyclotron beams we almost exclusively use Al_2O_3 plates, which have a very long lifetime but relatively low light output. Chromium doping improves the light output significantly, and experiments elsewhere[6] have proven it to be rugged and radiation-resistant. Most of the preliminary K1200 beam diagnostics has been done with a ZnS phosphor, which is widely available and inexpensive. Its light output is much brighter than pure Al_2O_3, and has allowed us to see beams as weak as 10 pA. We compared the light output of other types of phosphors, such as the rare earth phosphor gadolinium oxysulfide, but ZnS is as bright or brighter.

We also investigated various methods of depositing the phosphors, including spraying, electrocathaphoresis,[7,8] and sedimentation. Sedimentation has proven to give the best results. In this method, the phosphor powder is put into suspension above the plate to be coated. After several hours, the phosphor settles, to form a very uniform deposit on the plate. Varying the amount of material in suspension controls the thickness of the phosphor deposit. We found that organic and inorganic materials used as binders to hold the phosphor on the plate are damaged very quickly when exposed to the beam and so limit the useful lifetime of the plates. Hence, at present, no binders are used. We intend to continue studying new phosphors and different methods of binding. Issues which need to be studied are phosphor lifetime, grain size, decay-time, light-output, and linearity of response.

Experience has shown[5] that phosphors have a linear response for light particles and time-averaged current densities of less than 10 $\mu A/cm^2$. At higher current densities the non-linearities depend on the details of the pulse structure. Some preliminary linearity studies have been made by Anderson[7] for electrons with the same speed as the H^- ions used in the Neutral Particle Beam Test Stand at ANL, showing that for current densities below 5 $\mu A/cm^2$ ZnS:Ag was very linear, and had a slight quadratic dependance above that current density. However, at present no data is available for heavy ions.

Frame Grabber

Scintillators offer an excellent 2-dimensional display of the beam current distribution. However, until recently, it was difficult to obtain quantitative information from them. They were used mainly to position and focus the beam at the target. Wire scanners and harps gave profile informa-

tion, although as projections in x and y. If a more detailed measurement was needed, tomographic reconstruction was used.[9]

The availability of moderate cost frame grabbers opens new possibilities in this field. Basically, these frame grabbers are add-on boards to computers that take the TV signal directly from the camera and digitize the intensity level. This digital signal can then be manipulated arithmetically and then converted back to three analog signals that are sent as the RGB inputs to a color monitor. It is possible with some boards to assign different colors to different intensity levels. In this way subtle differences in gray level become clearly distinguishable. This feature has proven to be very useful in our beam line tuning, simultaneously giving position, intensity, and 2D shape information.

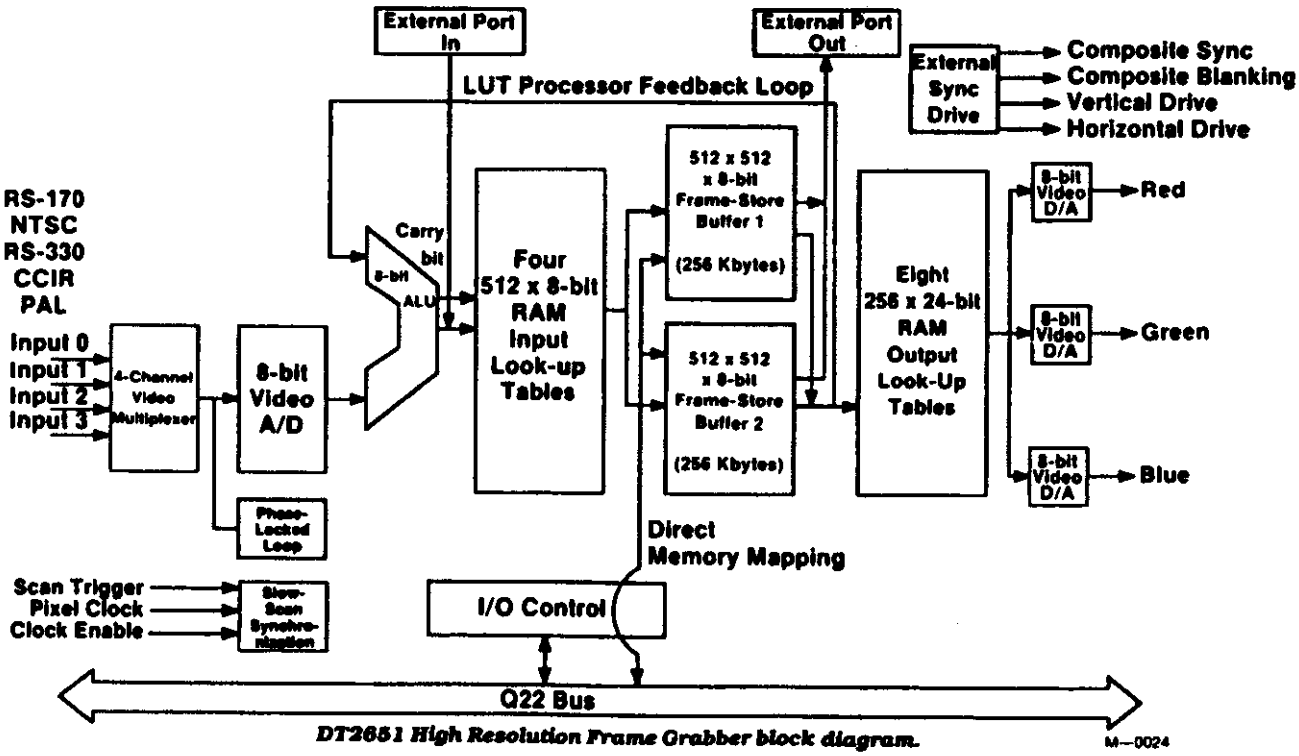

FIG. 3: Block diagram of DATA TRANSLATION DT2651 frame grabber. The basic features include: 4-channel multiplexer, 8-bit 10 MHz ADC, two 512 × 512 frame-store buffers and look-up tables. Pseudo-color representation of gray scales can be done in real time at 30 frames per second. The communication with the co-processor is done through the two additional ports shown on top of the diagram.

Frame grabber boards are now available for a large variety of computers, including microVAX, IBM-PC and clones, VME Bus, MacIntosh, etc. We selected a frame grabber board for a Q-bus microVAX because: a) we already had several microVAXes in the control system for the accelerators, and the database of accelerator parameters was then available to our software; b) we felt that using a PC-style computer would require many more file transfers to the microVAXes, where the final analysis would eventually be done and where our main disk storage was located; and c) we were more familiar with the microVAXes. These reasons probably would not apply to other installations. Similar boards for PCs are less expensive than the microVAX version.

We bought the high-resolution frame grabber DT2651 and the auxiliary frame processor DT2658 with the DT-IRIS software package from Data Translation.[10] The block diagram of the DT2651 is shown in Fig. 3 and a complete system

diagram in Fig. 4. There is a four-channel multiplexer on the board, but we have an additional multiplexer in front that allows us to have many more cameras connected to one single board.

The DT2651 operates in real time, digitizing, storing, processing and displaying 30 frames per second. Each image is a 512 × 512 pixel matrix. (In the 60 Hz version only 512 × 480 are usable). The ADC is an 8-bit flash converter, operating at approximately 10 MHz. There are two 256 Kbyte frame buffers. Either one can be displayed after processing through the look-up tables. It is possible to create overlays that are displayed on top of the incoming picture (this is done by write-protecting a bit plane); it is a useful feature that allows to have scales associated with each observing station. The DT2651 provides two asynchronous data ports which communicate at very high speed with the DT2658 co-processor, without overloading the Q-Bus. The co-processor is used for frame addition and subtraction, averaging, histogramming, zoom and pan, etc. We must note that these operations are not done in real time; it takes the DT2658 four frame-times to complete them.

We use a Cohu 4810 CCD camera,[11] which has an active area of 8.8 × 6.6 mm with a cell size of 11.5 μm(H) by 27.0 μm(V). This camera has very good sensitivity and it is possible to turn off the automatic gain control and to set the gamma to 1.

Beamline Tuning

Our basic use of the phosphor frame grabber combination is to display the beam spot in pseudo-color. This allows the operator to quickly see what is happening to the beam in two dimensions. After obtaining an image in gray scale, the operator decides what color table to use; we normally use 10 different colors. Then, from a histogram of the number of pixels-vs.-pixel intensity, the operator selects the minimum (*black*) and maximum (*white*) levels, and the color table translation is applied between these two levels. Every pixel with an intensity higher than *white* will be white and every pixel with intensity lower than *black* will be black. The intensities in between will be divided in 10 equally-spaced intensity levels, each shown as a different color. In this way, the shape as well as the current distribution can be observed by the operator. Absolute current readings can be obtained with a Faraday cup behind the scintillator, although once calibrated, the total light output could be used as an intensity measure.

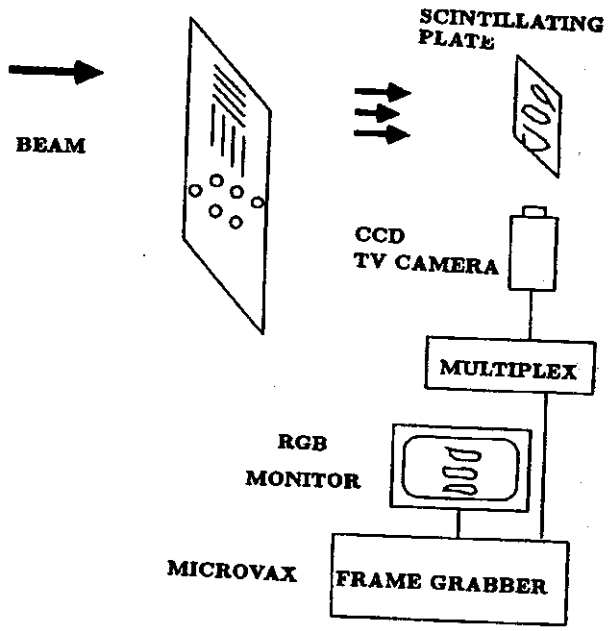

FIG. 4: Diagram showing the main components of the beam viewers and emittance measurement system. The beam impinges on the scintillating plate at 45° with the incoming beam. The beam spot is observed through a TV camera at a right angle with the beam path. A perforated plate partially stops the beam for the emittance measurement. The image produced by the TV camera is digitized and transformed to pseudo-colors by the frame grabber in the microVax, and displayed on the RGB monitor.

The frame grabber can simulate a wire scanner and display the beam profile in x and y projections if so desired. Each of the viewer stations may have an overlay stored with scales, target position or other information that the operator recalls if needed.

Emittance Measurements

One method of measuring beam emittances is the "pepperpot". In this method, a plate with a regular pattern of holes is placed in the beam to create many beamlets. The divergences are then measured for each beamlet. This technique is cumbersome because of the difficulties associated with reading a two-dimensional distribution of the current density downstream of the pepperpot. It takes so long to take measurements that this method is not widely used.

The "scintillating plate-plus-frame grabber" technique is a very good solution to the speed problem in the pepperpot method. In just a fraction of a second a complete digitized image is available for processing. Figure 4 shows the setup to measure the emittance of the extracted beams of the K1200 cyclotron. The distance between the perforated plate and the scintillating plate is 1 m. Three different patterns of perforated plates can be inserted into the beam. One of them is a pepperpot plate with 0.8-mm-diameter holes, separated by 2 mm between rows and columns in a staggered pattern. The other two plates are vertical and horizontal slits, with a slit width of 0.5 mm and a distance of 3 mm between centers. These slits simulate the scanning wire method, but since the slits are fixed, the resolution is poor.

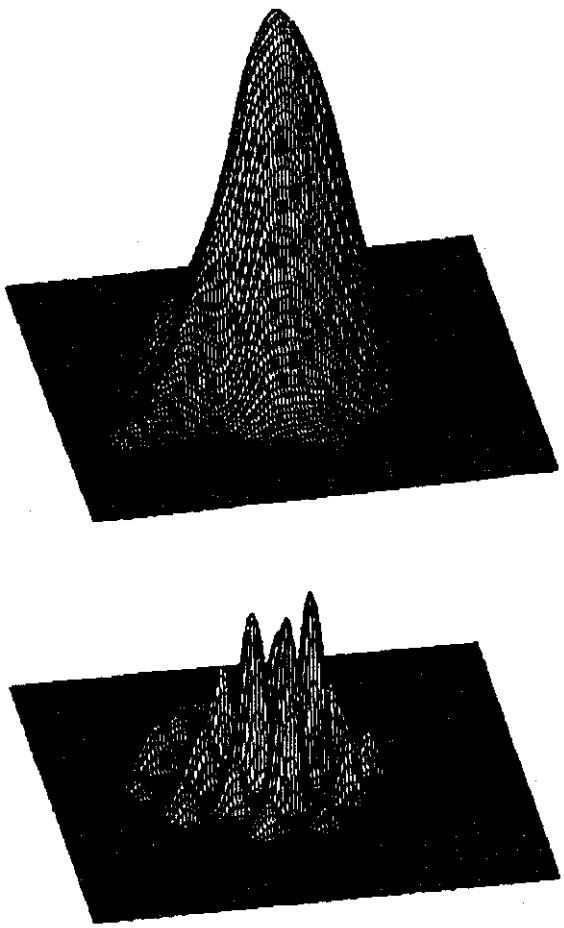

FIG. 5: 3D plot of "intensity vs. x-y" for the direct beam (top) and for the beam with the pepperpot plate inserted (bottom). The raw data is being displayed; no smoothing was performed. A total current of 0.5 enA of 75 MeV/u $^{40}Ar^{13+}$ was utilized.

Figure 5 shows a 3-dimensional plot of "intensity vs. x-y" for the direct beam (top) and for the beam with the pepperpot plate inserted (bottom). A beam current of 0.5 enA of 75 MeV/u $^{40}Ar^{13+}$ was observed. No smoothing of the data was done. The actual raw data is being plotted, as is the case in the other figures presented in this paper.

It is important to use the maximum dynamic range of the ADC in the frame-grabber. Since the intensity of the image changes significantly when the pepperpot plate is inserted, it would be useful to have a remote iris lens on the TV camera.

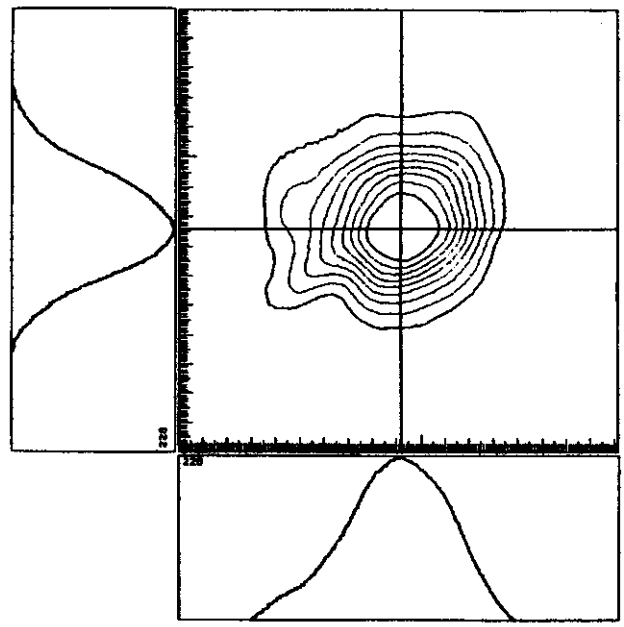

FIG. 6: The data shown in Fig. 5 (top) but shown as a contour plot. The two lines that cross at the center of the beam define the cross sections shown at the bottom and on the left. They are not projections as would be obtained by a wire scanner, but actual cross sections through the beam. The smallest tick mark is 0.1 mm. The total area plotted corresponds to approximately 18 × 15 mm.

The emittance-measuring setup is placed after quadrupoles which allow us to choose the beam size and divergence that works best with the hole size and the drift space between the perforated plate and the scintillator. This implies no overlap between the beamlets from adjacent holes. Once the phase space ellipse is calculated at the plate position, it is transported backwards to a point upstream of the quadrupoles using the known transfer matrices. A TRANSPORT calculation can then be started from that point to match the cyclotron extracted beam to the beam transport system. The

data from Fig. 5 is presented as contour plots in Figs. 6 and 7. We note that the profiles at the bottom and on the left in Fig. 6 correspond to cross sections through the beam as shown in the contour plot. They are not the profiles that we would obtain with wire scanners (i.e. total projections on the x and y axis).

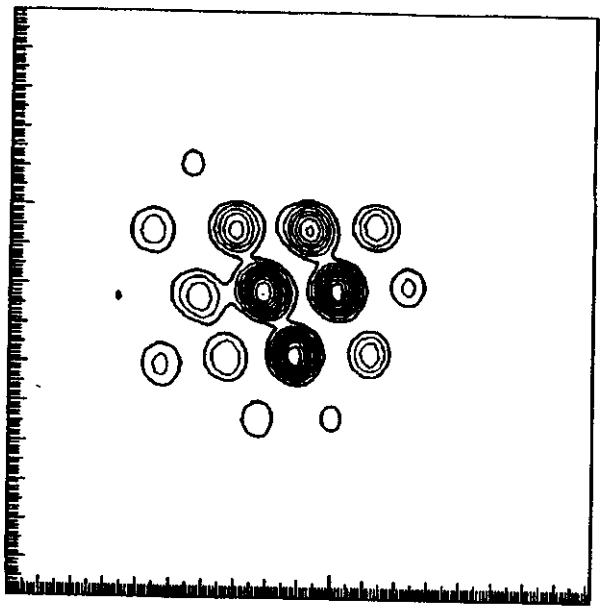

FIG. 7: The data shown in Fig. 5 (bottom) but shown as a contour plot. The scale is the same as in Fig. 6.

The smallest tic marks on the scales correspond to 0.1-mm intervals. The resolution in these pictures was approximately 15 pixels/mm. We can probably obtain twice this resolution by changing the optical arrangement and reducing the field of view. The area plotted corresponds to approximately 18 × 15 mm, corresponding to half the size in x and y of the total digitized frame.

Once the digitized image is available in the microVAX, we identify the individual peaks in the pepperpot configuration. From the peak analysis, the divergences in x and y are determined and assigned to the known x and y of that hole. Unless one of the holes is different, there is an unknown offset in (x,x') and (y,y'). This offset just gives a displacement of the phase space ellipses that is not significant. Ellipses are now fitted to the points and their area gives a measurement of the emittance.

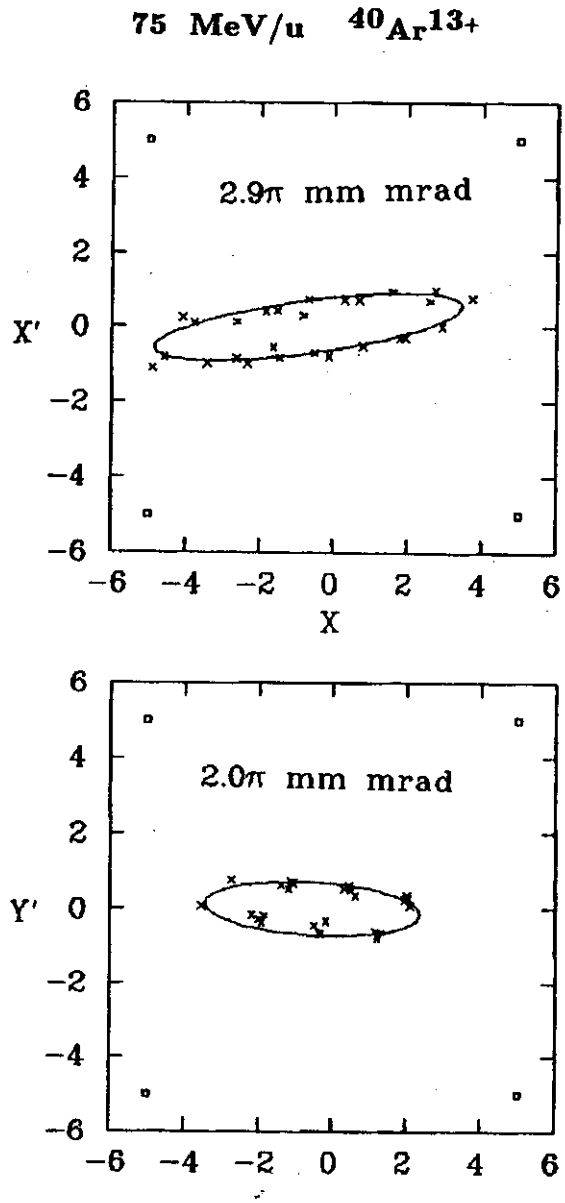

FIG. 8: Phase space ellipses determined from the data given in Figs. 5, 6 and 7.

An example of this calculation for the data of Figs. 5, 6 and 7 is given in Fig. 8. It is interesting to observe in the bottom half of the figure the grouping of points in the (y,y') space. For each y we had several holes illuminated, and each of them contributed a pair of points to the diagram. The fact that they are in compact groups implies little correlation between x and y. An alternative way to determine the beam σ matrix would be to determine the beam size at the

scintillator as a function of the strength of a quadrupole placed upstream in the beamline,[2] but no information on the correlations would be obtained.

References

1. R.F. Burton, D.J. Clark and C.M. Lyneis, "Beam Attenuator for the LBL 88- inch Cyclotron," Nucl. Instrum. Methods A270, 198 (1988).

2. M.C. Ross *et al.*, "Automated Emittance Measurements in the SLC," *Proceedings of the 1987 IEEE Particle Accelerator Conference* (1987), pp. 725-728.

3. A.A. Hassan, C.L. Fink and M.G. Rosing, "A Beam Characterization of H^- particles"; T.J. Yule *et al.*, "Beam Characterization with Video Imaging Systems at the ANL 50-MeV H^- Beamline," presented at the 1989 IEEE Particle Accelerator Conference, Chicago, Ill., March 1989.

4. D.P. Russell and K.T. McDonald, "A Beam-profile Monitor for the BNL Accelerator Test Facility (ATF)," presented at the 1989 Particle Accelerator Conference, Chicago, Ill., March 1989.

5. A. Martin, Adv. Electronics and Electron Phys., 67, 183 (1986).

6. S. Yencho and D.R. Walz, "A High-resolution Phosphor Screen Beam Profile Monitor," *Proceedings of the 1985 IEEE Particle Accelerator Conference,* (1985), pp. 2009-2011.

7. G. Anderson, LASL, personal communication.

8. C.P. Gutierrez, J.R. Mosley and T.C. Wallace, "Electrophoretic Deposition: a Versatile Coating Method," J. Electrochemical Soc. 109, 923 (1962);P.F. Grosso, R.E. Rutherford Jr. and D.E. Sargent, "Electrophoretic Deposition of Luminescent Materials," *ibid.*, 117, 1456 (1970).

9. G. Minerbo, "MENT: A Maximum Entropy Algorithm for Reconstructing a Source From Projection Data," Computer Graphics and Image Processing 10, 48 (1979).

10. Data Translation, Inc. 100 Locke Drive, Marlboro, MA 01752-1192, USA and Data Translation GmbH, Stuttgarter Strasse 66, 7120 Bietigheim-Bissingen, West Germany.

11. COHU Inc., 5755 Kearny Villa Road, P.O. Box 85623, San Diego, CA.

Test of an Avalanche Diode as a Detector for Measuring Beam Phase Width

R.M. Ronningen, J. Yurkon, and M.R. Maier

A detector which can measure the cyclotron beam phase or phase width is a useful diagnostic device. Considering its importance we have experimented with different types of detectors in an effort to maximize performance.

In previous annual reports we described tests of silicon photodiodes used as detectors. Silicon photodiodes have the advantage of compact size. In addition, they have low noise (small capacitance), are relatively impervious to strong magnetic fields, and are capable of fast risetimes (less than a nanosecond).

One of the first types of silicon photodiodes used was a pin diode (Hamamatsu series S1722). We coupled it to an integral preamplifier (NEC μPC1651G) to measure the phase width of the beam internal and external to the K500 cyclotron[1]. The preamplifier's output went into another preamplifier designed by H.J. Beeskow of GSI-Darmstadt. The pin diode detector worked well enough for initial tests[1] but was susceptible to heat and radiation damage. Furthermore, its inefficiency made it hard to bench-test.

Recently, we replaced the pin diode with an avalanche photodiode (Hamamatsu S2382), which we coupled to a broadband monolithic amplifier (Mini-Circuits MAR series). The efficiency and gain of this system are superior to the pin diode's. Bench testing can be done with a strong gamma or electron source, and no additional preamplifier is needed.

We measured the avalanche photo diode's time response using a conventional fast-timing setup with a time-to-amplitude converter. The avalanche diode provided the start signal, and the stop signal was provided by a 1.91 cm cylindrical BaF scintillator detector. The full-width-at-half maximum of the time distribution using a ^{60}Co source was about 550 psec.

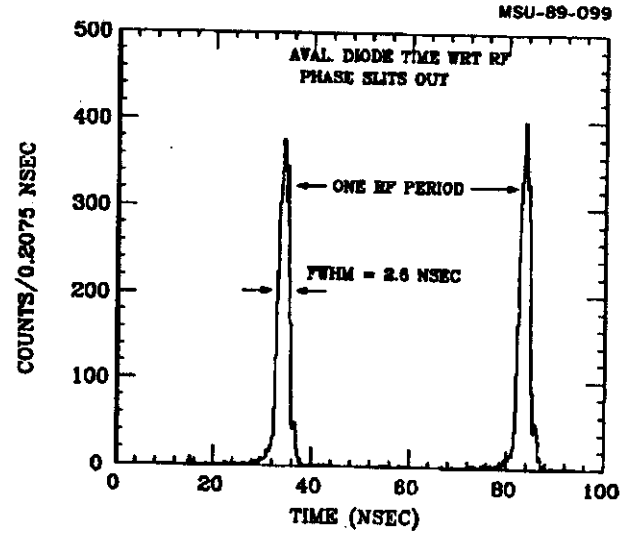

FIG. 1: Time spectrum of radiation from a K500 external beam with respect to the cyclotron RF. A TAC was used, with the avalanche diode detector providing the start signal and the cyclotron RF providing the stop signal. In this case phase slits internal to the cyclotron were not used.

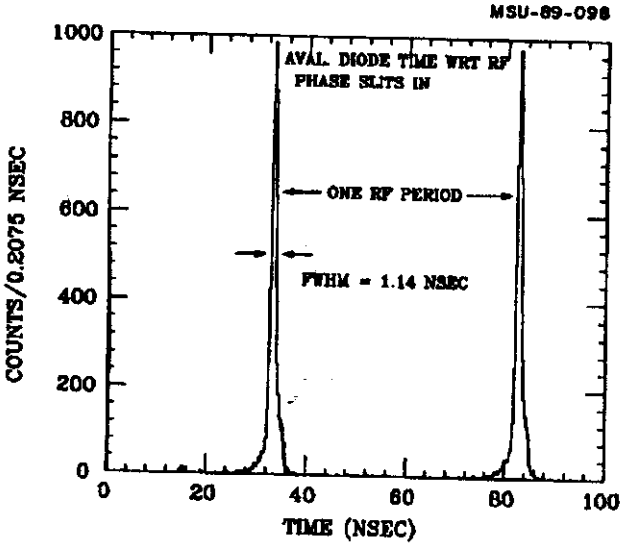

FIG. 2: The same as Fig. 1, except here the internal phase slits were used.

We then tested the avalanche diode detector with an external beam from the K500 cyclotron. Figures 1 and 2 show the time distribution of detected radiation with respect to cyclotron RF, with and without phase slits internal to the cyclotron. We plan to measure the beam inside the cyclotron soon.

References

1. B. Milton, Ph.D. thesis, Michigan State University, 1986, unpublished.

Phase II Control System

L. Foth

Introduction

Much of the equipment interface and operator interface sections of the Phase II computer control system for the NSCL is in place. Most major design decisions have been made and implemented. Some design issues regarding the Main Control Console software are still to be resolved, as detailed in *"Main Console and Software", Priller.* This paper will briefly discuss the architecture and status of the overall system, then concentrate on the equipment interface level.

Overall Phase II System Architecture

In the NSCL Phase II control system, both the processing power and the database are distributed among 15 to 20 VME stations, many of which are placed next to equipment in the field. Each VME station contains a Motorola 68010 microprocessor and a database of information for the equipment it interfaces to. The VME stations communicate with each other via ARCNET, a 2.5 MHz token bus, peer network. ARCNET links the VME stations with four user consoles, also known as "main consoles". Each main console is a DEC VAXstation II/GPX workstation, with knobs, meters, etc.

Figure 1 shows the overall control system architecture, without specifying the number of VME or VAX GPX nodes. The computers and networks shown above the "Control Ethernet" are not part of the control system and are outside the scope of this paper.

The four main consoles are clustered together with a MicroVAX II on the Control Ethernet. In Figure 1, a VAXstation console is shown with its I/O devices and Qbus ARCNET interface. The console's meters, knobs and switches interface to the GPX via a VME-to-Qbus card set, which maps a crate of VME cards into the GPX address space. This enables us to avoid buying expensive Qbus cards, for which there are few slots anyway.

The development MicroVAX II is used for: console code development that doesn't require the windowing environment; 68010 code development; and as an interface to a couple of CAMAC systems.

Also on the Control Ethernet is a terminal server which provides access to a plotter and printer, and which talks to a motor controller for the K1200 A2 probe.

VME equipment can be used for three different functions in the NSCL control system:

-- an I/O interface between a VAXstation console and its knobs, meters and switches;
-- a simple, yet functional user station (see above ARCNET in Figure 1); and
-- interface to the field equipment (below ARCNET in Figure 1).

The two latter types are VME "stations" and run the same software. The only difference between them is that the VME stations used purely as user stations are not directly coupled to any cyclotron devices and therefore do not contain their own database of control channels.

There is a database on the VAXcluster to provide device data needed by the VAX programs, but that the VME stations don't need. For example, name-to-channel number translations, knob speed scaling factors, etc. Similarly, information contained in the VME databases (hardware calibrations, engineering units, control-type information) is not kept in the VAXcluster database. Whenever this information is needed by a VAX program, the program must request it. This guarantees that changes made in a VME/68010 database will be seen the next time an operator controls a device using a VAX program.

Phase II Central Control and Information Flow

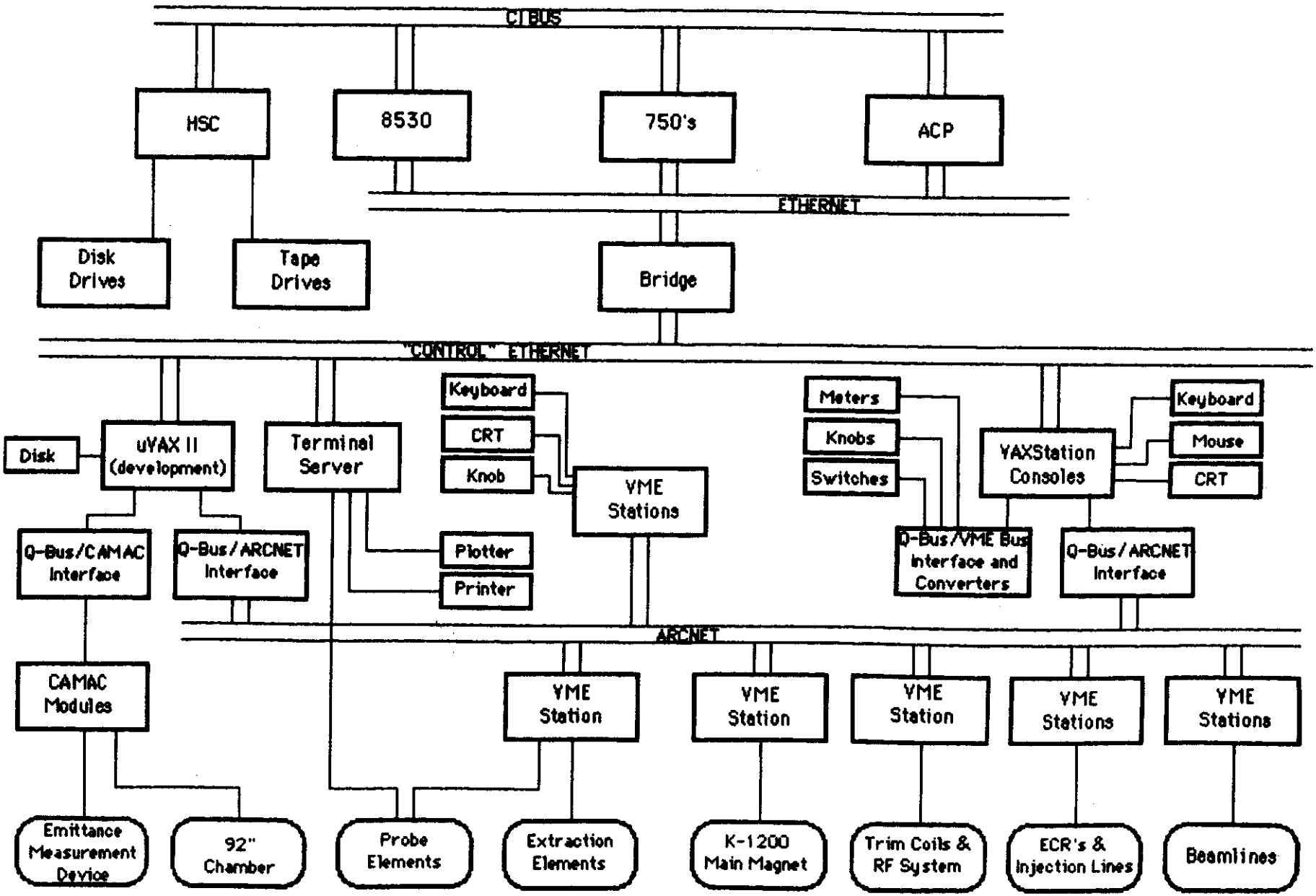

Figure 1

Phase II Control System

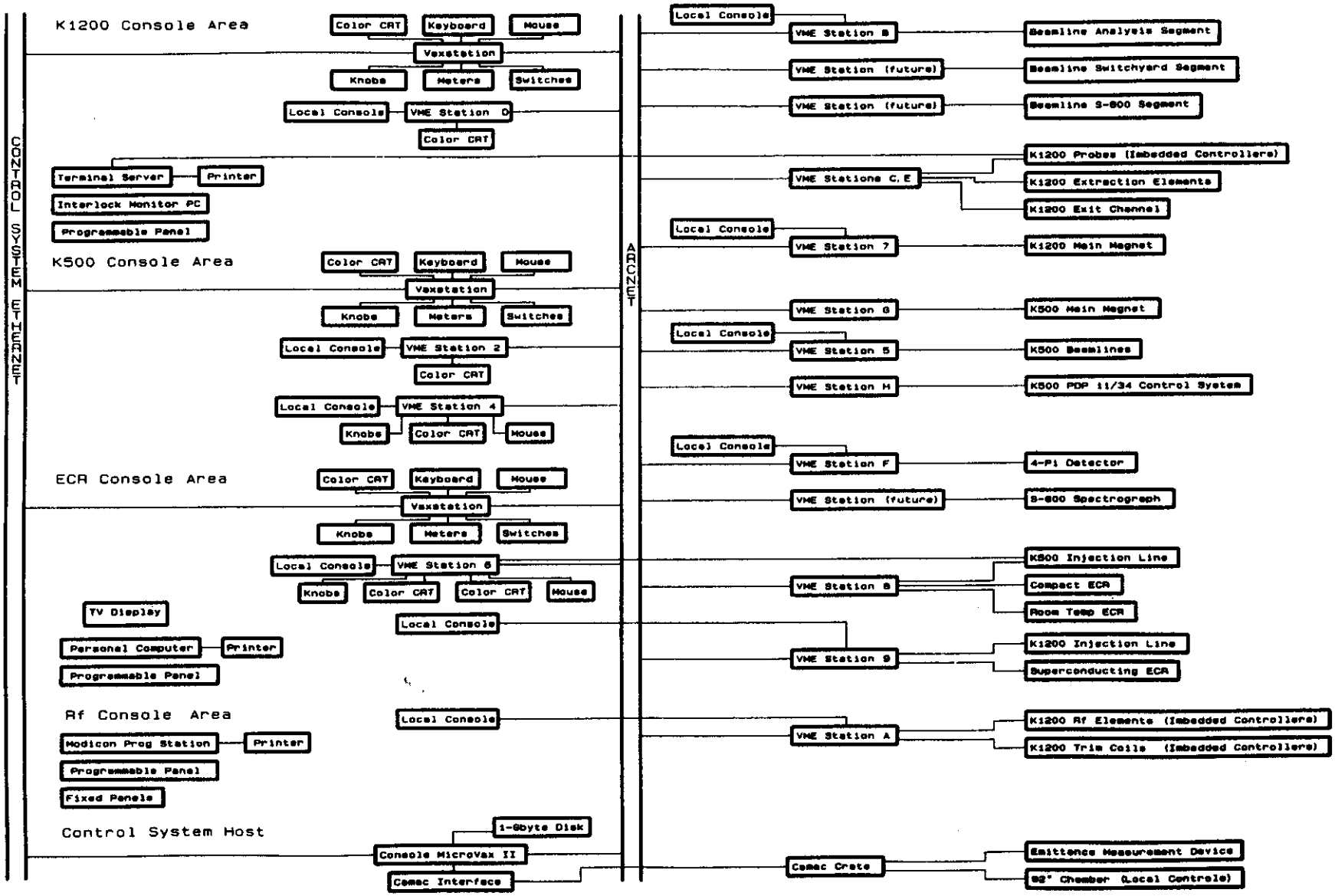

Figure 2

Control System Status

Everything shown below the Control Ethernet on Figure 1 is installed and working. We have four VAXstation consoles, four VME stations used as user stations, 11 VME/68010 equipment-interface stations, and two development VME stations. Figure 2 shows all but the development stations.

We are adding new VME stations as beamlines and experimental vaults are built. Concurrently, we plan to upgrade the VAX software so that:

-- multiple VAX programs may use ARCNET simultaneously;

-- CAMAC and Modicon devices are integrated; and

-- "smarter" pseudo devices are available (see *"Main Console and Software", Priller*).

Interface to Field Equipment

VME/68010 Stations

The VME/68010 stations which interface directly to the cyclotron and beamline devices are the heart of the control system. Each station can run stand-alone (for initial set-up) or networked via ARCNET. VME ARCNET nodes can be added to or removed from the network without affecting the operation of the other VME nodes. (The VAXes must be told of new or disappearing VME nodes due to their software configuration.)

The "core" of a VME/68010 station is four circuit cards: CPU, memory, ARCNET, and crate utility function card. The CPU card is a Motorola 110 with 68010 processor -- it's very simple, and a compatible card is now available from TL Industries for $650. The memory card is a Micro-Memories 6600-CC with 256K bytes of CMOS RAM and two NiCad batteries; it houses the device database. The ARCNET and crate utility cards were designed at Fermi National Accelerator Laboratory, where this station originated. One of the purposes of the crate utility card is to talk to a rack-mounted "local console" consisting of a keyboard, 5" CRT, shaft encoder knob and several buttons.

VME Input/Output Signals

All of the VME station I/O is memory-mapped. Our system contains a mix of direct-connect analog I/O and low-speed serial communications. Some of our early stations make use of Motorola I/O channel boards, since only that was available when the first stations were installed. Later on, as VME I/O boards became plentiful, we selected some standard analog-to-digital (-10V to +10V), digital-to-analog (-10V to +10V) and digital I/O (TTL) boards as the basic building blocks of the stations. Where isolation or signal-level translation is needed, we have used the "3B series" of off-board signal-conditioning modules made by Analog Devices.

Short, twisted-pair, shielded ribbon cables carry the analog signals from the VME stations to distribution panels we call "breakout boxes". Test points on Jones strips in the breakout boxes make it easy to determine if problems are in the VME hardware and software or in the wiring to the devices. This ease of troubleshooting makes it possible for many wiring problems and device malfunctions to be diagnosed and fixed without involving control systems programming staff.

As mentioned above, we use a good deal of serial communications to talk to devices. This is done where the environment is very noisy, where devices are sparsely distributed geographically, or where some local intelligence right near the device is desired.

VME Serial Input/Output

We currently support two different 9600-baud, character-oriented protocols. One protocol is the Opto-22 Optomux protocol, which interfaces to the trim coil power supplies. The other protocol, developed at NSCL, talks to hardware with embedded Motorola 68701 or 68008 microprocessors. The VME stations using serial I/O contain an Ironics 1624A 8-port serial I/O (SIO) interface card to handle the RS-422/485 communications.

The SIO card runs a multiple-protocol application developed on top of the pSOS kernel. This multiple-protocol application makes it possible to configure which lines run which protocols "on the fly". Code for each of the supported

protocols resides in EPROM on the SIO card. Configuration tables specifying what protocol runs on which line, and what types of devices are on each line, are loaded into the VME station's battery-backed memory. When the SIO board is reset, it copies these configuration tables to its own memory, initializes each port for the correct protocol, and manages all of the communications work, passing data back and forth to the VME station processor via the SIO board's dual-ported static ram. To add devices or change protocols, one merely re-loads new configuration tables and presses the reset button on the SIO card.

Because we use low-speed, character-oriented protocols, it is easy to use a protocol analyzer to test and troubleshoot the communications software and hardware. This was extremely valuable in pinpointing problems during initial development of this SIO system, and continues to be helpful when setting up new lines and new devices.

VME Station Software

Each VME/68010 station acquires data from the field devices and monitors them every 1/15 second. On each cycle, the analog and binary data is read into the VME's database and monitored for out-of-tolerance values. Any new alarm messages resulting from the scan are reported to the main console. If any other VME stations or main consoles request data, the requested readings are prepared and sent out via ARCNET. In addition, the VME/68010 station responds to setting requests and performs closed-loop control. Once all these functions have been completed, an application program executes to service the local console and update the video display.

The VME/68010 database contains device names, analog readings, settings and calibration constants, and digital control and reading characteristics. All of this information is organized in tables accessed through a standard mechanism. Because of the table-driven nature of the software, device calibrations can be changed and new devices of known types added "on the fly". Readings and settings are handled by device drivers and each device has a code informing the software which drivers to use. Thus, adding new types of devices is extremely easy for the software developer.

Each VME station runs identical system software, with the exception of some of the device drivers. This exception is due to the fact we have been installing stations over a number of years and adding new device drivers as we go. Eventually all stations may include all of the new drivers, to make station administration and documentation easier, but this is not mandatory.

Conclusion

The VME-based device interface stations have proven highly reliable, flexible and expandable. We have had very few failures of VME boards. Due to the battery-backed memory, the stations come back on-line immediately after power failures without human intervention. Twice when old 8080-based stations failed, we were able to move the controls over onto VME stations quickly, even though no plans had been made to do these takeovers. All in all, these stations are well suited to our control interfacing needs.

Main Console and Software

John Priller

Hardware Foundation

The K500/K1200 control system polls distributed VME stations (see *Phase II Control System, Foth*) to gather readings from the various meters and other devices in the ECRs, cyclotrons, beam paths, and experimental apparatus. Data from these devices is brought via ARCNET into DEC VAXstation II/GPX workstations, where it can be manipulated by control system programs, and where settings and other commands may be sent back to the individual devices.

Attached to each VAXstation via a VME-to-QBUS adapter is a control panel of knobs, toggles and buttons with which the operator adjusts device settings, and a bank of meters where readings can be viewed. Device drivers and interface software, written at NSCL, allow application programs to read and write to the control panel. The connections between the control panel and cyclotron devices are handled entirely in software, making them versatile and easily changeable. Graphics software on the VAXstations (some built-in and some written at NSCL) allows readings to be displayed on the video screen in text, graphics, or a combination of both. Each VAXstation also has its own keyboard and mouse.

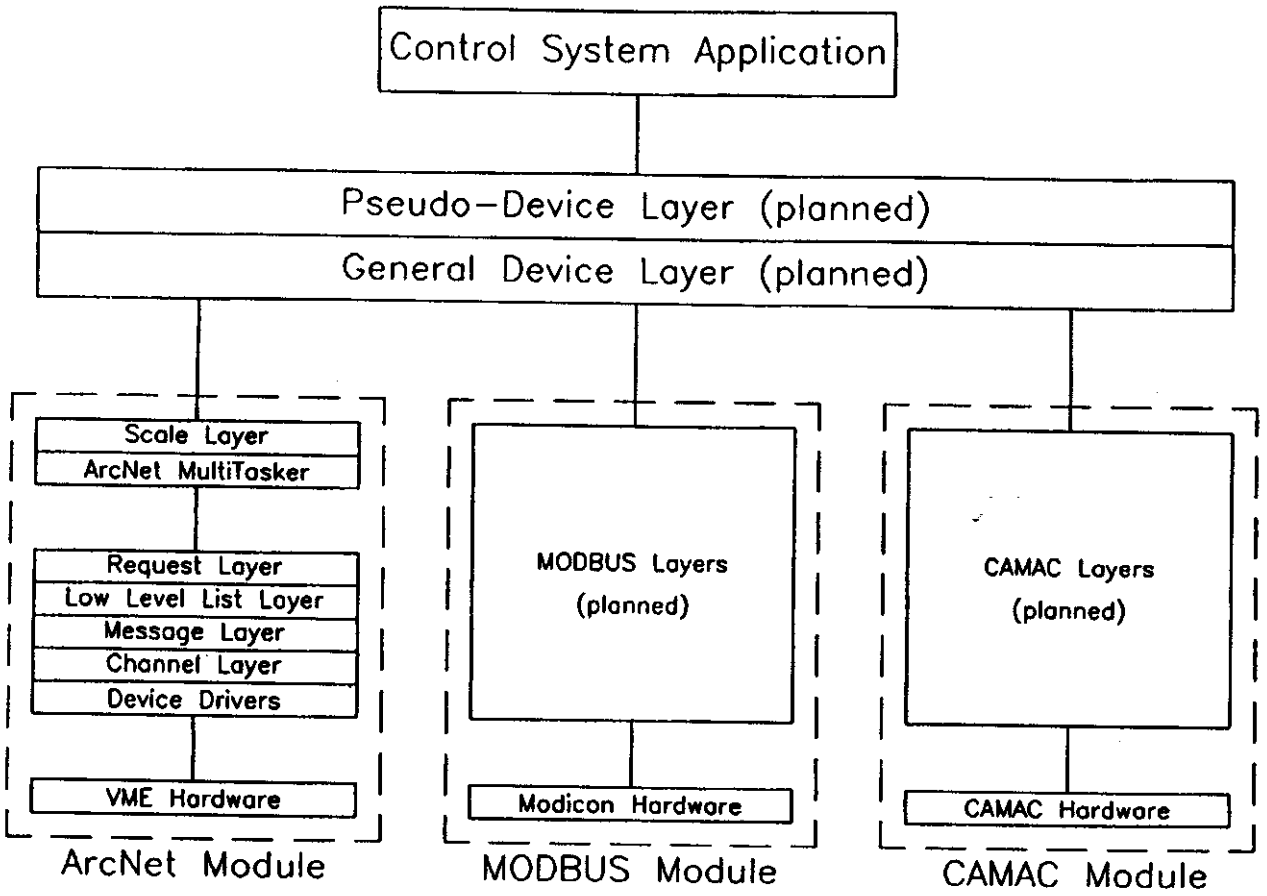

Figure 1: Control System Communications Diagram

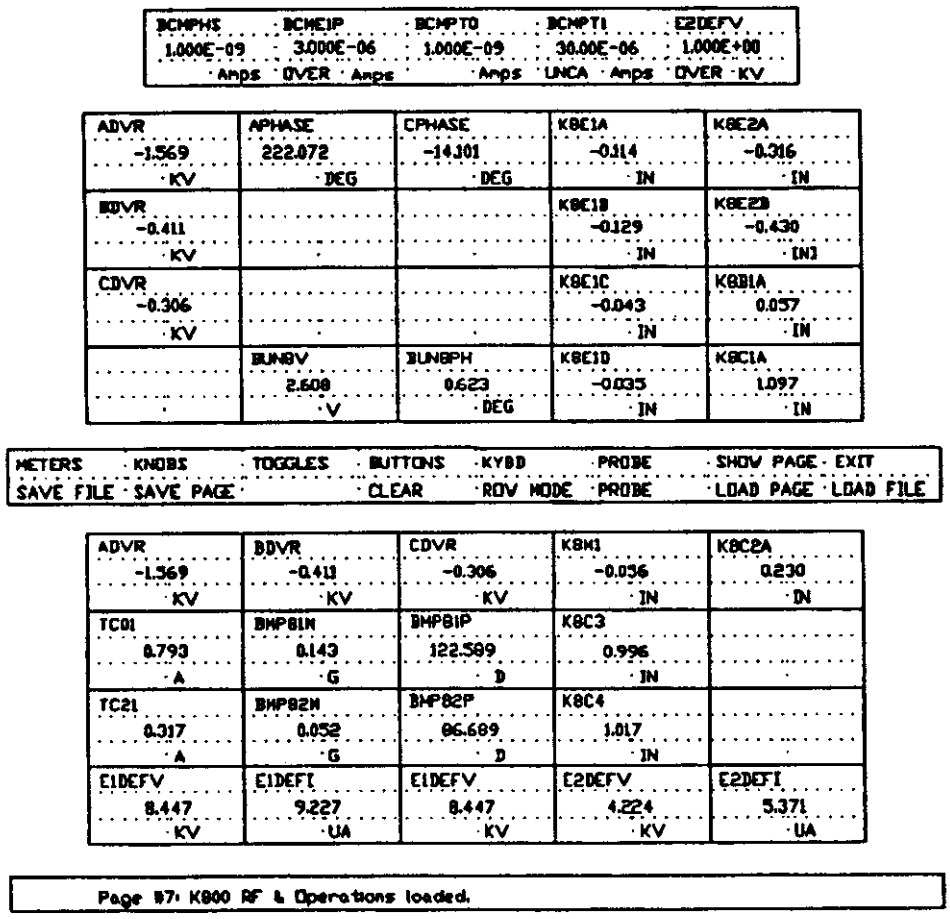

FIG. 2: Sample of 40-parameter page used on a VAXstation.

Software Foundation

Control system software is based upon a hierarchy in which each VAXstation communicates with control system devices through its ARCNET communications card. These software layers (see Fig. 1) collect the device data from the VME stations, scale it, and make it available to the applications programs in the VAXstations. They handle reading and setting requests across multiple nodes, present a small set of transparent device types to the program, and take care of almost all of the communications "housekeeping".

Most of these layers are written in VAX Pascal, with some of the lower layers relying on VAX "C" and VAX Macro assembler. VAX Pascal provides the interface between the uppermost layers and the application program, making it relatively easy for non-programmers to create their own individual control system applications (which is strongly encouraged).

Current Applications Software

The primary control system program is the K1200 Interim Maintenance Control Program, more simply known as "KIM". It can control both the K500 and K1200 cyclotrons, as well as the ECRs, experimental devices, and other apparatus. KIM's primary task is to display a grid of 40 display-boxes on the VAXstation's video screen (see Fig. 2), each one of which may have a control system device assigned to it, and to allow the operator to assign knobs and toggles from the control panel to the individual boxes/devices. KIM also has five additional boxes at the top of the screen which are automatically tied to the five meters in the control panel. Another five boxes at the bottom of the screen are reserved for Modicon control (which has yet

to be implemented). A central grid of control boxes allows the user to quickly and easily select commands, functions and menus via the mouse.

Another control program in place at NSCL is KIMLOG, a companion program to KIM which saves and restores device settings on a system or subsystem-wide basis. In practice, the operator tunes the ECR, cyclotron, etc., to the beam and energy desired, and then saves all of the appropriate device settings to a disk file. Later, KIMLOG may be run again to restore all devices to the previously saved settings, in effect restoring the conditions present when the experiment was last run. The disk files containing these settings may be stored in an individual user's directory, or in a common directory so that many users may have access to them. In time, a library of commonly used beams can be constructed, which should substantially reduce the time necessary to tune from one beam to another.

The final control system program installed at NSCL is FMONITOR, a utility for graphing up to three device readings, versus time or versus another device. When graphing *devices-versus-time,* the X-axis scale is adjustable from 2 minutes to 5 hours. If graphing *devices-versus-device,* the device on the X-axis may either be ramped between two limits or allowed to move freely. A printout of the generated graphs can be created on an HP ThinkJet color printer, or on whatever hard copy device is attached to the VAXstation (it supports several HP and DEC printers). FMONITOR is unique in the fact that it was never a planned application, but instead grew out of interest in a test program written to debug a new breed of beam current monitors. Due to multiple suggestions from many users, it was upgraded to a full-scale application and is still in development.

Future Software Plans

A number of software enhancements for the control system at NSCL are currently underway. They are described briefly below.

ARCNET MultiTasker

A limiting factor in the current control system software is that only a single VAXstation process may use the ARCNET card at a time. Since the VAXstation itself makes it easy to run programs in separate windows on the screen, it seems likely that someone will need to simultaneously run two or more control system processes, all of which will need to access the ARCNET card.

A solution to this problem is the "ARCNET Multi-Tasker", a server program to be installed on each of the VAXstations that can channel the data requests of multiple processes through the VAXstation's single communications card. Work on this server is currently underway at NSCL, and should be completed in the Fall of 1989.

General Device Layer

The general device layer will be another layer in the data communications hierarchy, sitting above the ARCNET and ARCNET multitasker layers and below the application programs (see Fig. 1). Its function is to collect device data from other (non-VME) systems, such as CAMAC and MODICON, and to make it available to the VAXstation. Each system will need to have its own communications hierarchy, possibly patterned after the existing ARCNET hierarchy, and then interfaced into the general device layer. Then, all devices available will appear as a small set of general device types to the application programs, which won't need to be concerned with which system the data is coming from. Work on this layer is still in the discussion stage, but should begin sometime in 1990.

Pseudo-Device Layer

Another software enhancement planned is the implementation of a "pseudo-device" layer, which would sit between the general device layer and an application program (see Fig. 1).

Currently, data available to the control system are readings of actual devices (power supplies, beam current meters, ion gauges, motion controllers, etc.). Pseudo-devices readings would instead be derived from a mathematical formula involving actual, perhaps multiple device readings and whose setting commands are an inverse of the same formula. Work on this layer is expected to start in the fall of 1989 and progress though most of 1990.

Phase II Beamline Power Supplies

John Vincent, Tom Jones, Bill Harder, and Bill Numberger

Introduction

The Phase II beamlines consist mainly of superconducting magnets for steering and focusing the cyclotron beam. Energizing these magnets will require 50 20V/20A power supplies and 10 10V/100A power supplies.

Because the loads are superconducting and require different polarities depending on beam type and desired location, these supplies must be "4-quadrant". A 4-quadrant power supply has four regions, each of which supplies unique voltage and current combinations. (See Table I.) Since industry has rarely used superconducting technology, and has little use for 4-quadrant power supplies in general, these supplies are not available at a reasonable cost with the proper design for a superconducting load.

This paper will give a brief set of requirements for such power supplies, the design currently in development and construction, and the current status of the development and construction of these supplies.

Power Supply Regions

The four quadrants of operation referred to in the introduction refer to the four regions of a cartesian plot of "current vs. voltage". A region's polarity is defined by the polarity of its current. Adhering to normal engineering conventions, a positive current is defined as "positive charges flowing out of the '+' terminal of the power supply". The four regions, and the power supply requirements for each, are summarized in Table I.

Assuming zero lead resistance and magnet current at the desired level, the output of the power supply would be 0 volts at an arbitrary current. Any drift from the desired value would cause the regulation circuitry in the power supply to apply a voltage proportional to the error current, which would then bring the current back to the desired value. Depending on the sign of the current error, the compensation voltage would cause the power supply to operate in one of the four power supply regions in the table above.

TABLE I: Power supply regions.

Region	Power Supply Requirements
1	Positive voltage and positive current *Power supply acts as positive polarity source.*
2	Negative voltage and positive current *Power supply acts as positive polarity load.*
3	Negative voltage and negative current *Power supply acts as negative polarity source.*
4	Positive voltage and negative current *Power supply acts as negative polarity load.*

Performance Requirements

1. Switch Smoothly

In order to maintain a high degree of regulation, the power supply must be able to switch smoothly and rapidly from one quadrant to any other. This is the primary requirement of power supply performance.

2. Operate at Full Rated Voltage

For good regulation and to aid tuning, the power supply must be able to operate at its full rated voltage, regardless of the quadrant used or how close it is to its maximum rated output. The superconducting coils used are highly inductive and the rate of change of current in an inductive load is directly proportional to the applied voltage.

3. Maintain Uniform Current Levels

The power supply should be able to regulate the current within 0.01 percent and to quickly settle on a newly set current. Normally, many magnets are involved in transporting the beam. Tuning one of them typically requires the tuning of others such that the operator must continuosly tune one, then another, and iterate until the desired condition is achieved. It would greatly confuse and prolong the process if after each adjustment one must stop and wait a long time for the magnet to reach its target current and stabilize.

4. Withstand Varying Temperatures

As stated, the current level must be consistently uniform within 0.01 percent, and this must be despite the temperatures of the power supply coolant and environment. This requires that we carefully choose the components in the main regulation loop which affect the thermal stability of the supply. It further means that this loop must have little or no DC error and high gain.

5. Power Supply and Coil Protection

Protection of the power supply, and particularly the load, is an extremely important requirement. The large value of inductance and current in the load results in a great deal of stored energy. An interruption of the normal current path causes the current's change rate to approach infinity, leading to a high-voltage arc across the coil. This condition would certainly lead to catastrophic equipment breakdowns of both the coil and power supply. Because the coil is more difficult, expensive, and time-consuming to repair, protection apparatus should be most geared to protecting it rather than the power supply under the worst case conditions. The power supply must contain apparatus designed to protect itself under any circumstances, and also the load, assuming the connection to the load is not lost.

6. Interlock Monitoring

Superconducting coils have many other environmental requirements in order to operate properly and safely, such as lead gas flow, appropriate helium states and levels, lead temperatures, dewar pressures, etc. Various relationships between these values, or expected changes in them due to external events, in some cases warrant the magnet to be brought to zero current as quickly as possible. However, it is difficult to make the appropriate responses to external and internal events, taking into account the associated logic and the sheer magnitude of conditions sensed and their location with respect to a given magnet. Therefore, a programmable logic controller (PLC) is used. The power supply must have circuitry which reports to the PLC for power supply problems and states, and accepts inputs from the PLC to set states and respond to external interlock conditions.

7. Remote Controls

All of the magnets are inaccessible due to radiation when they are in use. In addition, it is desirable to have the power supplies as close to the magnets as possible, but it is also necessary to be able to control them from the Control Room. This requires the power supply to accept the current level command and feed back the current values of voltage and current by remote control. The power supplies must have remote control capability for value setting and monitoring, as well as for state setting, state monitoring, and interlock response.

8. Simplified Construction and Maintenance

There are a great many of these power supplies. The failure of a single power supply could disable an entire beamline. It's very difficult to work around a failed supply, so in general, for a given section of line to operate, all of the supplies on it must work. In addition, since there are so many to be constructed, they should be designed for relatively simplified mass production.

9. Efficiency, Noise Generation, and Cost

One last item which should be mentioned here, but is not considered to be an absolute requirement, is the question of efficiency. Superconducting coils are typically used to generate large magnetic fields in a much smaller space and with much less core material. However, they are also viewed as a very efficient magnet because no energy is dissipated to conduct the electrical current. Although superconducting coils are still more efficient than conventional coils, even if the power supply were 100% inefficient, it seems that it's right to make the power supplies at least 50% efficient.

This means that some of the regulation is done by switching techniques. However, switching power techniques generate noise, which, if not held to a minimum, will be picked up by the sensitive detectors used by the experimenters. So there exists a fuzzy line between efficiency and noise generation.

In addition, to drop the full power supply voltage at full current (which is what happens with a zero-volt load), more pass transistors are required than if only a fraction of the full power supply voltage is dropped. Transistors are expensive, so the benefits of dropping the full voltage must be weighed against the expense of building the equipment.

This section has briefly gone over the major requirements of the power supplies needed for the operation of the new superconducting beamline magnets. The next section will briefly go over the implementation of these requirements by presenting a general overview of the power supplies being designed and constructed.

General Design

The 10V/100A and 20V/20A power supplies have basically the same design. They mainly differ in the number or size of components. The phase-regulated section of the 10V/100A was economical to buy, whereas the 20V/20A's section was designed and built in-house. This section will treat the two as if they were identical by just describing the general design and steering away from specifics. The specifics are available in great detail if the reader wishes to make inquiries. This paper will also not address issues associated with packaging of the two supplies. The power supply may be broken up into the following functional blocks:

1. Phase Modulated Section
2. Transistor H-Bridge Pass Bank
3. H-Bridge Coupler Circuitry
4. Load and Power Supply Protection Circuits
5. Main Regulator and Interface Circuit

Each of these functional blocks will now be independently described.

1. Phase-Modulated Section

The phase-modulated section transforms the AC line power into appropriate levels of DC output power. It receives the AC power line and the input reference which determines the output voltage level, and it supplies the filtered DC voltage and current proportional to command input. On the 20V/20A power supply, this section also supplies DC voltages for the control circuits: +15 V, -15 V, +33 V, -33 V, and +5 V.

The section basically consists of a input line filter feeding a pair of SCR's, which feed the primary of the rectifier transformer, which feeds the rectifier, which feeds the choke input filter, which feeds the section's output terminals. Also in here is a PC board with a circuit supplying the constant DC levels for itself and other control electronics, and with electronics which control and supply the SCR trigger pulses. The circuit closes a voltage loop around the phase-modulated section by comparing 'command' to 'output voltage' and setting the SCR firing angle to maintain this ratio. The output voltage from this section is settable from 0 to full-scale positive. This was the first section designed and developed for this project.

2. Transistor H-Bridge Pass Bank

This is a water-cooled heatsink containing power FET's and BJT's that set the output polarity of the supply. The heatsink is fed by the output of the phase-modulated section. It also supplies various monitor points to the H-bridge coupler circuitry and receives its drive signal from that circuit also.

The FET's are turned on or off sharply, whereas the BJT's are linearly driven to maintain regulation. Figure 1 shows the basic circuit of the H-bridge. When transistors Q1 and Q4 are on, and Q2 and Q3 are off, the load's current is positive, whereas when Q1 and Q4 are off, and Q2 and Q3 are on, the load current is negative.

This heat sink also contains a dump circuit which turns on if the load voltage exceeds 1.2 times the maximum operating voltage of the supply. The dump circuit is com-

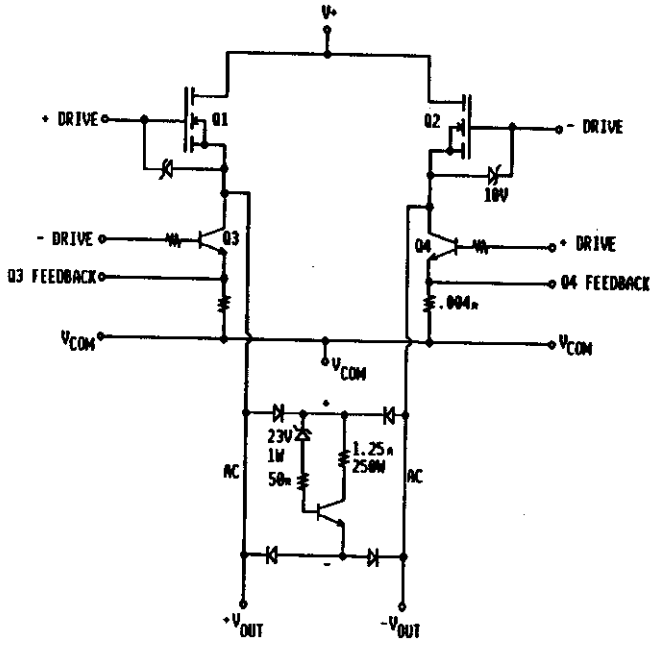

FIG. 1: Simplified schematic of H-bridge pass bank.

pletely driven by the load and would turn off only when the load voltage falls below 1.2 times the maximum operating voltage.

3. H-Bridge Coupler Circuitry

This is a PC board mounted over the H-bridge heatsink which contains the circuitry that drives the pass transistor and phase-modulated section. Each BGT group is driven by a voltage-controlled grounded-load current source. Each FET group is driven by a comparator-like op-amp arrangement. Depending on the polarity of the main error signal coming in the circuits, either the positive drive groups or negative drive groups are active.

The FET comparator circuits also have a pot-adjustable bias fed to them, which bias the positive and negative FET groups 'on' when the main error signal coming in is near zero. One pot simultaneously adjusts both sides. The BGT groups also have a single pot which biases the positive and negative drive groups simultaneously. This pot is adjusted to overcome the initial bias voltages necessary to turn the BGT's just slightly on whenever the main error signal is at zero. These bias circuits compensate for the large jumps at near zero, allowing a smooth transition from quadrant to quadrant.

This H-bridge PC board also has circuitry which monitors the BJT collector voltages. The difference between the positive- and negative-driven BJT collector voltages equals the load voltage. The BGT group which is currently regulating the load current is maintained at about 5 V VCE. This is done by taking the absolute value of the load voltage, adding 5 V to it, and using this as the command reference for the phase-modulated section. The difference between this voltage and the phase-modulated section's output voltage is amplified and fed back to the phase-modulated section's command input. Therefore, the phase-modulated section is basically following the current requirements of the regulator circuitry without being directly driven by it.

The main error signal on this board is generated by taking the difference between the command signal from the main regulator board, and the actual load voltage. Therefore, the main regulator board appears to be driving a voltage-controlled, voltage-regulating supply. Three signals are transported from this PC board to the main regulator board: the voltage command coming in, and the load voltage and load shunt current sent out. The main regulator board therefore deals with what appears to be a simple, voltage-controlled, bipolar, voltage-regulated power supply. It sees none of the phase-modulation complexities or the H-bridge control complexities.

As can be seen, the H-bridge coupler circuitry ties all these complex systems together. If this board and all of the systems controlled by this board are working properly and are stable, the main regulator board has a pretty standard problem to solve with respect to regulation and control system interface.

4. Load and Power Supply Protection Circuits

The load and power supply are protected by circuits in parallel with the power supply's load. If the power supply's current path is disrupted due to loss of a pass transistor or some other element, and the load has a large current in it, conceivably the power supply output voltage could increase to far beyond its rated value, thus damaging the supply. However, the dump circuit described in the H-bridge section would clamp the output voltage to only 1.2 times its

maximum rated value. This is necessary to protect the power supply's large electrolytic filter capacitors, which are normally rated for very low voltages. The superconducting loads we drive could easily handle four times the maximum output voltage without being damaged.

In addition to the dump circuit, there is a dump resistor in parallel with the load which can also drop the output voltage, by diverting the load's current. This dump resistor is rated so that it would develop a voltage four times the maximum rated output voltage. For example, assuming a power supply with a maximum rated voltage of V_{max} and a maximum rated current of I_{max}, the parallel dump resistor would be:

$$R = 4(V_{max})/I_{max}$$

Assuming the dump circuit was working, and the power supply was operating at I_{max} when the normal current path was disrupted, the resulting conditions would be:

$I_r = 1.2(V_{max})/R = 0.3(I_{max})$
$I_d = I_{max} - I_r = 0.7(I_{max})$
Where:
I_r = current in dump resistor and
I_d = current in the dump circuit

The voltage would remain at $1.2(V_{max})$ until $I_r + I_d < 0.3(I_{max})$. At this point the current in the load would deteriorate exponentially with a time constant of I_{load}/R.

Another protection feature is designed to prevent quenches and overheating in the event of a power failure. During a power failure we would want the current in the coils to automatically slowly decay. We don't want any dumps that could lead to quenches, creating abnormal pressures and cryogen conditions while we are unable to easily monitor and control these processes. Furthermore, whenever AC power is shut off to the supply, we can only assume we have lost power supply cooling. Stopping the current flow through the supply would prevent any unnecessary damage.

An integral dump switch serves this purpose well. This switch is held on by the AC power to the supply. Should the AC power be removed for any reason, such as operator shut-down or building power failure, the switch will change state. This "AC off" state prevents current from flowing through the supply, and places a resistor that is 1/4 the value of the dump resistor in series with the load current.

5. Main Regulator and Interface Circuit

This is a PC board we commonly refer to as the front panel board because it contains meters, LED's, knobs, adjustments, etc. which protrude through the front panel of the power supply. This board contains circuitry which:

-- regulates the load current
-- responds to the PLC external interlock signal
-- interfaces to the control system current command and supplies load and current values back to the control system
-- isolates all of these circuits from the rest of the power supply
-- maintains the internal maximum limits for the power supply
-- maintains user-settable addition limits for voltage and current
-- maintains front panel displays for voltage, current, limit status, and external interlock status

Current Status of Beamline Power Supply Design, Development, and Construction

This is the status of the beamline power supplies as of June 19, 1989.

The final development of the main regulator and interface circuit is in progress and should be complete within two weeks.

20V/20A Power Supply

The packaging design should be finished this week. A prototype of the supply has been around for some time now and has successfully operated a beamline magnet. Fifty supplies will be built. All 50 of two of the supply's three PC boards have been stuffed. Most of the parts have been ordered, and some are already in; all parts should be ordered within the next two weeks. The power supplies should be rolling out of our assembly line within the next two months if all goes well.

10V/100A Power Supply

The 10V/100A power supplies are currently being designed. This power supply will use all of the same control PC boards as the 20V/20A. Many of the parts for the prototype are now ordered. The mechanical design for the H-Bridge heat sink should be finished this week and submitted to the shop for fabrication. Transistors for all of the 10V/100A power supplies were ordered along with the transistors for 20V/20A supplies. Packaging design for the 10V/100A is now in progress. We are aiming to have a working prototype for this power supply by mid- to late August. By that time all parts for these supplies should be on order.

Current Status of the K1200 RF

John Vincent, John Brandon, and Jack Ottarson

Introduction

Last year's Annual Report described the initial operation of the K1200 RF system. From that time until June 6, 1988, the RF system ran frequently for internal beam development, culminating on June 6 with the first extracted beam. After this, the experimental program began and the operation of the accelerator gradually transferred from the Accelerator Physicists to the Operators for daily tuning and operation. The energies were moving up and the associated dee voltages were also. We typically now operate beams which require peak dee-voltages from 110 kV to 130 kV.

Minor problems occurred all along; however, on May 25, 1988, we started experiencing main RF amplifier tube failures. We also had dee stem insulator failures and coupler plating problems. This paper will describe these problems and other RF issues.

RF Amplifiers

As mentioned above, the main problem with the RF amplifiers is the premature failure of the main RF vacuum tube. The main power tube used is the RCA 4648 tetrode. We initially paid about $28k for each tube. New tubes cost about $50k each and have a minimum of nine months delivery time. Rebuilding a tube costs about $23k and takes from four to six months. At these prices and with the long delivery times, premature failures are a major problem.

The new RCA tube brochure also designates this tube as "Not recommended for new designs", which is also not a good sign.

Because of this problem, we decided to retrofit one of our amplifiers with a different tube which is more easily available and less expensive, a Thomson TH555. NSCL RF Note #107 describes the problem and choices made in detail. Tables I and II summarize the history of this problem.

TABLE I: K1200 tube history.

'A' RF Amplifier				
Date	Tube	Status	Hours	Down Time
1/15/88	U3-4648	begin Ops	0	-----
4/25/88	U3-4648	grid short	323	maint.
4/30/88	Z109-4648	grid short	30	4/30-5/17/88
6/21/89	J105-4648	running	3029	-----

'B' RF Amplifier				
Date	Tube	Status	Hours	Down Time
1/15/88	J105-4648	begin Ops	0	-----
5/17/88	J105-4648	moved to A	309	maint.
4/05/89	Y105-4648	to storage	2143	maint.
6/21/89	U1R1-4648	running	850	-----

'C' RF Amplifier				
Date	Tube	Status	Hours	Down Time
1/15/88	U1-4648	begin Ops	0	----
7/20/88	U1-4648	grid short	494	7/20-9/22/88
2/25/89	U3R1-4648	grid short	1620	2/25-3/14/89
6/15/89	TH555-1	?	771	6/10-6/18/89
6/20/89	TH555-2	running	150	----

TABLE II: 4648 repair history.

Amplifier	Tube	Failed	Shipped for Repair	Received Back
A	U3	4/25/88	5/05/88	9/20/88
A	Z109	4/30/88	7/21/88	5/02/89
C	U1	7/20/88	7/21/88	3/22/89
C	U3R1	2/25/89	No Plan	-----

TABLE III: Current amplifier configuration.

Amplifier	Tube	Configuration Date	Total Filament Hours
A	J105	5/17/88	3338
B	U1R1	5/17/88	850
C	TH555-2	6/20/89	150

TABLE IV: Current spare tube inventory.

Tube	Status
Y105	Undamaged tube on loan from Oak Ridge until next May with 2,143 cathode hours on it from here and about 10,000 hours of service at Oak Ridge. This tube is ready for service if needed.
TH555-1	First Thomson tube used here for 771 hours before the screen began to spark for unknown reasons. It is not currently known whether this tube is damaged. It is highly suspect at this time.
Z109R1	Newly rebuilt tube ready for service if needed.
U3R1	This was the first tube rebuilt. It ran for 1,620 hours before it failed again in C. There are no plans to rebuild it.

Tables III and IV summarize our experience with the RF amplifiers to date. The C-amplifier which has been retrofit to use the TH555, has been successfully driving the 'C' dee resonator, but is still in development as well. We have not yet verified whether the first TH555 failed under the stress of development.

The C-amplifier also tends to self-excite at the operating frequency. We've tried various neutralizing schemes to prevent this from happening. It was first believed that the problem was due solely to the 4 pF of grid-to-plate capacitance. Now, however, we're preparing to test the effect of the screen lead inductance, which is mainly caused by the manufacturer's tube socket design. If the screen lead inductance proves to be a large part of the problem, we shall design, build, and install new parts to eliminate the problem altogether. At that point we shall re-determine the neutralizing requirements and respond accordingly.

Operation of this amplifier now requires a temporary adjustable neutralizing circuit, and a load on the transmitter output, which consumes about 33% of the power available for the dee resonator. This not acceptable in the long run, since it would deny the dee resonator enough power for higher energy beams in the future.

Clearly, there are unresolved issues with this retrofit at present. Our experience in the next few months should steer us toward correct amplifier decisions.

Aydin Power Supply

Transformer problems with this power supply have been the subject of many other reports; however, the problems now appear to be coming to an end. We now have two transformers which appear sufficiently robust.

A rectifier failed on November 4, 1988, and the rectifier choke was repaired at a cost of about $18k. A second failure occurred on May 25, 1989, and the rectifier is now being repaired. We are now moving the rectifier choke connections from the high voltage side of the supply to the return side and adding two spark gaps in parallel with it, set to turn on if the voltage exceeds 25 kV. We also are adding a door and inspection port to the enclosure that houses these spark gaps, to allow easy weekly inspection and calibration if necessary. This is expected to solve the problem.

The repaired enclosure should be back and reinstalled about June 30, 1989. We are currently using the K500 anode power supply to feed the K1200 RF amplifiers so we can continue operation. The beams running for the next few months sometimes push the K500 supply to its designed limit, but it appears to be handling it.

RF Input Couplers

Last year's Annual Report discussed problems with the input couplers plating and eventually failing. We have since modified the coupler shield rings and tested other ideas. We've had significant improvements since then and these couplers seem to operate longer; however, they still are not good enough. Table V lists the failures recorded since the initial batch were modified.

TABLE V: Coupler failure history.

Coupler	Failure Date
B System	11/26/88
B System	5/18/89
A System	5/30/89

Apparently, the insulator-to-metal joint is eroded by electron bombardment and sprays metal on the insulator. This causes increased localized RF heating of the insulator and reduced metal in the joint, leading to either an insulator crack or a vacuum leak. It is not clear whether the braze joint is the only thing spraying metal onto the insulator, although it appears to be a major one.

The electron emission in this area is presumably enhanced by alumina's secondary electron emission, which varies from about 3 to 9 just about everywhere away from a few keV. Therefore, electron resonant mechanisms such as multipactoring are not necessarily the only possible cause of severe erosion and insulator heating, but such mechanisms are not ruled out.

A very thin deposit or diffusion of titanium over the insulator and surrounding areas could help. Titanium has a secondary electron emission of less than 1 and should prevent electron resonant mechanisms from building up, while greatly reducing other destructive mechanisms as well. However, the titanium, heated by the RF, will transfer heat to the insulator. To prevent localized heating of the insulator, this layer would need to be rather uniform. In addition, if too much titanium in present, RF operation could be adversely affected. So, a very thin, relatively uniform layer is required, of sufficient thickness to prevent stray electrons from hitting the alumina. A furnace for this and other projects is currently under construction.

A straightforward improvement involves placing the braze on the air-side of the insulator, hence removing the joint from direct electron bombardment in vacuum. We have an insulator designed in this way and a coupler is being assembled with it. This should greatly reduce the problem, if not completely eliminate it. Such a coupler will be installed for long-term evaluation as soon as possible.

Corona Rings and Dee Stem Insulators

The dee stem insulators serve as vacuum windows between the cyclotron beam chamber and the RF tuning stems. One side of the insulator presses against the vacuum-side outer-conductor spinning and the other side presses against the inner-conductor corona ring. To make a good seal between these surfaces, a strand of indium wire is placed in the joint between the insulator and copper surfaces. We have two problems here: voltage-holding (sparking) and vacuum leaks developing over time. Table VI lists the vacuum problems.

TABLE VI: Dee stem insulator failures.

Date	Failure	Insulator	Old Indium	New Indium
1/09/89	Indium leak	C upper	40 mil	30 mil
2/01/89	Cracked insulator	A lower	40 mil	30 mil
2/21/89	Cracked insulator	C lower	40 mil	30 mil
5/30/89	Indium leak	B upper	40 mil	30 mil
5/30/89	Cracked insulator	B lower	40 mil	30 mil
6/20/89	Indium leak	A upper	40 mil	30 mil
6/20/89	Cracked insulator	A lower	30 mil	30 mil

A couple of ideas about this come to mind. First, indium creeps and does not have any elasticity; in other words, it can squash but not spring back. Therefore, it cannot respond to pressure changes around the insulator, leading to leaks. Secondly, the 40-mil indium flows out from under the insulator, making intermittent electrical contact with the surfaces. This contact causes RF current flow, leading to excess heating. The excess temperature caused by the exposed indium probably enhances emission of electrons, which

encourages sparking in these areas. The exposed indium also melts and runs over the insulator, leading to breakdowns. A third probable cause of problems is that the insulator contact areas are not shaped to maintain the electric field to a minimum. Here are the corona ring and insulator problems perceived so far:

1. Leaks caused by inelastic indium,
2. Overheating from indium flow,
3. Sparking caused by insulator area-geometry,
4. Sparking caused by insulator placement, and
5. Sparking caused by inadequate air flow.

In-depth discussion of each follows.

1. Leaks Caused by Inelastic Indium

The only way to prevent the first problem is to seal the insulators in some other way. C-seals were used on the K500 for a while but had problems. To my knowledge, O-rings have never been tried in this location. If O-rings are to be tried at some future time, they should preferably either be manufactured of pure butyl rubber or silicone rubber. The latter is the best material for RF Q and helium permeability. There are currently no plans to try another method of sealing this vacuum joint.

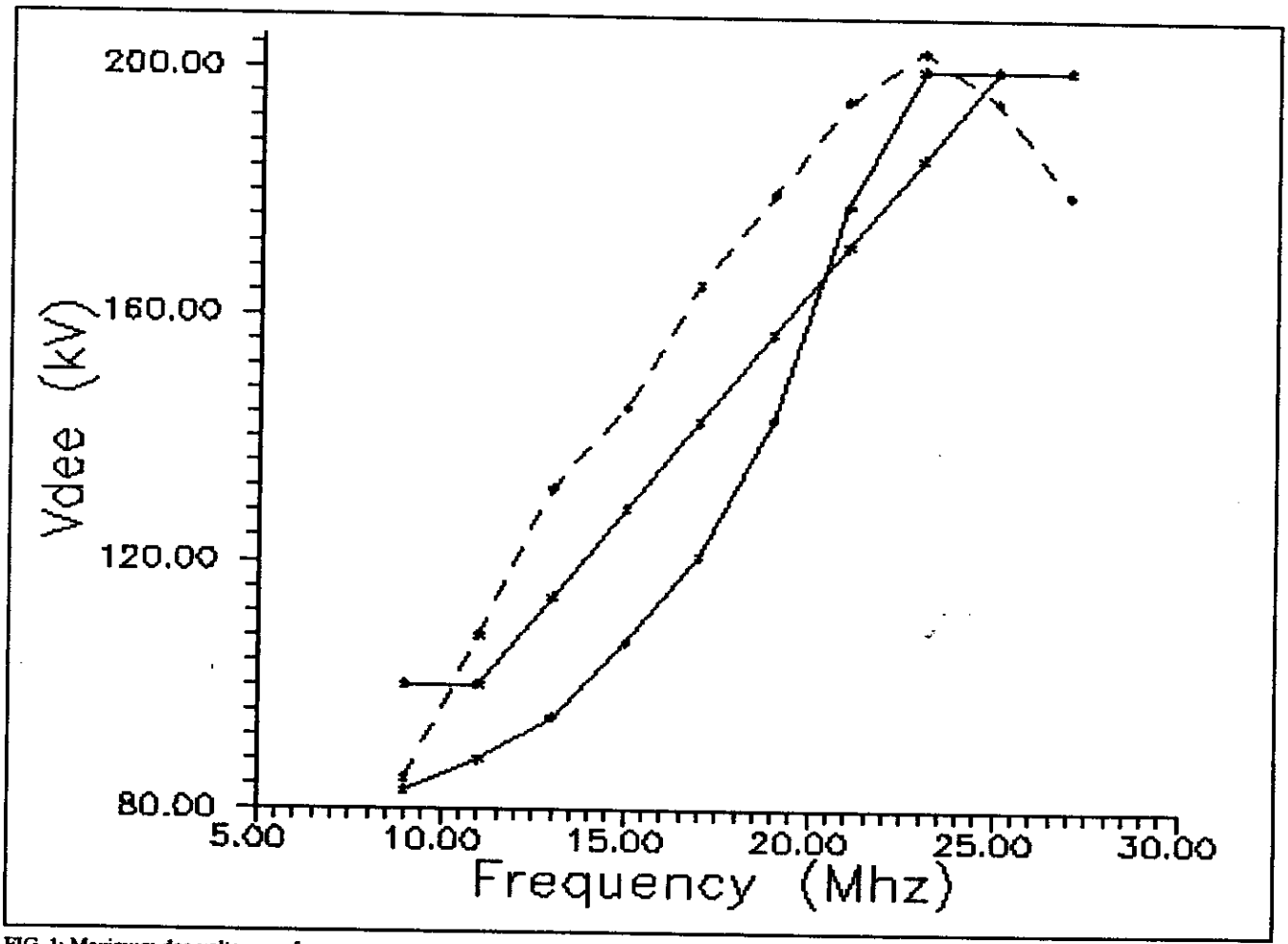

FIG. 1: Maximum dee voltage vs. frequency.

2. Overheating from Indium Flow

The indium flow problem can be addressed by using 30-mil indium instead of 40-mil. Although the table shows that A-lower developed a vacuum leak with 30-mil, the burning was much less severe.

3. Sparking Caused by Insulator-Area Geometry

The third concern is being addressed by a Poisson study of the fields in these areas. The results of this study should show the problem areas, and changing the geometry, we may be able to improve it. Of course, any change in geometry in these locations which would have any significant effect would probably result in significant down-time.

Another alternative is to mock up this geometry and do high-pot tests to determine the location of the sparking. This test should be done to verify the initial findings of problem areas from the study and to find out if any of the proposed modifications work.

The last way to solve this problem is to increase the number of beam turns required for acceleration.

4. Sparking Caused by Insulator Placement

One other item that may have hindered this situation is the insulator's placement. The insulator was designed for a certain maximum dee voltage, which has since changed. The insulator was placed closer to the dees to reduce the cavity overall losses by about 33%, which increases the voltage in its vicinity. Not only did the location change, but the intended operation of the cyclotron did as well. The cyclotron was initially intended to be radially injected. Now that it is injected in the center, the necessary maximum dee voltage has apparently increased across most of the RF frequency band.

Figure 1 displays three plots as a function of RF frequency. The dashed, curved plot is the maximum dee voltage needed to run the machine with the ions we are currently using. The solid, straight-line plot is the maximum dee voltage the resonator was designed for. The solid, curved plot is the maximum operating dee voltage that may presently be run without putting the insulators at risk.

5. Sparking Caused by Inadequate Air Flow

The air flow for each insulator is supplied by a high-volume blower which blows air into a plenum between the magnet iron and the air-side outer-conductor spinning. From the plenum, the air is blown through small angled holes in the spinning which point at the dee stem insulator. The hole angles are set so that the air spirals about the insulator.

Although there is much turbulence at the bottom of the insulator near the holes, a few inches up the insulator the air flow is barely discernable; air does spiral around the insulator, but the air flow is inadequate to blend the atmosphere in the cavity. We suspect this creates problems at the corona rings, where ions and gases such as ozone can build up, leading to sparks.

We are currently drilling 0.25-inch-diameter holes in the spinning to increase the overall flow. The 'B' resonator is being altered first to gain a qualitative feeling for the change between it and the unmodified ones. If the test shows any improvement, we will modify the other resonators as well.

Trivial Problems

Three of these come to mind. First, the dee-to-dee RF phase does not always regulate perfectly. However, no absolute problem has been shown here yet. Second, the dee-to-dee phase meter, which displays the absolute RF phase-angle between A-B and C-B, drifts and is very inaccurate. Third, we still want to build the RF control computer.

These problems are slowly being addressed and will be solved eventually; they are presently not top priority.

Conclusion

All told, the RF system project has gone remarkably well. It was only three weeks after the very first high-power runs were ever attempted that we began internal beam development. For a new RF system of this complexity, this is a feat which has rarely been matched. Of course, when higher energy beams began operation, requiring increasingly higher dee voltages for prolonged periods of time, problems began to emerge. These problems are being

addressed and we hope to have them solved this year. If we can accomplish this, the RF system should be much more reliable for beams requiring dee voltages of up to about 150 kV peak.

Programmable Logic Controller Use in the Phase II Control System

G. Humenik, D. Scott

Introduction

Most of the routine low-power switching of cyclotron and beamline hardware is done using programmable logic controllers (PLC's). This has been done to avoid using electro-mechanical relays. There is still a need for relay-controlled power transfer; however, the "logic" function which previously was hard-wired between banks of relays is now written in PLC software. The PLC inputs and outputs are optically isolated, and the field hardware generally uses 24 VDC.

The tremendous increase in flexibility attained by replacing hardware with software was further enhanced by the inherent self-documentation of the PLC "ladder" logic programs. Nowhere was this more apparent than during the recent Phase II upgrade of the old K50 vault into the new Transfer Hall. The K50 relay-type logic wiring was far easier to tear out than understand, given the lack of accurate documentation about it. The K50 relays also used 120 VAC signals, which meant that trying to trace or change their functions was never dull.

PLC History at NSCL

Equipment Acquisition

The Lab has been using PLC's in various capacities since 1978, when the K500 vacuum system and RF control was implemented with a Modicon 484 PLC. This 2nd-generation processor allowed 4K of logic, 256 inputs, and 256 outputs. For the first time, rapid alterations of complex interlock patterns could be designed and installed in real-time, without the headaches of consulting and correcting schematics, or the annoyance of shutting down the device or process to rewire terminal strips.

More capacity was needed for the K500 beamline, and later for the K1200 vacuum system, so in 1981 we acquired a 16K processor (Modicon 584A), capable of 3072 inputs and 3072 outputs. The 584A could be located over 10,000 feet from its I/O hardware, connected in a multidrop topology using a 1.5M baud serial data protocol. Initially, there were two I/O drops; later, four more were added to pick up operations of the K1200 cyclotron, 92" scattering chamber, and 4π detector. When the ECR was set up in 1986, a separate smaller PLC (884) was installed to allow control system independence. This same approach was used for the K1200 RF with a second 884 PLC. In 1987, a fast new processor, the 984A, was acquired for the K1200 trim coil power supplies. A second manufacturer of PLC's, Square-D, supplied a fifth PLC (Symax 300); this is used solely for the radiation protection system at the Lab.

Equipment Usage

One enhancement that the 584A, 984A and the two 884s possessed was the ability to form a master-slave network with Lab computers, using a 9600 baud RS-232 link and Modicon's MODBUS serial protocol. However, this was a laborious process, and was only used to occasionally connect the 584A to a VAX-750 for logic documentation and PLC program archival. In 1987, intelligent (programmable) color video terminals became available with MODBUS capability. Connection to the PLC's and VAXes was now relatively effortless, and the operator interface could be altered as quickly as the logic itself.

With the proliferation of PLC's and intelligent terminals, it became obvious that it would be necessary to network them. The method chosen involves a MODBUS 9-port multiplexer, which allows any combination of masters (video terminals) and slaves (PLC's) to communicate simultaneously and at different speeds. Recently, a second multiplexer was acquired; further networking will be done at 19.2 Kbaud to quicken terminal display updates.

The advent of the intelligent terminal seemed to argue against having many small PLC's distributed about the building. One large PLC is faster to interrogate, and reduces the need for inter-PLC relays for logic information sharing. Late in 1988, the hardware specification for the Phase II

beamlines allowed a projected inventory of future PLC input and output hardware. It was apparent that the 584A would barely be able to absorb the increased logic and hardware load. Rather than getting a fifth mid-size PLC, we decided to replace the 584A. All 584A functions would be transferred to the new PLC, and all Phase II PLC operations as well.

Current Status

Replacement of 584A with 984B

In February of this year, we acquired a Modicon 984B. This PLC has 64K of logic space, and is configured for 3000 inputs and 8192 outputs. The reason for so many more outputs is due to terminal interaction. In order for an intelligent terminal to change the PLC logic, a PLC software output must be turned on or off via MODBUS. So, as the intelligent terminals release hardware inputs, they use up software outputs. In the current 984B configuration, 2000 outputs are set aside for hardware devices, 3000 outputs are software-only use, and 3192 outputs are allocated for use by the terminals. Also, the 984B has three MODBUS ports, and solves logic four times faster than the 584A. As Phase II completes, the 984B will encompass more than 75% of all PLC operations.

To replace the 584A logic with 984B logic involved considerable planning. One interesting peculiarity of the Modicon PLC family is the users' ability to change the program in the processor while that program is running, provided that only one network (page) at a time is changed. Over the last seven years the 584A has had many logic changes done in this fashion. The unfortunate result was highly-patched code which had made much of the logic hard to follow. Also the labeling and numbering of outputs was quite haphazard, especially considering that numerous outputs were now used as MODBUS inputs.

While the 984B was still offline, the 584A logic program was entered is "by hand". This process allowed the 584A logic to be significantly altered in a comprehensive manner. Areas in logic, and the numbering of elements, now completely correspond to the physical location of the I/O hardware. Some systems, notably the K500 RF system, were totally rewritten to allow full use of the new display devices and/or to streamline their operation. The 984B came on-line in June of this year, with 12K of logic using 450 networks.

Problems Encountered

Along with the new PLC, four new I/O drops were installed to handle all of Phase II discrete control needs. All the coaxial cabling was re-routed to allow each I/O drop to be within 3 feet of its tap. The only real problems associated with the entire PLC changeover involved both the new I/O drop hardware and the 984B's communication to them. These problems have only been made manifest in August, 1989 while running K500 beams to the N1 (S320) Vault. The I/O communication hardware either locally (one drop) or globally (all drops) would momentarily cease to communicate with the PLC, causing all manner of inconvenient device shutoffs and closures. After replacing hardware under warranty, the problem has been fixed.

Conclusion

In the future, the discrete control system changes most visible to the cyclotron users will be in the implementation of true graphic displays of all controllable devices. This will allow a greater information density per screen, and a common-sense grouping of all system interlocks and controls. Further work will involve expanding the primitive link between the main console's VAX workstations and the intelligent terminals.

Relations Among Cell Matrix Elements in Second-Order Optical Beam Achromats

D. Ioanoviciu and J.A. Nolen Jr.

A magnetic optical beam achromat transports a charged-particle beam without adding any second-order aberrations.[1] At least four identical cells are needed, with generally two hexapoles in every cell.[2] It is of interest to determine under what conditions it is possible to simplify the structure of such an achromat. The cell number cannot be reduced to less than four, but the individual cell structure can be simplified in some cases. A deeper knowledge of the relations among cell-transfer matrix elements is essential to identify such geometries.

The following matrix element notations are used: w for the whole system, h for half-system, c for cell. Symbols for the first row are in lower case and symbols for the second row are capitalized. In the following equations, x denotes radial distance, α denotes radial angle, y denotes axial distance, β denotes axial angle, and δ denotes the relative energy difference.

Let us remember the first-order relations in a quarter wave cell[1]:

$$c_x + C_\alpha = c_y + C_\beta = 0 \tag{1}$$

Successive matrix multiplications then produce:

$$h_x = H_\alpha = -1 \tag{2}$$

$$h_\alpha = H_x = 0 \tag{3}$$

In the four-cell achromat, w_δ and W_δ vanish, as well as all the second-order geometric aberrations w_{jk}, W_{jk} where j and k stand for x, α, y and β.

The relations (1) being satisfied, only the second-order chromatic (pure and mixed) coefficients are dependent on the cell's second-order properties. As will be shown below, only two conditions must be fulfilled to cancel all the 10 chromatic coefficients of the whole system.

First, let us express the whole system coefficients using only those of half the system. The radial coefficients are:

$$w_{x\delta} = -(2h_{x\delta} + h_\delta h_{xx} + H_\delta h_{x\alpha}) \tag{4}$$

$$w_{\alpha\delta} = -(2h_{\alpha\delta} + h_\delta h_{x\alpha} + 2H_\delta h_{\alpha\alpha}) \tag{5}$$

$$w_{\delta\delta} = -\frac{(h_\delta w_{x\delta} + H_\delta w_{\alpha\delta})}{2} \tag{6}$$

$$W_{\delta\delta} = -\frac{(h_\delta W_{x\delta} + H_\delta W_{\alpha\delta})}{2} \tag{7}$$

$$W_{\alpha\delta} = -(2H_{\alpha\delta} + h_\delta H_{x\alpha} + 2H_\delta H_{\alpha\alpha}) \tag{8}$$

$$W_{x\delta} = -(2H_{x\delta} + 2h_\delta H_{xx} + H_\delta H_{x\alpha}) \tag{9}$$

These coefficients are not all independent: if (4), (5), (8), and (9) vanish, then (6), and (7) vanish too.

The axial coefficients are:

$$w_{\delta y} = -(2h_{\delta y} + h_\delta h_{xy} + H_\delta h_{\alpha y}) \tag{10}$$

$$w_{\delta\beta} = -(2h_{\delta\beta} + h_\delta h_{x\beta} + H_\delta h_{\alpha\beta}) \tag{11}$$

$$W_{\delta y} = -(2H_{\delta y} + h_\delta H_{xy} + H_\delta H_{\alpha y}) \tag{12}$$

$$W_{\delta\beta} = -(2H_{\delta\beta} + h_\delta H_{x\beta} + H_\delta H_{\alpha\beta}) \tag{13}$$

By using the simplecticity relations:[3]

$$H_{\alpha\delta} + h_{x\delta} = H_{x\alpha} + 2h_{xx} = 2H_{\alpha\alpha} + h_{x\alpha} = 0 \tag{14}$$

for the radial plane and

$$H_{\delta\beta} + h_{\delta y} = H_{x\beta} + h_{xy} = H_{\alpha\beta} + h_{\alpha y} = 0 \tag{15}$$

for the axial direction, we prove the identities:

$$W_{\alpha\delta} = -w_{x\delta} \tag{16}$$

$$W_{\delta\beta} = -w_{\delta y}\,. \tag{17}$$

The following simplecticity conditions are written at the cell level. The radial coefficients:

$$2c_\alpha C_{xx} = 2C_\alpha c_{xx} - C_x c_{x\alpha} + c_x C_{x\alpha} \quad (18)$$

$$c_\alpha C_{x\alpha} = C_\alpha c_{x\alpha} - 2C_x c_{\alpha\alpha} + 2c_x C_{\alpha\alpha} \quad (19)$$

$$c_\alpha C_{x\delta} = c_x C_{\alpha\delta} - C_x c_{\alpha\delta} + C_\alpha c_{x\delta} \quad (20)$$

and axial coefficients:

$$c_\beta C_{xy} = c_y C_{x\beta} - C_y c_{x\beta} - c_y c_{xy} \quad (21)$$

$$c_\beta C_{\alpha y} = c_y C_{\alpha\beta} - C_y c_{\alpha\beta} - c_y c_{\alpha y} \quad (22)$$

$$c_\beta C_{\delta y} = c_y C_{\delta\beta} - C_y c_{\delta\beta} - c_y c_{\delta y} \quad (23)$$

reduce the 10 initial conditions to the following two. For the radial plane:

$$\frac{w_{x\delta}}{c_x} = \frac{w_{\alpha\delta}}{c_\alpha} = \frac{W_{x\delta}}{C_x} \quad (24)$$

$$= -[(2c_{xx} + C_{x\alpha})h_\delta + (c_{x\alpha} + 2C_{\alpha\alpha})H_\delta + 2(c_{x\delta} + C_{\alpha\delta})]$$

$$= 0$$

and for the axial direction:

$$\frac{w_{\delta y}}{c_y} = \frac{w_{\delta\beta}}{c_\beta} = \frac{W_{\delta y}}{c_y} \quad (25)$$

$$= -[(c_{xy} + C_{x\beta})h_\delta + (c_{\alpha y} + C_{\alpha\beta})H_\delta + 2(c_{\delta y} + C_{\delta\beta})]$$

$$= 0$$

Generally, the equations (24) and (25) can be satisfied simultaneously by two particular hexapole component values (another way to derive the result of reference 2). However, several particular cases should be noted, such as when the system (24), (25) has no solution, or when the two equations become identical. The last possibility would offer the major simplification of less than two hexapoles/cell needed.

By using these conditions, beam achromat parameters may be calculated with high accuracy. There are computer programs allowing the calculation of the global parameters of the whole achromat. In this case the vanishing of too many coefficients must be monitored simultaneously, and the final accumulated errors are four times higher for a given limit of the computer accuracy.

References

1. K.L. Brown, SLAC - PUB - 2257 (1979).
2. D.L. Carey, Nucl. Instrum. Methods 189, 365 (1981).
3. H. Wollnik and M. Berz, Nucl. Instrum. Methods Phys. Res. A238, 127 (1985).

Interchanging Electric and Magnetic Components in Second-Order Optical Achromats: Some Particular Geometries

D. Ioanoviciu, J.A. Nolen Jr., and B. Sherrill

The second-order beam achromat principle stated in Ref. 1 for magnetic cells was generalized for electric and mixed cell components in Ref. 2. Here, the conditions to be satisfied when magnetic and electric components are interchanged will be detailed and some particular geometries given.

An achromat cell may contain dipole, quadrupole, and hexapole elements (higher order components do not contribute to aberrations at the level of interest). Normal entry and exit for homogeneous field magnets and cylindrical electrodes are to be preferred, being the simplest to machine.

First we consider a tuned cell of an all-magnetic second-order achromat. The replacement of a homogeneous magnet by a cylindrical condenser changes the first- and second-order properties simultaneously. Then, not only hexapoles must be re-tuned, but possibly the entire cell reshaped. The substitution of magnetic quadrupoles by electric ones leaves the first order properties of the cell unchanged, if the following condition is satisfied:

$$\frac{B_q}{A_{qb} BR} = \frac{V_q}{A_{qe}^2 V_a} \tag{1}$$

where B_q is the magnetic induction at the pole tip, BR the particle magnetic rigidity, $\pm V_q$ the applied voltage, eV_a the particle energy (e the elementary charge, for single charged particles); A_{qb} and A_{qe} the half-aperture of the magnetic and electric quadrupoles respectively. Because the second-order aberrations of the magnetic and electric quadrupoles are different, their substitution requires hexapole re-tuning.

The substitution of magnetic hexapoles by electric hexapoles keeps the cell tuned if:

$$\frac{B_h}{BR A_{hb}^2} = \left(\frac{3}{2}\right) \frac{V_{he}}{V_a A_{he}^3} \tag{2}$$

where B_h is the magnetic induction at the hexapole tip; $\pm V_h$, the applied voltage; A_{hb} and A_{he}, the half aperture of the magnetic and electric hexapole, respectively.

The above assertions were tested on particular geometries using the computer program GIOS.[3] Four cell achromats were considered. The cell components, following the ion path are: drift space *D1*, multipole *M*, second drift *D2*, dipole *S*, drift *D3*, hexapole *H*, drift *D3*, quadrupole *Q*, drift *D1*. For all the tabulated geometries, *D2* = 0.1 m, *D3* = 0.01 m, quadrupole and multipole length is 0.2 m, hexapole length is 0.08 m, the dipole deflecting angle 60°. In Table I, the field given in Teslas indicates a magnetic component, and applied voltage in kilovolts indicates an electric component.

The first cell belongs to an all-magnetic achromat. Substituting electric multipoles the second case results, with mixed (electric + magnetic) cell structure. Replacing the magnetic homogeneous field sector with an electric cylindric deflector reshapes the cell (see change in drift *D1*). (See data on the all-electric achromat in the third row of the table.) Another mixed structure results by introducing magnetic multipoles in the all-electric cell (see the last row of the table).

By using the magnetic fields tabulated in the first and last rows of the table, and using formula (1), we calculate V_q for the second and third case:

$$V_q = -2.79181 \text{ and } -5.57330 \text{ kV},$$

which are in good agreement with the values fit by GIOS and listed in Table I.

The whole achromat matrix elements obtained with GIOS for the all-electric case are given below. The row/column notation is used for the quoted matrix elements:

[x/x] = 1	[x/α] = 8 E-07	[x/δ] = 4.9 E-13
[α/x] = -1.5 E-06	[α/α] = 1	[α/δ] = 1.2 E-06
[x/xx] = -1.4 E-05	[x/xα] = 5.9 E-07	[x/xδ] = 8.0 E-06
[x/αα] = 3.4 E-06	[x/αδ] = -7.3 E-11	[x/δδ] = -1.7 E-06
[x/yy] = 1.1 E-05	[x/yβ] = -4.8 E-05	[x/ββ] = -9.8 E-06
[α/xx] = -3.1 E-06	[α/xα] = 2.8 E-05	[α/xδ] = 8.6 E-06
[α/αα] = -2.9 E-07	[α/αδ] = -8.3 E-06	[α/δδ] = -4.1 E-06
[α/yy] = -3.1 E-06	[α/yβ] = -6.1 E-05	[α/ββ] = 2.9 E-06
[y/y] = 1	[y/β] = -1.0 E-06	
[β/y] = 2.2 E-06	[β/β] = 1	
[y/yx] = 6.1 E-05	[y/yα] = -4.8 E-06	[y/yδ] = -1.3 E-05
[y/βx] = -5.9 E-06	[y/βα] = -2.0 E-05	[y/βδ] = 2.6 E-09
[β/yx] = -6.1 E-06	[β/yα] = -2.1 E-05	[β/yδ] = 4.8 E-06
[β/βx] = -6.1 E-05	[β/βα] = 4.8 E-05	[β/βδ] = 1.3 E-05

TABLE I: Achromat cell parameters.

Drift	Multipole M		Dipole S	Hexapole H	Quad Q
$D1$	B_q or V_q	B_h or V_h	B or V	B_h or V_h	B_q or V_q
1.0627m	-0.09474T	0.11962T	0.20361T	-0.23888T	-0.09474T
1.0627m	-2.79168kV	2.06147kV	0.20361T	-4.68985kV	-2.79168kV
0.0768m	-5.57323kV	19.7823kV	0.8kV	-50.3488kV	-5.57323kV
0.0768m	-0.18913T	1.04251T	0.8kV	-2.56321T	-0.18913T

References

1. K. L. Brown, SLAC-PUB-2257 (1979).

2. D. Ioanoviciu and J.A. Nolen Jr., Bull. Am. Phys. Soc. 33, 986 (1988).

3. H. Wollnik *et al., Manual for GIOS,* (II Physikalisches Institut, Justus Liebig Universitaet Giessen, version T4M, 1985).

Kinematic Effect Correction by Wien Filters

D. Ioanoviciu

The dependence of the nuclear reaction product-energy on the reaction angle induces an image broadening in nuclear spectrometers. This is called the kinematic effect.[1] The effect was corrected in magnetic spectrographs by moving the detector[2], or by slightly adjusting a quadrupole component.[3]

If a crossed-field analyzer (e.g. Wien filter) is used as a spectrograph, the kinematic effect can be eliminated by changing the intrinsic parameters of that analyzer, without need for additional components or detector displacement.

By using the matrix elements for non-relativistic particles[4] and those given by Roussel,[5] we obtain the focusing condition for particles undergoing the kinematic effect K:

$$\sin(kZ)\left(\frac{1}{k} - klL + 2b2\frac{KL}{k}\right) + \cos(kZ)\left(1 + L - 2b2\frac{K}{k^2}\right) + 2b2\frac{K}{k^2} = 0 \qquad (1)$$

where $K = (1/p)(dp/d\Theta)$, p being the particle momentum, Θ the reaction angle, l the analyzer target drift length, L the analyzer detector drift length, Z the main path length inside the analyzer, and k and $b2$ being detailed in Ref. 3. In the absence of the kinematic effect the usual angular focusing is satisfied for some value of k denoted $k0$:

$$\tan(k0Z) = \frac{k0(1 + L)}{k0^2 lL - 1} \qquad (2)$$

For a Wien filter, the relation (1) simplifies to:

$$\sin\left(\frac{Z}{R}\right)\left(1 - \frac{lL}{R^2} - \frac{KL}{R}\right) + \cos\left(\frac{Z}{R}\right)\left(K + \frac{1 + L}{R}\right) = K \qquad (3)$$

where R is the radius of the main path particle in the magnetic field (or electric field), assumed to act alone.

Let us consider the numerical example of a Wien filter having $L = l = Z$. The radial focusing for $K = 0$ takes place when $R0 = 0.765Z$. If $K = -0.5$, the kinematic effect is corrected for $R = 0.651Z$, while for $K = 1.0$, the value $R = 1.054Z$ is needed. To cover this K range, a relative variation $\Delta R/R0 = 0.527$ must be performed (involving the same relative variations of the magnetic and electric fields). For $Z = 5$ m and a maximum electric field of 67 kV/cm, the upper energy of the analyzed particles will be limited to $n(10.9)$MeV, n being the charge-state number.

The method has the advantages of wide K range, and no need for mechanical adjustments. Its drawback is a limited energy range, especially for low charge states.

References

1. H.A. Enge, Nucl. Instrum. Methods 162, 161 (1979).

2. H.A. Enge, Rev. Sci. Instrum. 29, 885 (1958).

3. D.L. Smith and H.A. Enge, Nucl. Instrum. Methods 79, 144 (1970).

4. D. Ioanoviciu, Adv. Electronics El. Phys., 73, 1, (Academic Press, 1989).

5. P. Roussel, Nucl. Instrum. Methods. Phys. Res. A236, 20 (1985).

Installation and Operation Experience of Superconducting Beamline Magnets

J. DeKamp, H. Laumer, C. Magsig, J.A. Nolen, D. Pendell, D. Sanderson, B. Sherrill, and A.F. Zeller

Introduction

With the Interim Vault experimental layout complete[1] and experimental operations underway, valuable installation and operation experience has been gained which will help in Phase II construction and operation. Beamline cryogenic operation has also become much better defined, allowing for a better planned Phase II control system. In addition many of the additional devices built for Phase II have been built and tested.

Beamline Magnet Installation

One quadrupole singlet, two quadrupole doublets and one ±16° dipole were installed in the Interim Vault beamline. The beamline quadrupole magnets were placed by optical alignment through the use of targets placed on the magnet's conflat flanges, which define the physical beam axis. The dipole was aligned with dowels placed directly in the poletips, defining the axis of symmetry. The cryogenic lines were then welded and the magnets realigned to account for positional changes due to cryogenic manifold welding operations.

We then aligned the magnetic axis of the quadrupoles with the physical beam axis by rotating a Hall probe about the physical axis inside the quadrupole field, and adjusting the quadrupole support frames. The frames were adjusted by repositioning hanger bolts at the top of the devices until the peak fields at the radius of rotation of each pole tip were equal within 0.2%.

Special consideration was given to the quad singlet which is very close to the K1200 cyclotron. Restraints were installed between the singlet and the cyclotron against magnetic forces from the cyclotron fringe field. The quadrupole fields in the singlet and first doublet were also evaluated with the cyclotron magnet on, then off, to determine effects on their fields from the cyclotron fringe field, and to see if extra magnetic shielding should be added to the 1/2"-thick steel cryostat vacuum box of the quads. No additional shielding was needed.

An added complication to installation was the discovery of both N_2 and He leaks in the first doublet. This required some cryogenic testing to determine effects on operation. For this purpose, a pumping station was added to the cryogenic manifold close to the doublet to pump the He, since the N_2 could be cryo-pumped by the LHe container. The pumping station kept the residual He gas in the vacuum to a low enough level that very little extra LHe boil-off was noticed, and operation was not a problem.

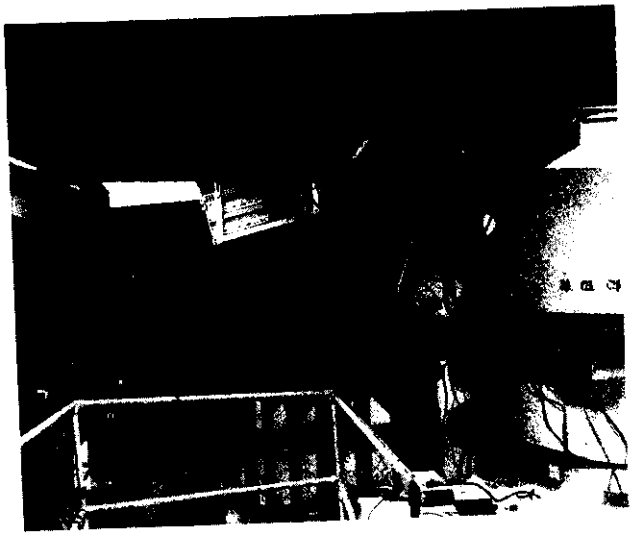

FIG. 1: The superconducting beamline magnets in the K1200 cyclotron vault. The singlet is just outside the cyclotron and is followed by the first doublet.

The beamline magnet installation in the K1200 vault is shown in Fig. 1.

The magnets in the Interim vault are shown in Figs. 2 and 3.

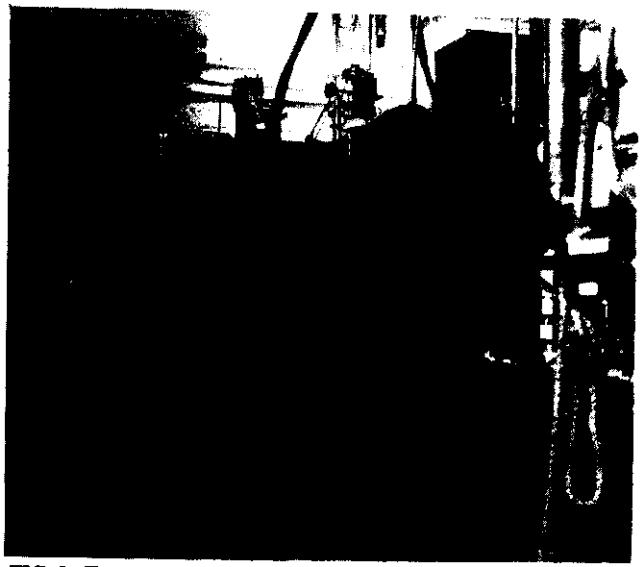

FIG. 2: The beamline magnets in the interim vault. The 16° dipole is just outside the wall separating this vault from the K1200 vault, and is followed by the second doublet. A small normal resistive dipole for vertical steering is between the superconducting dipole and doublet.

FIG. 3: Close-up of small normal resistive dipole between superconducting dipole and doublet shown in Fig. 2.

Beamline Magnet Operation

The superconducting beamline magnets have operated smoothly since operation has started. Beam tuning has been trouble-free, with initial settings from optics calculations being close enough so that only fine tuning is required.

Beam tuning is also very reproducible. Once the settings are established for a given beam, the same settings will get the beam on target again in later experiments. A tuning problem exists in that it is a little difficult to tune the dipole until the power supply achieves regulation. This makes the tuning process take somewhat longer than one would like, as the regulation is slow.

When Phase II is complete, all power supplies for the beamline magnets will be made in-house. For the interim beamline, we are using commercially-manufactured power supplies that we have modified here. The quadrupole supplies are 20V/20A, bipolar, 4-quadrant. The dipole power supply is a 10V/100A single polarity and uses a combination energy-absorber and current-reversal switch which limits the ramping to 3.5 V.

As of the end of 1988, the magnets have never been warmer than 80°K and have experienced only one incident influencing magnet operation. This occurred when the LHe storage dewar ran empty and an automatic fill cycle was triggered by the control system. Warm He gas was then fed to all the magnets, which eventually depleted the LHe which was left in their containers, causing all magnets to quench. Beam was not being put through the magnets at this time. As expected, no damage to the magnets occurred and the magnets were re-cooled from 80°K and ready to operate again within 24 hours.

The mode of magnet operation consists of leaving the He return valve open all the time, and opening the LHe feed valve only during the fill cycle. Because the control system is minimal at this time, very few magnet safety interlocks are installed. Leaving the He return valve always open provides adequate venting of He in case of a magnet quench and insures some cold gas flow through the leads in case the container runs dry of LHe while the magnet is operating.

Even though the magnet is self-protecting, the leads must have flow to keep them from burning up when there is current flow. Because of the heat capacity in the magnet steel, with the return valve closed and no LHe present, it would be possible for the leads to burn up before the magnet quenched. Leaving the He return valve open also helps decrease lead frosting/defrosting problems during fill cycles due to higher filling pressures.

The cryogens are automatically filled by the Modicon control system and independent timers, relays, and sensors. The fill cycle can also be put into a manual mode and each device independently filled if necessary. Because of the predictability and consistency of the LN_2 boil-off rates, the fill cycle is started by the Modicon's internal timer. The cryogen is presently filled once daily but is capable of going three days between refills, being limited by the dipole LN2 holding time.

Because the magnets fill with LN_2 in series, a thermocouple is placed at the exhaust, which triggers the valve closing through its controller. As this method has worked very well and is also very simple, it has been designed into the Phase II control system.

The LHe fill cycle is more complicated, consisting of two separate steps: transfer line cooldown and the actual refilling. The fill cycle is triggered by the Modicon timer. The LHe feed valve at the distribution box is opened and the transfer line is cooled through a crossover valve which connects the feed and return lines. An independent timer opens the device feed valves and closes the crossover valve, filling the devices. When the devices are full, the device feed valves and the valve at the distribution box close and the loop valve reopens. The dipole is presently filled once a day and the quadrupoles filled every other day.

The present beamline requires a time-averaged 5.9 l/hr of helium liquification. Transfer losses account for 72% of the present beamline refrigeration load, with the total steady-state heat load of the four devices being only 1.7 l/hr at their operating pressure of 1.35 atm. The transfer loss rates will be greatly reduced in Phase II because the magnet refill cycles will be five to seven days rather than the current one day (which is dominated by the higher heat load of the prototype dipole). The Phase II superconducting beamline will involve about 10 times the number of magnets in the interim vault. Hence, the Phase II beamline magnets will use 10 to 20% of the 200-l/hr capacity of our refrigerator, depending in detail on transfer frequency and transfer line losses.

Operation and testing of the quadrupoles and dipoles built so far shows very good reproducibility. The heat loads of the quadrupole doublets are very close in value. The leads on the doublets operate very efficiently with almost no frost at the top. The ±16° dipole in the interim vault has a heat load higher than desired. Its magnet leads are also less efficient than those on the doublets. Design changes made for the remaining dipole have been shown to be successful as evidenced by testing of the first 22.5° 'X' dipole. The steady state heat loads of the devices now operating and those tested to date are shown in Table 1.

TABLE I: Interim vault cryostat LHe boil-off rates (1.2 atm).

Magnet	Boil-off rate (liters/hour)	Refill every:
Quadrupole singlet	0.18	5 days
Quadrupole doublet #1	0.32	6 days
Quadrupole doublet #2	0.27	7 days
±16° dipole	0.68	2.5 days
Phase II magnet tests:		
8 quadrupole doublets	0.27	7 days
22.5° dipole	0.35	5.5 days

The leaks in the first doublet show the potential for undiagnosed future leaks; however, through experience and accurate leak-checking records, we rediscovered the causes for previous leaks, thereby lessening the chance of future leaks.

From testing, it was determined that the helium boil-off rate does not increase on the quadrupoles when the magnets are turned on, which gives further evidence of the efficiency of their leads.

An exception is the first doublet, which has an apparent bad wire splice in one of its magnets; this increases its heat load. The splice is in a coil, but is in contact with LHe, which prevents magnet operation problems. This is the only coil in all the quads with a splice at a point other than a lead.

References

1. B. Sherrill *et al., MSU Annual Report* (1987), p. 183.

Superconducting Beamline Magnet Construction Progress

J.C. DeKamp, C.T. Magsig, J.A. Nolen, and A.F. Zeller

The beamline magnet construction project presently consists of building 21 quadrupole doublets, two ±16° dipoles, and six 22.5° 'X' dipoles. These magnets are in addition to the two quadrupole doublets, one quadrupole singlet, and one ±16° dipole already built. Other details of the design and construction of these magnets are published elsewhere.[1-6]

The dipole steel was manufactured differently than our first dipole, which was forged from 1003 steel, with 3-to-1 forging factor and with all steel fully annealed. The eight new dipole steel assemblies were made from vacuum-degaussed 1001 continuous-cast steel plate, with only the poletips reduced by a factor of three by cross-rolling. Also, only the poletip steel was annealed. Because the steel is originally manufactured as plate, we reduced the original bid price by changing the ±16° dipole steel assembly from a trapezoid to a rectangle, which resulted in savings in flame cutting and machining, even though the magnets are more massive.

Procurement of parts took longer than expected due to rebidding of many parts and changing the bidders to keep costs as budgeted. Though device construction was delayed somewhat, procurement costs were kept as estimated. The procurement cost per doublet was $16K and per dipole was $32K. All magnet and cryostat parts were received by December, 1988. Four dipole steel assemblies were received from Inland Steel Corp., who was responsible for the steel production, machining, and assembly, including holding the poletip assembly gap tolerances. The other four steel assemblies are completed and being stored temporarily by the vendor. One 22.5° 'X' dipole has been uncrated and looks very good. This steel assembly is shown from two angles in Fig. 1.

Doublet and dipole construction has consisted of completing cryostat subassemblies, winding quadrupole coils, and assembling coils to the quad magnet steel. Subassemblies completed for all magnets include the He feed and return lines, overpressure vent pipes, current leads, cryostat vacuum boxes, and LN_2 containers. About 130 superconducting quadrupole coils were wound, giving a total inventory of 160 coils by the year's end. Three doublet steel/coil assemblies have been completed, with the steel assemblies connected to each other by tie bars and aligned. Each doublet is to have its steel assemblies aligned axially within .002" and rotationally within 10 minutes.

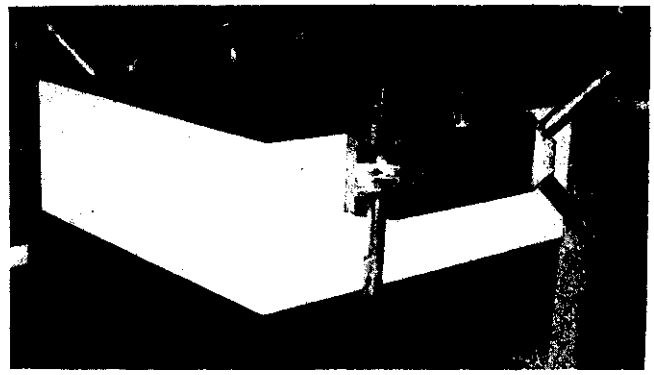

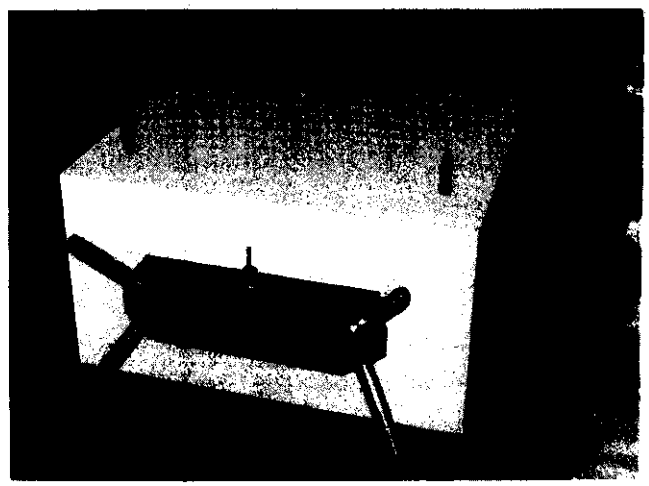

FIG. 1: 22.5° 'X' dipole magnet steel assembly.

References

1. A.F. Zeller *et al., Procedures of Ninth International Conference on Magnet Technology* (1985), p. 160.

2. A.F. Zeller *et al., MSU Annual Report* (1985), p. 176.

3. J.C. DeKamp *et al., MSU Annual Report* (1986), p. 186.

4. J.C. DeKamp *et al.,* IEEE Trans. Magn. 23, No. 2, 524 (1987).

5. J.C. DeKamp *et al., MSU Annual Report* (1987), p. 187.

6. J.C. DeKamp *et al., MSU Annual Report* (1987), p. 189.

NSCL Phase II Beamline Electronics

A. McGilvra, P. Koblas, G. Zheng, J. Vincent, and W. Numberger

The electronics for the Phase II beamline (beamline that connects the K1200 cyclotron to all the experimental vaults) consist of controls, power supplies, and instrumentation.

Controls: Analog, Digital, and Serial

The controls are analog input and output signals, digital input and output signals, and serial communication channels (RS-485).

Analog channels are set and read by digital-to-analog and analog-to-digital cards in VME crates, which are usually placed near the equipment. The analog input, once digitized, is sent via an ARCNET link to the main console in the Control Room, where it is viewed on a DEC μVAX workstation. All analog data can also be viewed locally on VME consoles. (See *Phase II Control System, Foth*, for description of VME consoles.) The analog output travels the same route in reverse: from the main control console, through the ARCNET link, to the VME digital-to-analog converter card.

Digital channels are set and read by a Gould-Modicon programmable logic controller (PLC). The digital readings are monitored by the PLC and the settings are determined by pre-programmed logic in the PLC. Digital readings and settings can be viewed at the main control console, or locally on a Metra or Panelmate user-interface screen.

Serial communications are sometimes used where analog channels would be too noisy. Serial channels are controlled by serial communication cards in VME crates. The serial communications data is transferred to and from the main control console on the same ARCNET link as the analog channels. Like the analog channels, it can be viewed at the main console on a DEC μVAX workstation, or locally on a VME console.

A device may have a variety of signals controlling it. A common example would be a power supply for a beam-focusing magnet. In this instance, an analog channel determines the magnet current set point and a digital channel turns the power supply on and off. Beamline power supplies are discussed in the next section.

Beamline Power Supplies

The beamline power supplies are controlled from the main control console by the system described above. The supplies are located along the beamline and are relatively far from the Control Room.

The power supplies power the superconducting magnets. There are two types of magnets: quadrupole (4 poles, for beam-focusing) and dipole (2 poles, for beam-bending).

The quadrupole magnets' power supplies are rated at 20 volts and 20 amps (20V/20A). Controls for a 20V/20A power supply consist of:

- one analog output (set point for magnet current)
- two analog inputs (actual magnet current and voltage)
- two digital outputs (power supply on/off and power supply ramp to 0 magnet current), and
- two digital inputs (water flow/temperature fault and power supply on/off status).

The dipole magnets are powered by power supplies rated at 10 volts and 100 amps (10V/100A). Functionally, the same controls are needed for 10V/100A power supply as for the 20V/20A power supply (see above), but in the 10V/100A, a single serial communications channel is used in placed of the three analog channels. This is because the 10V/100A power supplies, which are placed near the magnet, are too far away from the VME crate to reliably transport noise-free analog information. (The 20V/20A power supplies are grouped near their VME crate, so their cables are short enough for noise-free operation.)

Beamline Instruments

There are several instruments on the Phase II beamline. Some include:

1) beam current meters (BCM's) for reading the beam current at certain points on the beamline;

2) bang-bang servos (BBS's) for controlling motor drives which move beam diagnostic and experimental apparatus;
3) instruments for controlling the vacuum and cryogenic systems; and
4) additional devices, such as LED panels and dual meter panels.

1. Beam Current Meters (BCM's)

The BCM's are multi-range current meters with 16 ranges from 10pA to 300μA full scale. The range is set by the operator at the main control console and is received by the BCM through the serial line. The beam current reading is converted to IEEE floating point format by the microprocessor in the BCM and is transmitted on the serial communications line to a VME crate, then to the main control console via the ARCNET link.

2. Bang-Bang Servos (BBS's)

The BBS motor controllers are also controlled via a serial communications line. The motor settings and readings are transmitted between the BBS and the VME crate through a serial line and from between the VME crate and the main control console via the ARCNET link.

3. Vacuum and Cryogenic Controllers

We buy most of these but do build two: the dual-channel thermocouple vacuum-gauge controller and the cryogenic monitor unit.

The dual-channel thermocouple vacuum-gauge controller interfaces to two thermocouple vacuum-gauge transducers. It provides two 0-10 V signals that are related to the vacuum level at the transducers. There are also two digital signals that are inputs to the PLC which indicate if the vacuum has fallen below the preset limits.

The cryogenic monitor unit monitors all the functions of a typical cryostat. A typical cryostat is a doublet (contains two coils) and has a helium-pressure transducer and a helium-level transducer. The cryogenic monitor unit has interfaces to these transducers and can thereby provide 0-10V signals related to helium pressure and helium level. These analog signals are input to a VME crate and ultimately appear at the main control console. The unit also has six threshold detector circuits for detecting:

- helium rupture (pressure falls below one PSI);
- helium rupture warning (pressure exceeds 15 PSI);
- high helium level;
- low helium level;
- high magnet lead drop 1 (voltage drop on lead of first magnet exceeds 100 mV); and
- high magnet lead drop 2 (voltage drop on lead of second magnet exceeds 100 mV).

These digital status signals are inputs to the PLC and also drive the LED on the LED Panel (see below).

4. Additional Devices

In addition, there are three devices for monitoring information locally so that one can see information needed while performing operations in the vaults. These three monitoring devices are very simple.

* The LED Panel consists of 144 LED's, which monitor six status functions on 24 cryostats:
  helium rupture,
  helium rupture warning,
  high helium level,
  low helium level,
  high magnet lead drop 1, and
  high magnet lead drop 2.
* The cryogenic dual meter selector panel is simply two digital panel meters and two 24-position selector switches for reading helium level and helium pressure from 24 cryostats; there is also a push-button for activating the helium level sensor.
* The vacuum dual meter selector panel is the same as the cryogenic one, except the meters read vacuum information and there is no level-sensor activation push-button.

Radiation Monitoring and Personnel Security System in Phase II

R.M. Ronningen, R.A. Blue, B.L. Jiang, G. Humenik, T.R. Jones, E. Kashy, M.R. Maier, D. Scott, and J. Yurkon

In last year's Annual Report we described a radiation monitoring and personnel security system based on the use of a Square-D Corporation SY/MAX model 300 programmable logic controller (PLC) and a personal computer. In 1988, this system was used for K500 and K1200 operations. However, there were several modifications of the scheme presented last year.

The original 8-bit input/output modules were supplemented by 32-bit modules, which expand system capacity considerably. Two racks were placed near the K1200 rf control console. In addition to the PLC CPU, the racks contain 8-bit I/O modules, three 32-bit I/O modules, and one 4-register analog input module. The former handle K1200 and interim vault personnel security functions (barrier chain microswitches, arming box switches) and the latter are mostly for neutron counters (via logic status of count-rate circuit cards described last year).

A new remote rack containing four of the high-density modules (2 input and 2 output) was placed near the K500 rf control console. These I/O points provide personnel security for the K500 vault and newly constructed experimental vaults. For future expansion we have available eight 8-bit I/O modules and a rack for remote location.

The security status of all vaults is displayed on a series of color graphics screens by a personal computer in the Control Room. This PC can also display ladder logic with real-time status of inputs and outputs. Logic conditions that prevent or shut off cyclotron rf produce alarm messages on the computer screen accompanied by audible tones. The messages are logged on a printer.

In the radiation monitoring area, counter/ratemeters with audio amplifiers were constructed for both cyclotron consoles. These convert neutron counter pulses into audible "clicks", which aids the operator in tuning.

Construction and installation of radiation safety devices is still progressing. Visual and audible security alarms, triggered by PLC outputs, are being installed in all the vaults. The use of a voice synthesizer/tone generator for audible alarms is being explored. In this application the PLC logic would trigger a software interrupt, bringing up a selected voice and/or tone lexicon for the synthesizer. The PLC logic would also trigger hardware relays to start the visual alarm and link the synthesizer output (amplified) to the appropriate public address speaker.

Along with additions to the radiation safety system, improvements are still being made to the present equipment. During initial operations of the system there were episodes of frequent alarm triggering due to noise pick-up on the coaxial cables which link neutron detectors to the count rate logic cards. We eliminated this problem by replacing the RG58/U coax by "superscreened" MM 11/50 cable (Permanoid Ltd., Manchester, UK).

In closing, the PLC-based radiation safety system has served us well, even from its initial use. Its modular structure, composed of a programmable logic controller, logic card, BF3 counter, and counter/ratemeter, makes it easy to disassemble and rebuild according to specific need. This is particularly useful during construction phases of the facility, when the configurations of the cyclotron vaults, experimental area shielding walls and beam transport configurations may change often. The system is also versatile enough to serve other causes, since the logic card, BF3 counter, and counter/ratemeter can work without the PLC. This versatile functionality was put to good use recently when the system, sans PLC, provided radiation monitoring during testing of the Harper Hospital K100 cyclotron.

Nuclear Electronics

M.R. Maier, D.J. Morrissey, K. Niemeyer, M. Robertson, and James Vincent

This year the Research Electronic Group (REG, renamed) mass-produced a number of electronic modules primarily for the hodoscope experiment of the Gelbke group. We had to redesign the quad shaping amplifier and are building 25 modules. When it was realized that the experiment needed quad gate generators more urgently, we produced 20 modules on short notice. The hodoscope experiment is also using silicon detector preamplifiers with a built-in calibration facility, and we built approximately 100 channels, including the necessary driver modules for the calibration chopper in the preamplifiers. Along with the photodiode preamplifiers described in the last annual report, all these electronic modules have contributed to the success of the hodoscope experiment.

Along other lines, a prototype of the "fast decision module" for use with the 4π detector was successfully tested. This module has a look-up-table memory with 16 address lines and 17 data lines (i.e. 64K 17 bit words) with a propagation delay of approximately 35 nsec. To increase its utility, the experimenters requested the addition of a delay and gate generator fired by bit 17, that has been included in the final design. The preamplifiers for the Bragg curve section of the 4π detector were also redesigned, separating the input field effect transistor (FET) from the rest of the circuitry. This allows the connections between the detector and the FET to be very short. This arrangement is less susceptible to the external noise interference that had been a problem in test runs. Fifteen units of the new version have been built and used in a S320 spectrograph experiment, confirming the high resolution and noise immunity (see corresponding contribution to this report). Another advantage of this arrangement is the low power dissipation of the first amplification stage (<50mW), a feature which allows us to place many of these FET's close to the detectors inside a vacuum chamber.

An ongoing task of the REG is the construction of photomultiplier tube (PMT) bases for different experiments. Fifty PMT bases for use in vacuum, using a common cable for high voltage and signal, were built for the forward array detector of the 4π detector array. This cable-economy freed vacuum feedthroughs for the installation of additional detectors. Another 50 PMT bases (for use in air) were built for the high-energy gamma ray experiment. We also constructed several prototypes of PMT bases for detector testing.

In addition to all these electronic units, we built several special devices for various experiments, ranging from passive signal splitters to cables. We also built and produced four units of a ratemeter for the radiation safety electronics -- and included all the changes that were requested after production had started.

Collaboration with David Fossan's group at SUNY at Stony Brook has led to the preparation of a paper about a new pulse shape discriminator for NE213 neutron detectors, which has been accepted for publication in Nuclear Instruments and Methods.

Because of the high workload, development of the octal CAMAC constant fraction discriminator had to be terminated. The company which was interested in buying the design has decided to do their own.

For the future we are designing a "ECLine to VME" interface module. This unit will interface the FERA ADC's via the ECLine port to a VME buffer memory. We hope to achieve readout rates of 50 thousand events per second with 50 parameters per event. This should allow complex front-end preprocessing of experiment data, and reduce the data volume recorded on tapes. We are still considering the design of multichannel ADC's, especially peak-sensing ones, and hope that our workload will allow this.

Magnetic Channel Design for a 250 MeV Superconducting Synchrocyclotron

X.Y. Wu and M.M. Gordon

Introduction

As reported last year, work is being carried out on the design of a 250 MeV superconducting synchrocyclotron for use in cancer therapy. The overall design of our regenerator and magnetic channel was influenced by the extraction system devised for the Harvard synchrocyclotron[1] while the required orbit calculations were modeled on those employed so successfully in upgrading the CERN machine.[2]

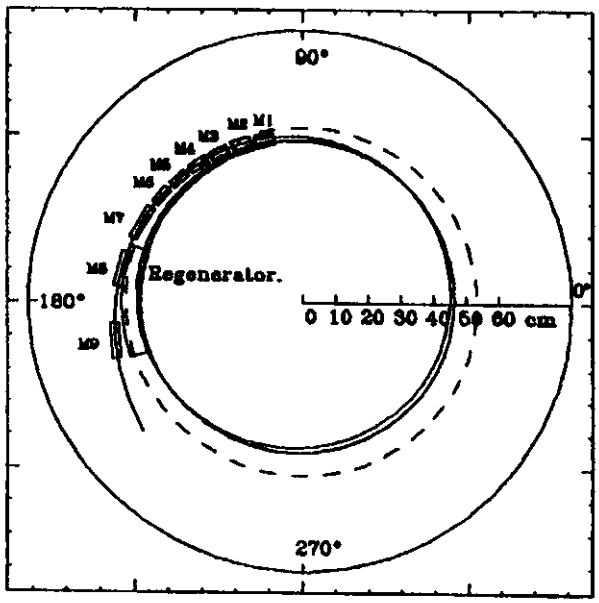

FIG. 1: Layout of the Extraction System showing the arrangement of the regenerator and the nine magnetic channel elements. M1, M2, M5, and M6 are deflecting magnets, and M3, M4, M7, M8, and M9 are all focusing magnets. The solid curve shows the last two turns of an extracted orbit, and the broken curve shows the pole boundary.

Our design process consists of iterating back and forth between magnetic field calculations and orbit computations in order to systematically improve the design parameters and optimize the extraction efficiency. In the magnetic field calculations, we simply assume that the main field is so strong (central field B=57 kG) that the regenerator and channel elements are all uniformly magnetized in the vertical direction, while in the orbit computations, we use our Z[4] Orbit Code[3] which provides an accurate evaluation of the important coupling effects between the radial and vertical motion.

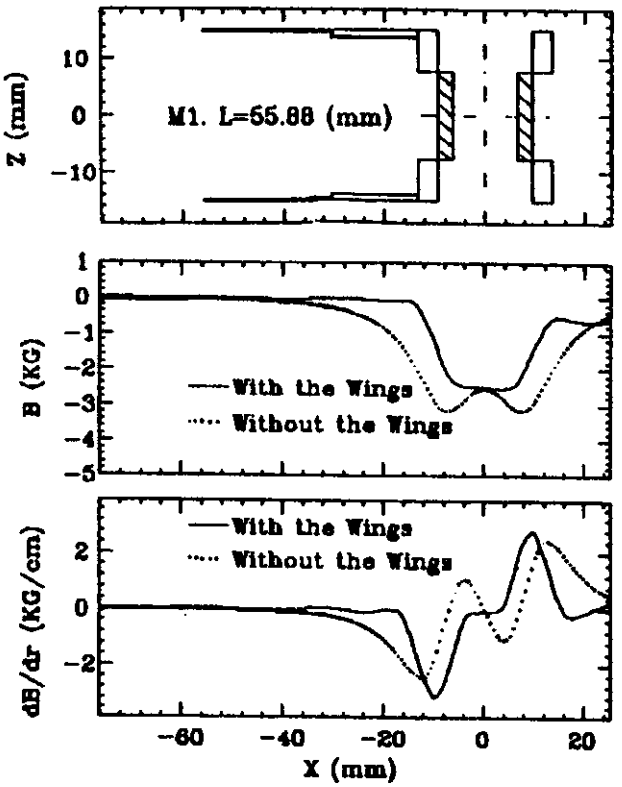

FIG. 2: Cross section of the deflecting magnet M1 with its projecting wings. Plots show the resultant field (kG) and field gradient (kG/cm) produced with (solid curve) and without (broken curve) the wings. The effectiveness of the wings is apparent. M2, M5, and M6 are similar.

Results on the design of the regenerator itself have already been published.[4] The passive magnetic channel consists of a sequence of deflecting and radial focusing elements that bend and focus the beam along its path around the regenerator. These elements are equipped with an elaborate set of "wings" which serve to shelter the internal beam from the extreme vertical overfocusing that would otherwise occur on the last few turns prior to channel entry. Figure 1 shows the nine magnetic channel elements with M1, M2, M5 and M6 being deflecting magnets, while the remainder serve mainly as radial focusing magnets.

Figures 2 and 3 show the geometries and magnetic properties of two typical elements. The magnetic channel starts at $\Theta = 100°$ with its aperture centered at r = 50.1 cm. The channel entrance aperture is 12.7 mm and the septum thickness is 3.2 mm.

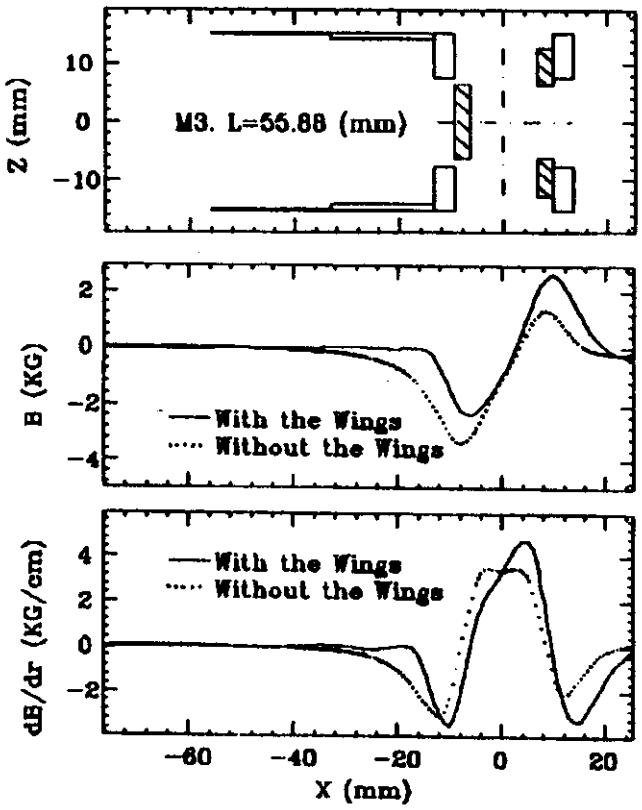

FIG. 3: Cross section of the radial focusing magnet M3 with its projecting wings. Plots of resultant field and field gradient are analogous to those in Fig. 2. M4 and M7 are similar in structure, but M8 and M9 do not require wings.

Radial Motion

Figure 4 shows the four static phase plots at $\Theta = 180°$ and E = 254.5 MeV that were used as initial conditions for the accelerated orbits. These plots correspond to radial amplitudes of 1.27, 2.54, 3.81 and 5.08 mm. The approximate stability boundary is also shown. (This boundary shrinks to zero at E = 255.7 MeV where $\nu_r = 1$.) Using a constant energy-gain per turn of 10 keV, the orbits are traced until they are either successfully extracted or lost through hitting an obstacle.

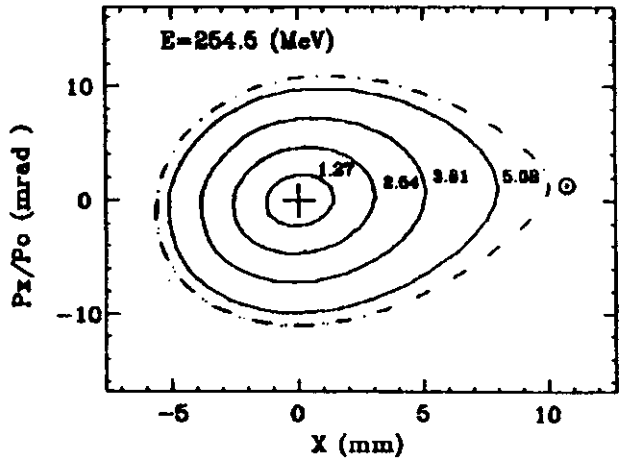

FIG. 4: Radial phase plots at E = 254.5 MeV and $\Theta = 180°$ showing four invariant curves for radial amplitudes of 1.27, 2.54, 3.81 and 5.08 mm. Between 60 and 74 points on these curves were used as initial conditions for the accelerated orbits. The dot-dash curve shows an approximate stability boundary at this energy.

The resulting phase space distribution at the entrance of the magnetic channel is shown in Fig. 5 for the four different radial amplitudes. Plotted here are the differences between the (r,p_r) of the orbits and the (r_o,p_{ro}) of the central ray; also shown are the position and size of the septum. Orbits entering the channel with too small or too large values of p_r hit the inner or outer wall, respectively. About 42% of the orbits are successfully extracted.

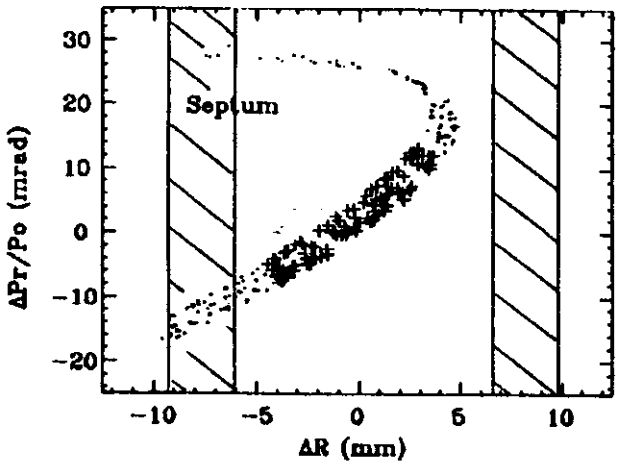

FIG. 5: Radial phase plot at the entrance of the magnetic channel ($\Theta = 100°$) showing resultant distribution for median plane orbits with initial conditions given in Fig. 4. Points labeled with "+" signs indicate those orbits that successfully traverse the magnetic channel. (p_o is the momentum corresponding to $E_o = 255.0$ MeV.)

Combined Radial and Vertical Motion

The computations were carried out using the Z^4 Orbit Code which is based on exact equations of motion and magnetic field components that are correct to fourth order in z.[3] The results therefore provide a more realistic evaluation of the effects of the vertical motion. For each of the (r,p_r) values used above at 254.5 MeV, we used eight initial (z,p_z) points uniformly spread around an eigenellipse having a given maximum height Δz_o=2.54 or 5.08 mm. Figure 6 shows the initial (z,p_z) conditions used in these computations.

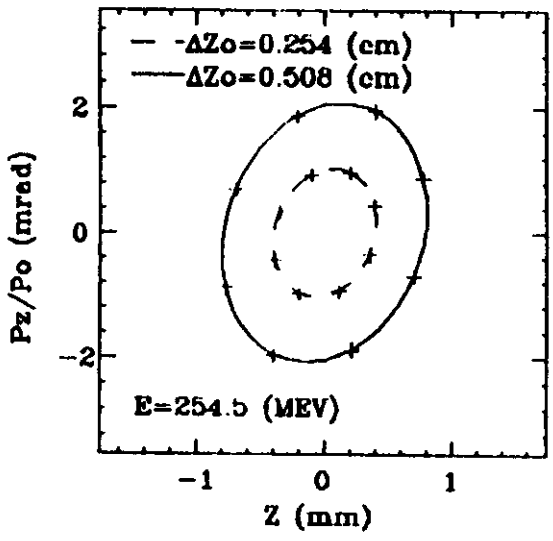

FIG. 6: Initial (z,p_z) values at E=254.5 MeV and θ=180° used for accelerated orbits in conjunction with the (r,p_r) values given in Fig. 4. The two eigenellipses shown have maximum height Δz_o=2.54 and 5.08 mm near θ=0.

As shown in the work at CERN,[5] orbits with large radial amplitudes produce unacceptable growth in the vertical oscillations due to the $\nu_r=2\nu_z$ coupling resonance. Our present studies show that the reverse can also be true and that in some cases, the radial and vertical oscillations grow simultaneously to very large amplitudes. Since ν_r=1 and ν_z=0.5 in these cases, we attribute this phenomenon to the $\nu_r+2\nu_z=2$ coupling resonance.

For the smallest radial amplitude used in these studies, 1.27 mm, the coupling action remains within acceptable bounds and 51% of the orbits are successfully extracted. For the 2.54 mm radial amplitude case, the extraction efficiency drops to 32% with about 12% of the orbits exceeding a vertical amplitude limit of 15 mm prior to reaching the

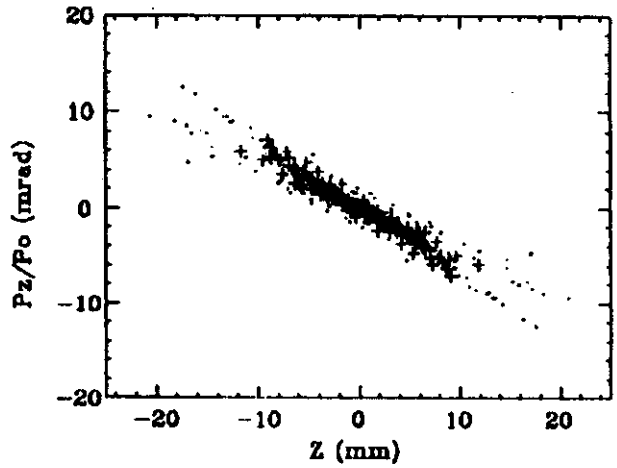

FIG. 7: Phase plot at the entrance of the magnetic channel (θ=100°) showing the $(z,p_z/p_o)$ values for all the orbits with initial conditions given in Fig. 6 and Fig. 4 for the two smaller radial amplitudes. Points labeled by "+" signs indicate those orbits that successfully traverse the magnetic channel.

channel. Figure 7 shows the resultant vertical phase space distribution for all of these two sets of orbits at the entrance to the channel.

The results are very different for the two largest radial amplitudes, 3.81 and 5.08 mm, where 92% of the orbits fail to reach the channel entrance. That is, the coupling effects described above produce vertical amplitudes that are too large for the given aperture, 30 mm. Thus we find that reasonably good extraction efficiency can be achieved only if the internal beam prior to extraction has a maximum radial amplitude of about 3 mm. This is consistent with the results obtained at CERN[2] where the radial amplitude limit is about 10 mm, since our field is about three times higher than the CERN field and one might expect lengths to scale inversely with the field values.

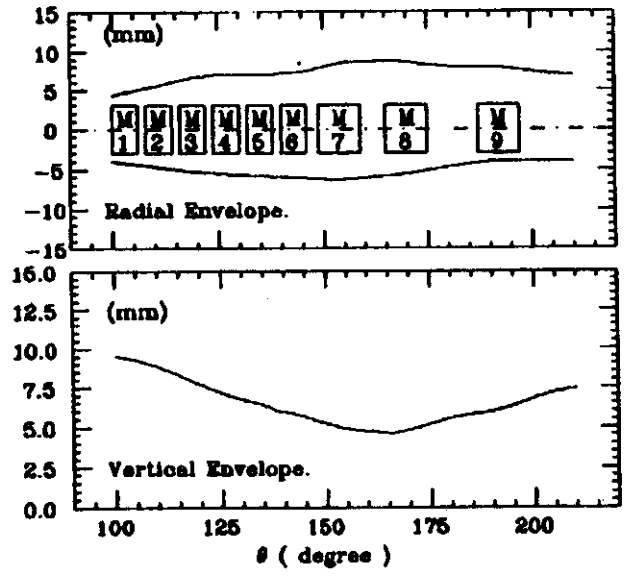

FIG. 8: Radial and vertical envelopes for all of the successfully extracted orbits as they traverse the magnetic channel. Plots show $(r-r_0)$ and $|z|$ vs. θ from 100° to 210°. All 145 orbits used here started at 254.5 MeV with initial radial and vertical amplitudes less than 3 mm as shown in Fig. 4 and Fig. 6.

Conclusions

Assuming now that the internal beam can be controlled so that both the radial and vertical amplitudes do not exceed 3 mm, our results indicate that an extraction efficiency of about 40% can be achieved. A plot of the radial and vertical envelopes for the resultant beam as it traverses the magnetic channel is shown in Fig. 8, and these results confirm that the beam remains well focused. The corresponding radial and vertical phase space distributions at the exit of the channel are shown in Fig. 9 with resultant emittances of about 20 π mm-mrad radially and 30 π mm-mrad vertically.

Finally, the projected energy distribution of the extracted beam is shown in Fig. 10, and indicates an energy spread of about 500 keV. We should note that this spread depends quite strongly on the vertical amplitude as well as the radial amplitude.

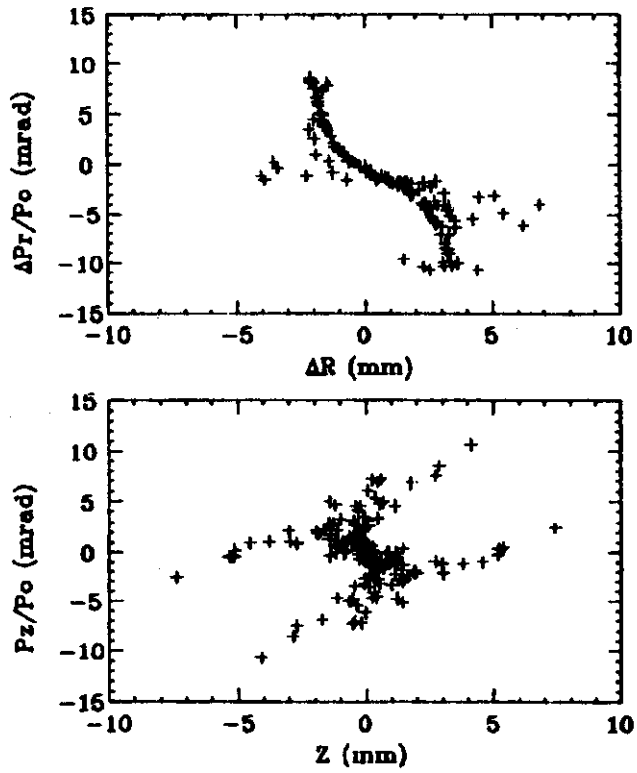

FIG. 9A: Radial and vertical phase plots at the exit of the magnetic channel (θ=210°) showing the distribution of points for the 145 orbits described in Fig. 8. The estimated final emittances are about 20π mm-mrad radially and 30π mm-mrad vertically.

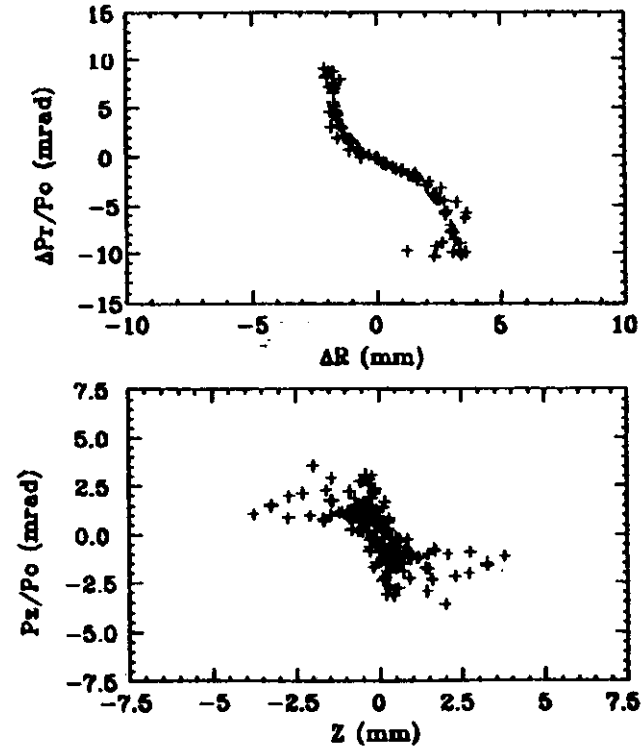

FIG. 9B: Same as Fig. 9A but using data only from orbits started with radial and vertical amplitudes of 1.27 mm. In this case, the radial emittance is 12π rather then 20π mm-mrad, and the vertical emittance is 6π rather than 30π mm-mrad. These results demonstrate the significance of the nonlinear coupling effects.

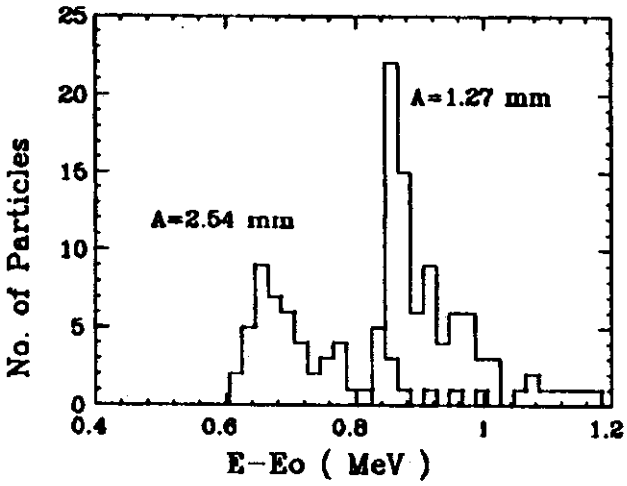

FIG. 10: Distribution of final energies for the 145 orbits described in Fig. 8 and Fig. 9. The histograms show the number of extracted orbits vs. $(E-E_0)$ where $E_0 = 255$ MeV, with two separate curves for initial radial amplitudes of 1.27 and 2.54 mm.

The required control of the internal beam quality depends quite directly on the design of the central region and, in particular, whether an enclosed ion source plus puller can be accommodated within the small space available. The investigation of this problem will be our next task now that the design of the extraction system has been completed. The computer programs that have proved so successful in designing the central regions of our other cyclotrons will require only a slight modification to make them suitable for application to the central region of a synchrocyclotron with its frequency-modulated rf system.

References

1. G. Calame *et al.*, Nucl. Instrum. Methods I, 169 (1957).

2. B. Allardyce *et al., Proceedings of the 7th International Conference on Cyclotrons and their Applications* (Birkhauser, Basel, 1975), p. 287.

3. M.M. Gordon and V. Taivassalo, Nucl. Instrum. Methods A247, 423 (1986).

4. M.M. Gordon and X.Y. Wu, *Proceedings of the 1987 Particle Accelerator Conference* (IEEE, New York, 1987), p. 1255.

5. S. Lindback, *Proceedings of the 5th International Cyclotron Conference* (Butterworths, London, 1971), p. 235.

Cancer Therapy Cyclotron for Harper Hospital

H. Blosser, J. Bailey, E. Kashy, T. Kuo, F. Marti, R. Morin, R. Ronningen,
D. Sanderson, G. Stork, J. Wagner, and G. Zheng, of NSCL
and
E. Blosser, G. Blosser, R. Maughan, and Wm. Powers, of Harper-Grace Hospitals

A K100 superconducting cyclotron has been constructed and brought into operation in a project sponsored by Harper-Grace Hospitals Inc. of Detroit. After completion of testing at NSCL, the cyclotron will be moved to Detroit and installed in the Gershenson Radiation Oncology Center of Harper Hospital, where it will be a key element of a comprehensive radiation therapy system for cancer. (The Gershenson Radiation Oncology Center also has 20- and 15-megavolt linear accelerators and two cobalt therapy units.)

The goal of the cyclotron project is to provide neutron beams for treatment of cancer in a physical setting matching that of the linear accelerators so that the possible beneficial effects of the high linear energy transfer (LET) characteristic of neutron radiation can be evaluated in a setting which is otherwise comparable to the low LET treatments from the linacs and Cobalt units. Low LET treatments are given in the US to some half-million persons per year by linear accelerators and cobalt units in thousands of hospitals.

Critical prerequisites for this even-handed comparison of high- and low-LET treatments are:

1. A comparable depth of penetration.
2. An isocentric mounting.
3. Comparable collimation capability.
4. Facility located in the hospital so that life support systems are identical.

The cyclotron which has been constructed for Harper Hospital meets these goals, and by using a high-field superconducting cyclotron, considerable compactness and economy has been achieved relative to neutron therapy facilities based on room-temperature cyclotrons or linear accelerators. Figure 1 shows Dr. William Powers, the radiation oncologist who suggested the project, and Henry Blosser standing on the K100 cyclotron.

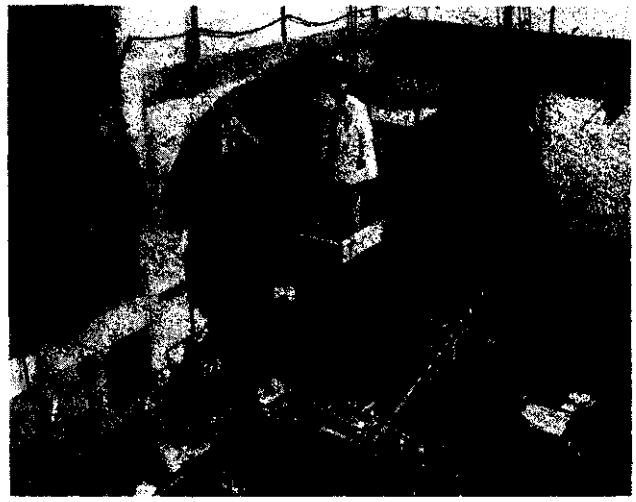

FIG. 1: Dr. William Powers, chairman of the Dept. of Radiation Oncology at Wayne State University and head of the Gershenson Radiation Oncology Center of Harper Hospital, standing and Henry Blosser kneeling on the top of the K100 cyclotron. The umbilical cord which feeds utilities to the rotatable cyclotron is at the center of the right-hand circular ring.

Many of the specific features of the cyclotron follow from the choice of rf frequency, namely 105 MHz, which allows the rf system to be driven by a standard commercial fm radio station transmitter. At this frequency, a deuteron beam is resonant in third harmonic mode at a central magnetic field of 4.6 tesla, which is a comfortable value relative to present magnet technology, but gives nevertheless a very compact cyclotron, the maximum energy orbit having a radius of only 30 cm.

Beam tests in the hospital cyclotron began in the spring of 1988 and beam was immediately accelerated to full energy. In first tests, beam current was much lower than the design specifications, which stipulated 20 microamps on a target at half energy and 10 microamps on a full energy

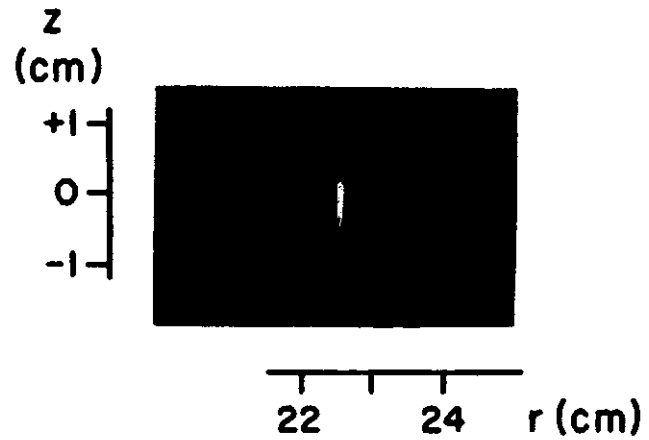

FIG. 2: A contact radiograph of the half-energy target, showing the spatial distribution of the beam at this point. The distribution almost exactly matches the size of the ion source slit, indicating a well focused beam.

target. (Calculations indicate that the medically desirable treatment time of 2 minutes will be obtained with a full energy current of approximately 6 microamps.) The low initial beam current was traced to details of the cyclotron central region and several corrective changes were introduced to achieve full design current. The most important of these changes involved redesign of the ion source extraction slit in order to reduce the time required for the ions to leave the source and cross the first gap, a half cycle at 105 MHz being only 5 nanoseconds. Cyclotrons have not previously operated at these high frequencies, and at lower frequencies the timing details at the source exit do not come into play as a limiting characteristic, so a new cyclotron phenomenon was involved. After appropriate central region corrections, beams of up to 55 microamps have been obtained, which gives a comfortable margin relative to the specification values. Figure 2 is a radiograph of the half-energy target, showing the spatial distribution of the beam at this point. (The distribution of the beam at the full energy target is similar but the mechanical details of the target are not compatible with a simple contact print radiograph.) The observed beam distribution nicely matches design goals.

Figure 3 shows schematically the mounting system for the cyclotron which involves a pair of 14-foot diameter rings mounted on rollers, with a counterweight opposite the cyclotron to balance the system, and a patient table cantilevered onto the axis of the ring system from the adjacent

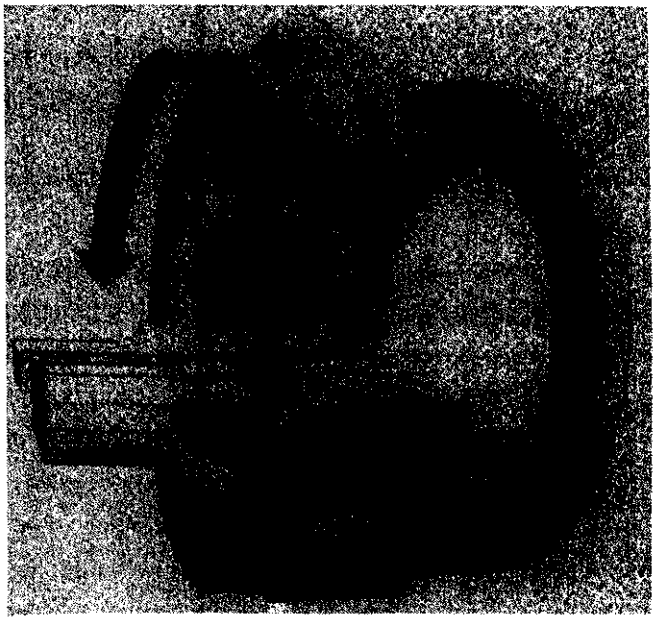

FIG. 3: Schematic drawing of the medical cyclotron shown in two positions relative to a patient. The cyclotron mounts on the rotating ring system with counterweight opposite. The patient table is cantilevered from the fixed floor at the left of the ring system, so that the cyclotron can move through a full 360° relative to the patient.

fixed floor. With this structure the cyclotron can rotate through a full 360° relative to the patient, and by using several beam entry positions (typically 4) a lethal radiation dose can be administered to a tumor site while dose to normal tissue is held at a level where undesired complications are acceptably rare.

Neutron therapy is of course not a new treatment modality, some 8,000 patients having been treated at various facilities in the world, with impressive success in a number of cancer situations. Figure 4 is from a paper[1] on follow-up results from an early study at the University of Washington of patients with advanced cancer of the prostate. In that early facility, treatments could be given only partially with neutrons, but nevertheless, the 6- to 10-year survival in the patients receiving neutrons more than doubled. Results over a similar time span are not yet available for more modern facilities, but for the time spans available, results for pure neutron beam treatments in these facilities are even more favorable than the Fig. 4 results. (There is also a moderate indication that results from neutron facilities with beam energy above 40 MeV are superior to results from lower energy facilities.)

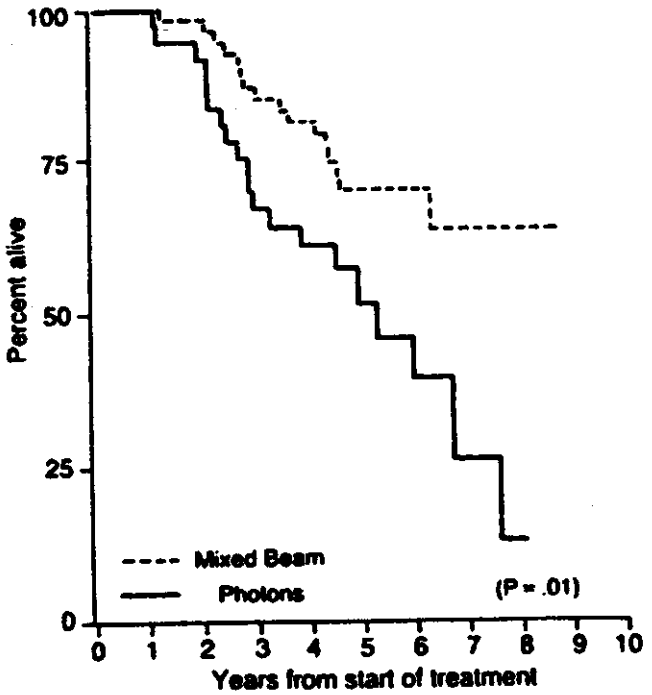

FIG. 4: Results from an early clinical trial in which patients with advanced prostate cancer were treated conventionally with photons or unconventionally with mixed beams of neutrons and photons. This study was conducted at the Univerisity of Washington.[1]

The Harper Hospital cyclotron involves two significant superconducting magnet advances, namely, to use a current density in the winding four times higher than that used in the larger NSCL cyclotrons, and to use a helium vessel which can rotate 360° and still be vented to the atmosphere. The helium cooling system is also based on conduction cooling of the coil, enabling the magnet to operate as long as any part of the coil is in contact with helium, rather than requiring full emersion. Details of the coil construction[2] and of the cooling system are shown in Fig. 5.

In the fall of 1989, the cyclotron will be transported to Harper Hospital and installed in a recently constructed shielded room. Operation should resume about two weeks after installation, following connection and checkout of utilities systems; calibration tests and treatment planning studies will require approximately six months, after which treatment of humans will begin.

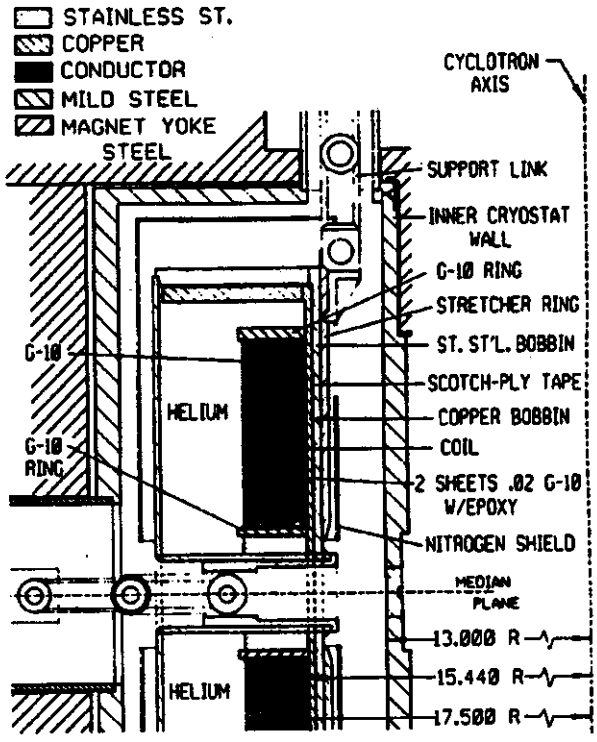

FIG. 5: Detailed section view of the cryostat, helium vessel, and main coil of the Harper cyclotron. The coil operates at a current density of 13,000 amps/cm^2 (averaged over the winding area).

References

1. Thomas W. Griffin, *Important Advances in Oncology*, edited by DeVita, Hellman, Rosenberg (J.B. Lippincott Co., Philadelphia, 1989) pp. 221-234.

2. H. Blosser *et al.*, IEEE Trans. Magn., 25, 1746 (1989).